ANUL XLII **1996**

S T U D I A
UNIVERSITATIS BABEŞ-BOLYAI
PHYSICA
2

Editorial Office: 3400 CLUJ-NAPOCA, Gh. Bilaşcu no.24, ♦ Tel. 194315; int. 167

S U M A R - C O N T E N S

STUDIA UNIVERSITATIS BABEŞ-BOLYAI, PHYSICA XLI, 2, 1996

MAGNETIC PROPERTIES OF Cr_2O_3-TeO_2-B_2O_3-PbO GLASSES

I. ARDELEAN[1], M. PETEANU[1], V. SIMON[1], S. FILIP[2], N. MUREŞAN[1]

ABSTRACT. The magnetic measurements have been performed on Cr_2O_3-TeO_2-B_2O_3-PbO glasses with $0 < x \leq 20$ mol %. The data indicate that the chromium ions are in Cr^{3+} valence state. For $x \leq 3$ mol % the greater part of these ions are isolated or experience dipole-dipole interactions. For higher Cr_2O_3 content a mictomagnetic type behaviour is evidenced.

INTRODUCTION

Chromium ions were largely used as paramagnetic probes for revealing the local order in diamagnetic vitreous matrices. A great variety of vitreous systems were investigated by means of Cr^{3+} EPR absorption spectra. They are oxide glasses as phosphate [1, 2], borate [3-5], fluoride [6-9], borosulphate [10], lead-bismuthate [11] and also chalcogenide glasses [12]. EPR and magnetic investigation of chromium ions in $3B_2O_3 \cdot PbO$ [4] and $2B_2O_3 \cdot Li_2O_3$ [5] vitreous matrices have evidenced the presence of both Cr^{3+} and Cr^{5+} ions.

Tellurite glasses have been extensively studied because their interesting properties and possible applications [13-15]. The magnetic behaviour of Cr^{3+} ions was less investigated in vitreous systems [16]. Previously we investigated the tellurite glass matrices $95TeO_2 \cdot 5PbO$ containing $3d^5$ ions [17-19] and $70TeO_2 \cdot 25B_2O_3 \cdot 5PbO$ containing Cu^{2+} [20], Mn^{2+} [21] and Fe^{3+} ions [22]. We succeeded to obtain information on the valence states of the paramagnetic impurities, their distribution in different structural units, the ligand field effects and the stability of the studied systems.

This paper reports results concerning magnetic properties of Cr_2O_3-TeO_2-B_2O_3-PbO glass system.

---

[1] Faculty of Physics, Babeş-Bolyai University, Cluj-Napoca.
[2] Department of Physics, University of Oradea, 3700 Oradea, Romania.

EXPERIMENTAL

The $xCr_2O_3 \cdot (100\text{-}x)[70TeO_2 \cdot 25B_2O_3 \cdot 5PbO]$ glasses with $0 < x \leq 20$ mol % Cr_2O_3 were prepared using as start materials Cr_2O_3, TeO_2, H_3BO_3 and PbO of reagent grade purity.

The samples were mixed in suitable proportion and melted in sintered corundum crucibles at 1000^oC for 6 minutes. The melts were poured onto stainless steel plates. The X-ray analysis showed that homogeneous glasses are formed up to 20 mol %. The magnetic data were obtained using a Faraday-type balance, in the temperature range 80-300 K.

RESULTS AND DISCUSSION

The temperature dependence of the reciprocal susceptibilities for some of the investigated glasses is presented in Fig. 1.

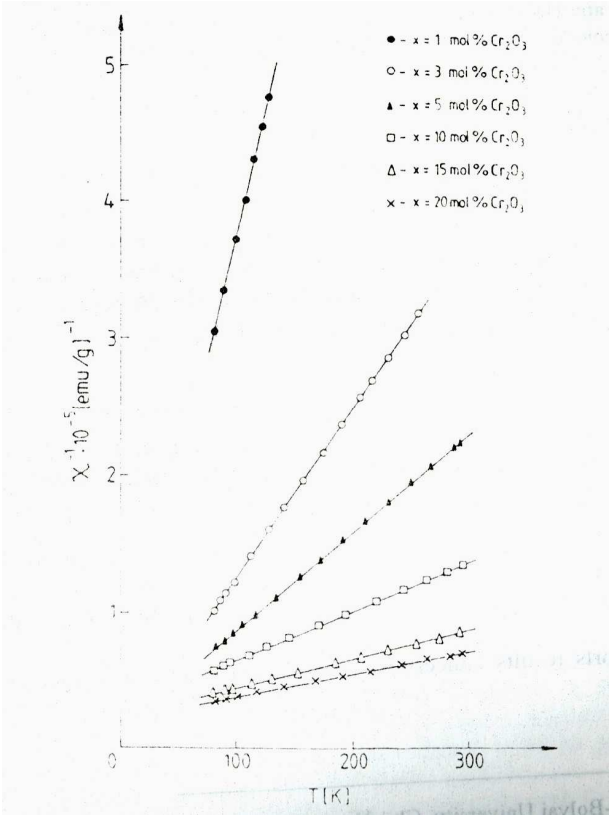

Fig. 1. Temperature dependences of the reciprocal magnetic susceptibility for xCr_2O_3 $(100\text{-}x)[70TeO_2$ $25B_2O_5$ $5PbO]$ glasses.

For x < 3 mol % Cr_2O_3 a Curie type behaviour is evidenced, suggesting that chromium ions are magnetically isolated. This result is also confirmed by EPR measurements [23], which indicate only isolated Cr^{3+} ions, subjected to dipole-dipole interactions. For higher concentrations (x > 3 mol % Cr_2O_3) a Curie-Weiss law is showed. The paramagnetic Curie temperatures, θ_p, are negative and increase in absolute magnitude when Cr_2O_3 content is higher. This suggests that the chromium ions are predominantly antiferromagnetically coupled. The magnetic interactions take place only at short range and can determine a mictomagnetic type behaviour [24, 25]. These results are also in agreement with the EPR data [23]. A similar conclusion was reported by Landry et al. [2] and confirmed by Fournier et al. [26] for phosphate glasses containing Cr^{3+} ions, and by Ardelean et al. for $3B_2O_3 \cdot PbO$ [4], $2B_2O_3 \cdot Li_2O_3$ [5] and $B_2O_3 \cdot PbO$ [11] glasses.

The composition dependence of the paramagnetic Curie temperature, θ_p, is presented in Fig. 2. The absolute magnitude of θ_p linearly increases within $3 \leq x \leq 10$ mol % Cr_2O_3.

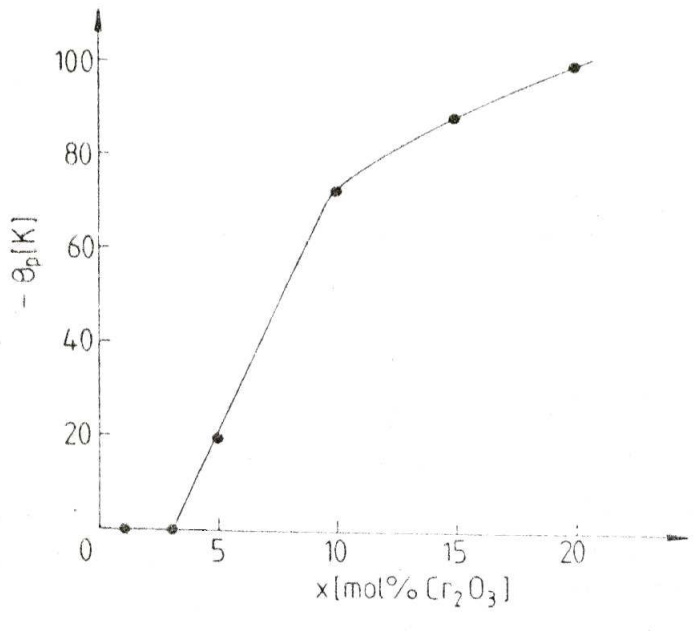

Fig. 2. Composition dependence of the paramagnetic Curie temperature, θ_p.

For x > 10 mol % Cr_2O_3 the slope of the curve changes, the increasing becomes much slower indicating weaker exchange interactions between chromium ions [4, 27]. By using the molecular field model [28, 29], the molecular field constant may be written as:

$$J = \theta_p / C_M = 2zJ_{ij} / Ng^2\mu_B^2$$

where N and z are the total and exchange coupled number of magnetic ions, g is their spectroscopic splitting factor, and μ_B is the Bohr magneton. The values of $J = \theta_p/C_M$ calculated for the experimentally obtained data are presented in Fig. 3.

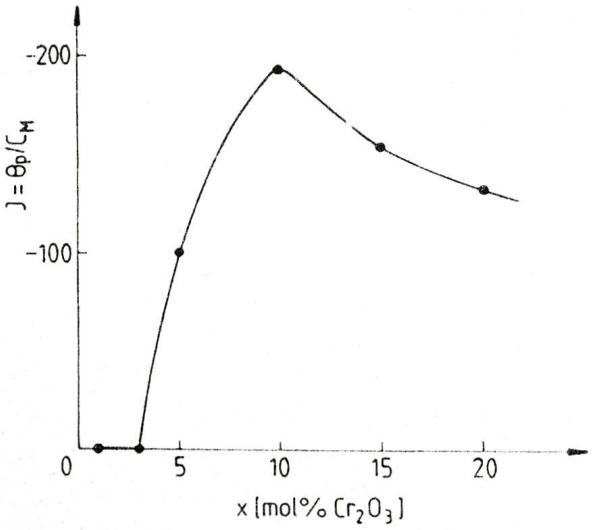

Fig. 3. Composition dependence of the molecular field constant, J.

The J values have a particular evolution. They increase up to x = 10 mol % Cr_2O_3 and decrease thereafter.Because the number of exchange coupled ions is proportional to the total number of magnetic ions from the glass sample we assume that the z/N ratio is constant. In this assumption the decreasing of J values reflects the decrease of the exchange coupling intensity and suggests more disordered local environments of Cr^{3+} ions for x > 10 mol % Cr_2O_3.

The composition dependence of the Curie constant, C_M, is presented in Fig. 4.

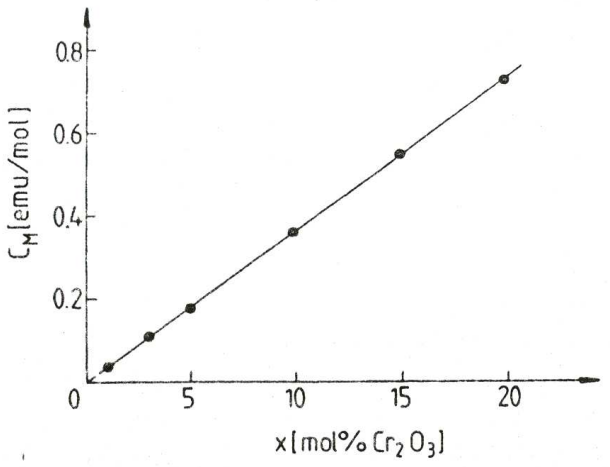

Fig. 4. Composition dependence of the paramagnetic Curie constant, C_M.

The C_M values, which are proportional to the ions concentration, linearly vary with the Cr_2O_3 content.

According to Table 1 the effective magnetic moments $\mu_{eff} = (3.87 \pm 0.02)\ \mu_B$ are very close to the magnetic moment of free Cr^{3+} ions usually obtained in paramagnetic salts containing chromium [30]. Thus, the matrix structure favours the appearance only of Cr^{3+} valence state.

Table 1. Magnetic moments of chromium ions in $xCr_2O_3(100-x)[70TeO_2\ 5B_2O_5\ 5PbO]$ glasses

x [mol % Cr_2O3]	μ_{eff} [μ_B]
1	3.87
3	3.87
5	3.87
10	3.86
15	3.89
20	3.85

CONCLUSIONS

In $xCr_2O_3 \cdot (100-x)[70TeO_2 \cdot 25B_2O_5 \cdot 5PbO]$ glasses with $0 < x \leq 20$ mol % only the presence of Cr^{3+} ions is evidenced. For samples containing $x \leq 3$ mol % magnetically isolated Cr^{3+} ions were evidenced. For higher Cr_2O_3 content a mictomagnetic type behaviour is shown, the predominant superexchange interactions being negative. The intensity of magnetic coupling depends on the ordering degree of the Cr^{3+} ions environment.

REFERENCES

1. V. K. Zakharov and D. M. Yudin, *Soviet Phys. Solid State* 7, 1267 (1965).
2. R. J. Landry, J. T. Fournier and C. G. Young, *J. Chem. Phys.* 46, 1285 (1967).
3. D. Loveridge and S. Parke, *Phys. Chem. Glasses* 12, 19 (1971).
4. I. Ardelean, Gh. Ilonca, M. Peteanu, D. Barbos and E. Indrea, *J. Mat. Sci.* 17, 1988 (1982).
5. O. Cozar, I. Ardelean, I. Bratu, Gh. Ilonca and S. Simon, *Solid State Commun.* 86, 569 (1993).
6. G. Fuxi, D. He and L. Huiming, J. *Non-Cryst. Solids* 52, 135 (1982).
7. J. M. Dance, J. J. Videau and J. Portier, *J. Non-Cryst. Solids* 86, 88 (1986).
8. E. A. Harris, *Phys. Chem. Glasses* 28, 196 (1987).
9. C. Leign, J. Y. Bouzare, J. Emery and C. Jacobony, *J. Phys. Condens. Matter*. 7, 3853 (1995).
10. A. S. Rao, J. L. Rao and J. S. V. Laksman, *Solid State Commun.* 85, 529 (1993).
11. I. Ardelean, O. Cozar. V. Simon and S. Filip, *J. Magn. Magn. Mat.* 157/158, 165 (1966).
12. I. V. Chepeleva, E. R. Zhilinskaya, V. V. Lazukin and A. P. Cernov, *Phys. Stat. Solidi* (b) 73, 65 (1976).
13. J. Moncoujoux, J. Faurie and K. Kohlmuller, *Verres refract.* 31, 47 (1968).
14. Y. Dimitriev, V. Dimitrov and M. Arnaudov, *J. Mat. Sci* 18, 1353 (1983).
15. H. H. Qiu, H. Mori, H. Sakata and T. Hirayama, *Ceram. Soc. Jpn. Int. Ed.* 103, 32 (1995).
16. E. P. Kashchieva, "*Likvatiya v telluritni sistemi*" Thesis, University of Sofia, 1984.
17. I. Ardelean, Gh. Ilonca, M. Peteanu and I. Luca, *Studia Univ. Babeš-Bolyai*, Physica 1, 65 (1979).
18. I. Ardelean, M. Peteanu, Gh. Ilonca, *Phys. Stat. Sol.* (a) 58, K38 (1980).

19. I. Ardelean, Gh. Ilonca, M. Peteanu and D. Pop, *Solid State Commun.* 33, 653 (1980).

20. M. Peteanu, I. Ardelean, S. Filip and F. Ciorcas, *J. Mat. Sci.: Mat. Electronics* 7, 165 (1996).

21. I. Ardelean, M. Peteanu, S. Filip and D. Alexandru, *J. Magn. Magn. Mat.* 157/158, 239 (1996).

22. M. Peteanu, I. Ardelean, V. Simon, S. Filip and G. Györffy, *Studia Univ. Babeš-Bolyai, Physica,* 1996 (in press).

23. M. Peteanu, S. Filip, V. Simon, N. Mureşan and I. Ardelean, *J. Mat. Sci. Tec*h. (submitted).

24. P. A. Beck, *Met. Trans.* 2, 2015 (1971).

25. C. M. Hurd, *Contemp. Phys.* 23, 469 (1982).

26. J. T. Fournier, R. J. Landry and R. H. Bartam, *J. Chem. Phys.* 55, 2522 (1971).

27. E. J. Friebele, N. C. Koon, L. K. Wilson and D. L. Kinser, *J. Am. Ceram. Soc.* 57, 237 (1974).

28. L. F. Bates, *Modern Magnetism,* Cambridge University Press London, 1962, p. 133.

29. I. Ardelean, E. Burzo, D. Mãtulescu-Ungur and S. Simon, J. Non-Cryst. Solids 146, 256 (1992).

30. E. Burzo, *Fizica fenomenelor magnetice,* vol. 1, p. 241, Ed. Acad. Bucureşti, 1979.

STUDIA UNIVERSITATIS BABEŞ-BOLYAI, PHYSICA, XLI, 2, 1996

EPR OF Mn^{2+} IONS IN $2B_2O_3 \cdot SrO$ GLASSES

M. PETEANU[1], I. ARDELEAN[1], V. SIMON[1], S. FILIP[2], M. FLORA[2]

ABSTRACT. The Mn^{2+} ions distribution on different structural units of the $2B_2O_3 \cdot SrO$ glasses was revealed by means of EPR. Octahedral symmetric sites tetragonally distorted were detected, and also the progressive clustering of Mn^{2+} ions at high manganese content.

INTRODUCTION.

Manganese ions were frequently used as paramagnetic probes for exploring the structure and properties of amorphous vitreous systems. Many oxide glasses so as borate [1-5], alkali-silicate [6, 7], alumino-silicate or phosphate [8], tellurite [9, 10] and also chalcogenide [11-13] or halide glasses [14-16], were investigated by means of EPR due to Mn^{2+} ions. The effort was primarily done on elaborating the theoretical support for explaining the absorption lines at $g \cong 4.3$ and $g \cong 3.3$ in the Mn^{2+} absorption spectra. There are also valuable information concerning the structural details of the investigated glasses revealed by the distribution of Mn^{2+} paramagnetic ions on different structural units building the vitreous matrix, their coordination, the valence state, etc. There are systems where besides Mn^{2+} ions, the Mn^{3+} species were also detected [17-19].

Strontium borate glasses were studied by means of EPR [4], and also by ^{11}B nuclear magnetic resonance, infrared spectroscopy and hardness measurements [20].

This paper aims to present our results concerning the EPR of Mn^{2+} ions in $2B_2O_3 \cdot SrO$ glasses revealing interesting aspects.

EXPERIMENTAL.

Glasses of the system $xMnO \cdot (1-x)[2B_2O_3 \cdot SrO]$ were prepared within $0.005 \leq x \leq 0.5$ mol by using reagent grade oxides. The mixtures having suitable proportions, corresponding to the desired concentration of MnO, were mechanically homogenized and melted in sintered corundum crucibles, in an electrical furnace, at 1150^oC.

---

[1] Babeş-Bolyai University, Faculty of Physics, 3400 Cluj-Napoca, Romania.
[2] University of Oradea, Faculty of Sciences, 3700 Oradea, Romania.

The molten material was maintained at this temperature for 30 min. to homogenize by means of thermal convection, then was quenched at room temperature by pouring on a stainless-steel plate. Typical glasses in both aspect and structure were obtained having the gradual coloration specific to manganese within the investigated range of concentration.

The EPR measurements were performed by using a JEOL-type spectrometer, with 100 KHz field modulation. The absorption spectra were recorded at room temperature, in the X frequency band. Samples were powdered and studied in tubular sample holders of the same caliber.

EXPERIMENTAL RESULTS. DISCUSSION.

The detected EPR absorption spectra evidenced the Mn^{2+} ($3d^5$, $^6S_{5/2}$) paramagnetic ions, within the investigated concentration range. The structure of the absorption spectra strongly depends on the MnO content of the sample, and may be observed in Fig. 1. For samples with low Mn^{2+} concentration the spectrum consists in absorptions centered at values of 4.30, 3.33 and 2.02 of the effective g factor. The absorption at $g \cong 2.02$ is the prevalent part of the spectrum having the hyperfine structure (hfs) characteristic for the Mn^{55} ($I = 5/2$) isotope well resolved for $0.005 \leq x \leq 0.03$ mol (Fig. 1.a).

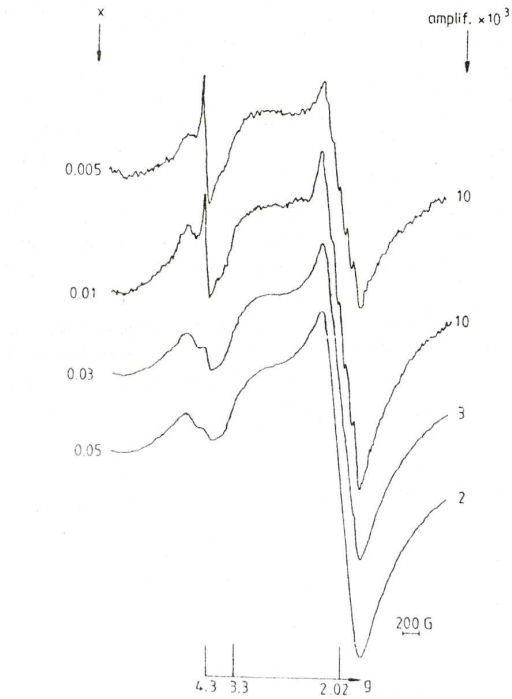

Fig.1.a. EPR absorption spectra due to Mn^{2+} ions in vitreous matrices of the system $2B_2O_3 \cdot SrO$ at low MnO content.

At high manganese content (Fig. 1.b) the spectrum reduces to a single absorption line, without hfs, centered at g ≅ 2.0.

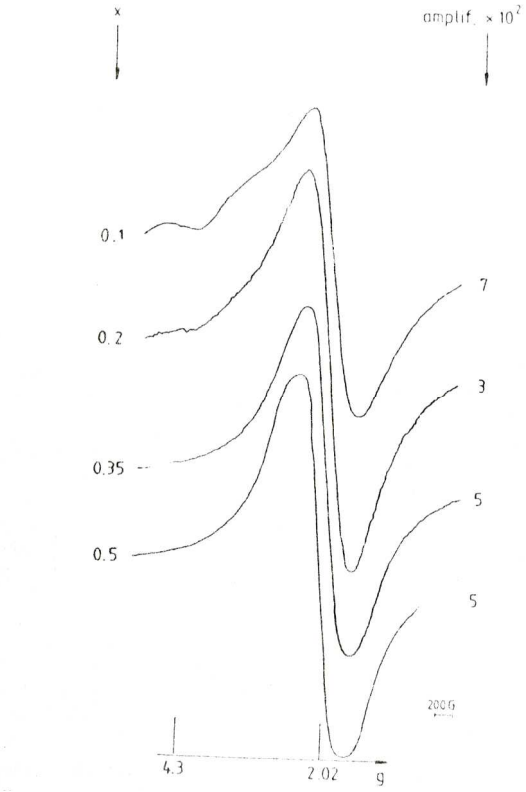

Fig.1.b. EPR absorption spectra due to Mn^{2+} ions in vitreous matrices of the system $2B_2O_3$·SrO at high concentration of Mn.

The absorptions at g ≅ 4.3 are less intense and do not show any hfs. Their evolution may be followed in Fig. 2. The absorption signal is broadened due to the unresolved hfs.

The absorption intensity increases in the $0.005 \leq x \leq 0.05$ mol concentration range, and then decreases until the complete disappearing. Superimposed on this broad absorption, the line corresponding to accidental impurities of Fe^{3+} ($3d^5$, $^6S_{5/2}$) ions was also detected. Being narrow and well resolved, this line has been used as a field marker of the spectrum, being positioned at the well known g = 4.285 value [21].

The absorption centered a g ≅ 3.33 was detected for the $0.005 \leq x \leq 0.1$ mol range. It is a broaden, unresolved line and do not show any hfs.

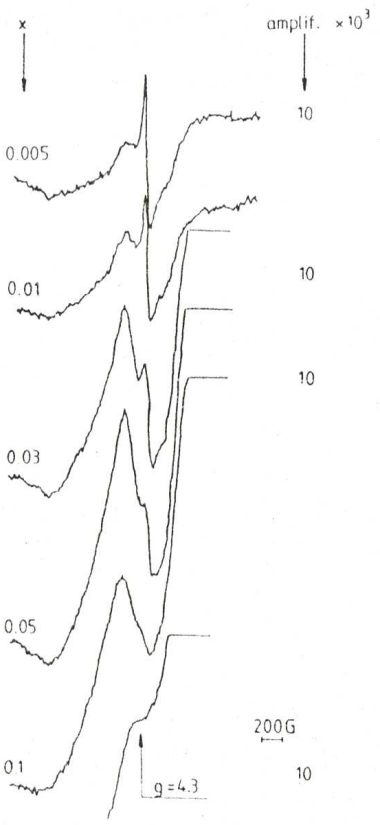

Fig. 2. The g≅ 4.3 absorptions evolution when the Mn^{2+} ions concentration increases in the sample.

As previously mentioned, only the g ≅ 2.02 absorption has a well resolved hfs. The resolution depends on the Mn^{2+} ions concentration in the sample, as may be seen in Fig. 3.

The best resolution was obtained for the lowest paramagnetic ions content providing the optimal opportunity in positioning the lines of the hfs sextet, and evaluating the EPR parameters of the absorption line. For these spectra the hyperfine coupling constant, A, was approximated as separation between the lines of the central pair of the hfs sextet, and the g factor was calculated at the middle point of this. The separation between the hfs lines, ΔH_{hfs}, increases with the magnetic field. This suggests second order terms to be taken into account in the spin Hamiltonian in an accurate theoretical approach.

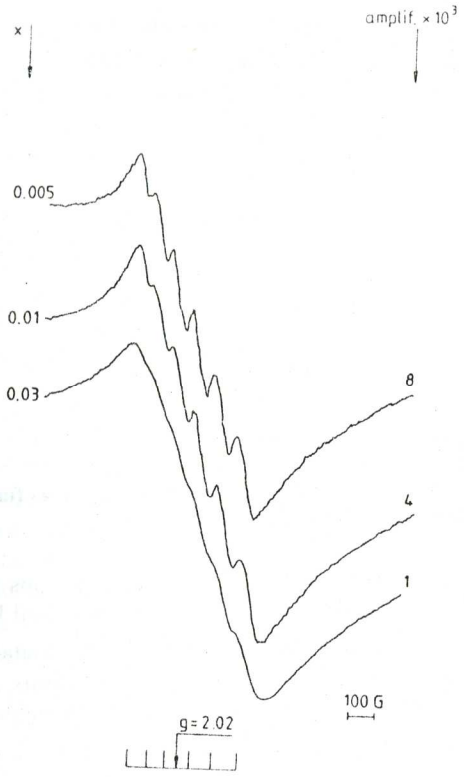

Fig. 3. The evolution of the hfs at the g≅2.0 absorption when increasing the Mn^{2+} ions concentration.

The hfs smears progressively when the Mn^{2+} ions concentration increases (Fig. 3) due to the dipolar broadening of the EPR absorption line, and the crystal field parameters fluctuation [15].

The hfs sextet superimposes on a large absorption line, the envelope of all contributions at absorptions having g ≅ 2.0. This last one depends on the manganese content of the sample. The concentration dependence of the line-width corresponding to this absorption is presented in Fig. 4.

The g ≅ 2.0 absorption was generally attributed to isolated paramagnetic centers in octahedral symmetric sites, slightly tetragonally distorted, or to exchange coupled pairs of ions [22]. Depending on concentration, our samples show an evolution of the vitreous matrix structure from structural units involving Mn^{2+} ions in well defined vicinities, of a certain symmetry, to structural aggregates containing clustered ionic formations.

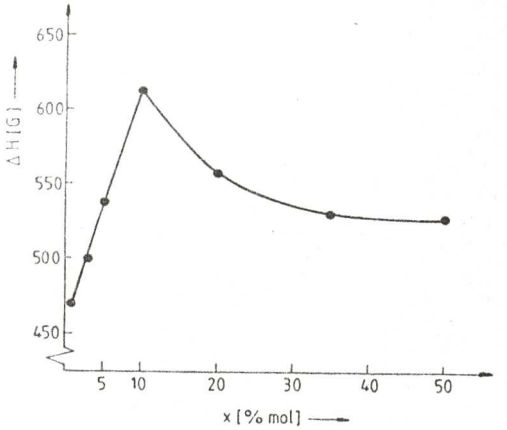

Fig. 4. The variation of the g≅2.0 absorption line-width as function of the manganese content of the sample.

Within the low concentration range of paramagnetic ions (Fig. 1.a) the g ≅ 2.0 absorption is prevalent in the spectrum, having a well resolved hfs. The hyperfine sextet is due to isolated Mn^{2+} ions in high symmetric sites (octahedral), separated well enough from each other to avoid strong dipolar interactions. The g factor and hyperfine coupling constant values and the well resolved hfs support this statement, and also evidence the predominantly ionic character of the bonding between Mn^{2+} ions and the O^{2-} ions generating the octahedral symmetric ligand field. There are weak axial distortions superimposed on this field, varying from one vicinity to another [23, 24]. Their random orientation determine the absorption line broadening. The random distribution of Mn^{2+} ions in the vitreous matrix together with this broadening give the large envelope at g ≅ 2.0 having superimposed the hfs sextet.

When the paramagnetic ions concentration increases the hfs smears out, and the intensity of the broad, symmetric absorption at g ≅ 2.0 increases. Its line-width follows the evolution given in Fig. 4. Within 0.005 ≤ x ≤ 0.1 mol MnO the absorption progressively broadens evidencing dipole-dipole type interactions between the Mn^{2+} ions. For x > 0.1 mol MnO the line suddenly narrows, evidencing magnetic exchange type mechanisms between Mn^{2+} ions close enough to each other for interacting. The reached doping level of the sample imposes the progressive clustering of Mn^{2+} ions. For x > 0.25 mol MnO the narrowing is balanced by the line broadening due to another mechanisms like the interaction between mixed valence states of manganese, or the progressive disordering of the vitreous system. At high MnO content, besides Mn^{2+}

species, the only ones giving rise to EPR absorption in our experimental conditions, superior valence states may occur in the sample. In vitreous oxide matrices Mn^{3+} ions were frequently reported as progressively involved when increasing the MnO content [17-19]. The interaction between Mn^{2+} and Mn^{3+} ions in their neighbourhood gives the EPR absorption line broadening.

Due to distortions, inherent in glasses, the ligand field in the paramagnetic ion vicinity is not perfectly cubic. This field act via the spin-orbit coupling on the Zeeman splitting of the ground state level. The strongly distorted versions of the vicinity are characterized by strong crystal field effects inducing large splittings between the multiplet levels in zero magnetic field. The microwave field quanta is inefficient in inducing transitions at resonance, between these levels. Transition will be induced between the levels of the same multiplet as splitted by the static magnetic field, and corresponding to absorptions positioned by $g_{eff} >> 2.0023$ values.

In the case of our samples, the strongly distorted versions of the octahedral vicinity of Mn^{2+} ions give the resonant absorptions at $g \cong 4.3$ and $g \cong 3.33$ (Fig. 1.a). According to the recorded spectra, the weight of these absorptions is small and their hfs unresolved. This proves a relative small concentration of Mn^{2+} ions involved in such structural units. The absorptions at $g \cong 4.3$ and $g \cong 3.33$ reach their maximum intensity for approximately 0.05 mol MnO. The further increasing of the MnO content of the sample reduces the isolated ions possibilities to arrange their vicinity, so that the structural units of Mn^{2+} in low symmetric crystal field become less represented, and the paramagnetic ions are gradually involved in clusters. The clustering process generalizes for a manganese content exceeding 0.1 mol MnO.

From the variety of symmetries of the Mn^{2+} ion vicinity efficient in the $^6S_{5/2}$ state splitting [25, 26] we selected those for which the theoretical isotropic g_{eff} values of 4.285 and 3.33 are very close to those experimentally detected. The tetragonal and tetragonally distorted cubic vicinities are of particular interest, for which both values of the isotropic g factor (4.285 and 3.33) may be theoretically obtained. Isotropic $g = 3.33$ values, corresponding to transitions within the lowest doublet, where theoretically obtained, in the strong ligand field approximation, even for an undistorted cubic field case [26].

A characteristic of the absorption lines detected at $g \cong 4.3$ and $g \cong 3.3$ is their weak resolution and lack of hfs. This is principally due to fluctuations of the ligand field parameters in the paramagnetic ion neighbourhood and the random distribution of the cubic vicinity distortions. Some of the low-symmetry centers no more contribute to the isotropic absorption and the resulting EPR line is broadened due to anisotropy and the ligand field parameters distribution. The trigonal symmetric vicinities and those of trigonal distorted cubic symmetry of the Mn^{2+} ion, may give anisotropic absorptions having the $g \cong 3.33$ value for one of the components of the g factor [26]. All these contributions result in the absorption line broadening and an unresolved hfs.

CONCLUSIONS.

By means of EPR measurements, Mn^{2+} species were detected in glasses of the system $xMnO\cdot(1-x)[2B_2O_3\cdot SrO]$ within $0.5 \leq x \leq 50$ mol % MnO.

For samples with a low MnO content ($0.5 \leq x \leq 5$ mol %) isolated Mn^{2+} paramagnetic ions were detected in sites of octahedral symmetry slightly tetragonally distorted. They give rise to intense absorptions lines at $g_{eff} \cong 4.3$, and $g_{eff} \cong 3.33$ values. The weight of these lines in the spectrum is small enough to suggest a relatively low content of Mn^{2+} species involved in such vicinities.

For a high manganese content ($5 \leq x \leq 50$ mol % MnO) the progressive clustering of Mn^{2+} ions was observed. The resulted aggregates give the intense absorption line centered at $g_{eff} \cong 2.0$ having a peculiar dependence on concentration of its line-width: a dipolar broadening within $0.5 \leq x \leq 10$ mol % MnO and a superexchange narrowing for $x > 10$ mol % due to magnetic interactions between the Mn^{2+} ions involved in clusters.

REFERENCES

1. D. L. Griscom, R. E. Griscom, *J. Chem. Phys*. 47, 2711 (1967).
2. R. D. Dowsing, J. F. Gibson, *J. Chem. Phys.* 50, 294 (1969).
3. A. W. De Wijn, R. E. Van Balderen, *J. Chem. Phys*. 46, 4 (1967).
4. P. C. Taylor, P. J. Bray, *J. Chem. Phys. Solids* 33, 43 (1972).
5. I. Ardelean, Gh. Ilonca, M. Peteanu, *Solid State Commun*. 52, 147 (1984).
6. H. H. Wickman, M. P. Klein, D. A. Shirley, *J. Chem. Phys*. 42, 2113 (1965)
7. D. Loveridge, S. Parke, *Phys. Chem. Glasses* 12, 19 (1971)
8. J. W. H. Schreurs, *J. Chem. Phys.* 69, 2151 (1978)
9. M. Peteanu, I. Ardelean, Al. Nicula, *Rev. Roum. Phys*. 28, 47 (1983)
10. I. Ardelean, M. Peteanu, Gh. Ilonca, *Phys. Stat. Sol*. (a) 58, K33 (1980)
11. R. C. Nicklin, C. P. Poole, H. A. Farach, *J. Chem. Phys*. 68, 2579 (1973)
12. V. N. Lazukin, I. V. Chepeleva, DAN SSSR 214, 787 (1974)
13. V. Chepeleva, E. A. Zhlinskaya, V. N. Lazukin, A. P. Cernov, V. I. Olkhovskii, *Phys. Stat. Sol.* (b) 82, 189 (1977)
14. B. Petrova, M. Frumar, E. Cernoskova, V. Cerny, *J. Non-Cryst. Solids* 161, 316 (1993)
15. V. Cerny, B. Petrova, M. Frumar, *J. Non-Cryst. Solids* 125, 17 (1990)

16. V. Cerny, B. Frumarova-Petrova, J. Rosa, I.L. Lieholit, M. Frumar, *J. Non-Cryst. Solids* 192 & 193, 165 (1995).
17. Gh.Ilonca, I.Ardelean, O.Cozar, *J. Physique* 49, 8 (1988).
18. I.Ardelean, Gh.Ilonca, O.Cozar, *Rev. Roum. Phys.* 33, 179 (1988).
19. I.Ardelean, M.Peteanu, S.Filip, D.Alexandru, *J. Magn. Magn. Mat.* (to be published).
20. S.J.Moon, M.S.Kim, S.J.Chung, H.T.Kim, *J. of the Korean Phys.* Soc. 29, 213 (1996).
21. T.Castner, G.S.Newell, W.C.Holton, C.P.Slichter, *J. Chem. Phys.* 32, 668 (1960).
22. D.L.Griscom, *J. Non-Cryst. Solids* 40, 211 (1980).
23. I.N.Feuerhelm, S.M.Sibley, W.A.Sibley, *J. Solid State Chem.* 54, 164 (1984).
24. J.L.Rao, B.Sreedhar, Y.C.Ratnakar, S.V.J.Lakshmann, *J. Non-Cryst. Solids* 92, 175 (1987).
25. M.Peteanu, Al.Nicula, *Studii şi Cercet. de Fizicã* 33, 29 (1981).
26. M.Peteanu, Al.Nicula, *Studii şi Cercet. de Fizicã* 34, 14 (1982).

STUDIA UNIVERSITATIS BABEŞ-BOLYAI, PHYSICA, XLI, 2, 1996

SPIN FLUCTUATIONS IN (1-x)$USi_{1.88}$x$DySi_2$ SYSTEMS

I. LUPŞA[1], P. LUCACI[1], M. MARCU[2]

ABSTRACT. The magnetic and structural properties of (1-x)$USi_{1.88}$x$DySi_2$ systems were studied. The low temperature magnetic behaviour of $USi_{1.88}$ was discussed in the spin fluctuations model. The uranium substitution by dysprosium leads to the appearance of the antiferromagnetical ordered phase and in addition the quenching of spin fluctuations is evidenced.

INTRODUCTION

The $USi_{1.88}$ structure was reported to be of so called disordered tetragonal $ThSi_2$ type [1]. The magnetic susceptibility closely fits a Curie-Weiss law with μ_{eff}=3.53 μ_{eff}/U_{atom} , close to that of uranium $U^{4+}(5f^2)$ free ion value. A slight positive deviation occurs below 100 K and a constant Van Vleck type paramagnetism is reported below 10 K [1].

The $DySi_2$ compound crystallizes in a tetragonal structure of $ThSi_2$ type having lattice constants a=0.3974nm and c=1.3676nm [2]. The magnetic measurements indicate that $DySi_2$ is an antiferromagnetic having T_N=17K and the effective magnetic moment 10.4 μ_B [3].

In this paper we report the magnetic properties of (1-x)$USi_{1.88}$x$DySi_2$ systems in connection with their structure.

EXPERIMENTAL RESULTS

The samples were melted in an arc furnace in a purified argon atmosphere. Then they were thermally treated in vacuum at 1200 K during one week. X-ray analyses show that the compounds have tetragonal symmetry of $ThSi_2$ type. The lattice parameters have values between those of $DySi_2$ and $USi_{1.88}$ which are very close each other.

The temperature dependence of $USi_{1.88}$ susceptibility is presented in figure 1.

The $USi_{1.88}$ compound shows at low temperatures a maximum at 14 K in agreement with previously reported data. Over this temperature the χ values are decreasing and above T^*=80K the susceptibility follows a Curie-Weiss law: χ=C/(T-θ). We denoted by C the Curie constant and θ is the paramagnetic Curie temperature.

By fitting the experimental results we obtained C,and θ values. The Curie molar constant is 1.6 emuK/mol and θ=-386K. The effective magnetic moment is 3.57μ_B/Uatom.

[1] Technical University, 3400 Cluj-Napoca.
[2] Babeş-Bolyai University, 3400 Cluj-Napoca.

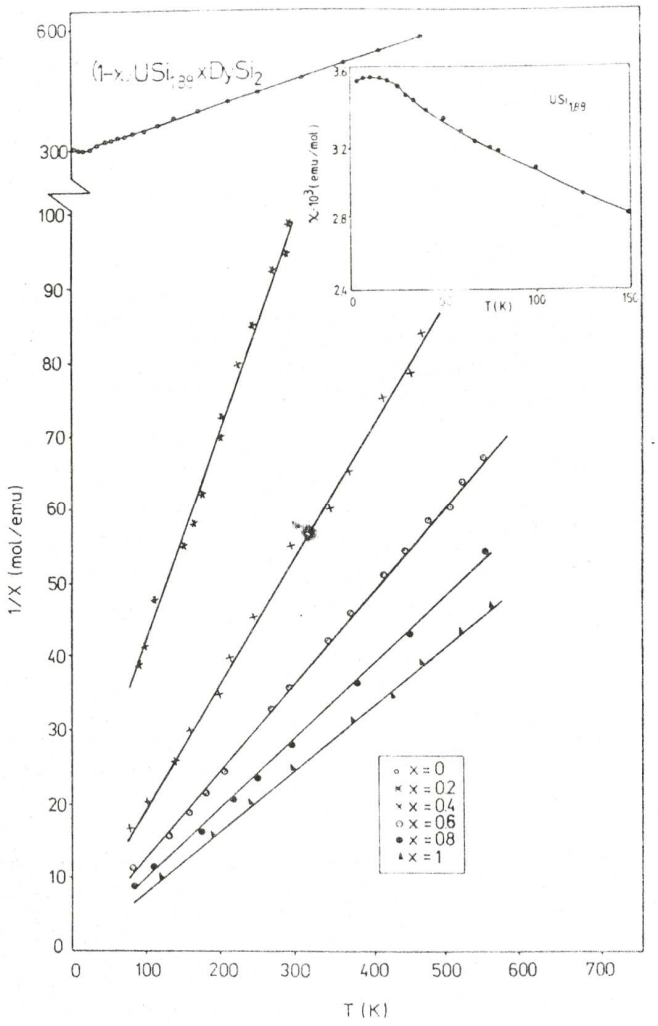

Fig.1. The temperature dependence of the reciprocal susceptibility of(1-x)$USi_{1.88}$x$DySi_2$ systems. The thermal variation of $USi_{1.88}$ susceptibility in the low temperature range is presented in inset.

The systems where uranium is substituted by dysprosium show also a Curie-Weiss type behaviour (fig.1). The molar Curie constants calculated in accord with Curie-Weiss law are increasing as the dysprosium content is increasing up to the value of 13.53 emuK/mol corresponding to $DySi_2$. The paramagnetic Curie temperatures are negative and are rapidly decreasing in absolute magnitude from -386K to -40K for x=0.2 as it seen in figure 2.

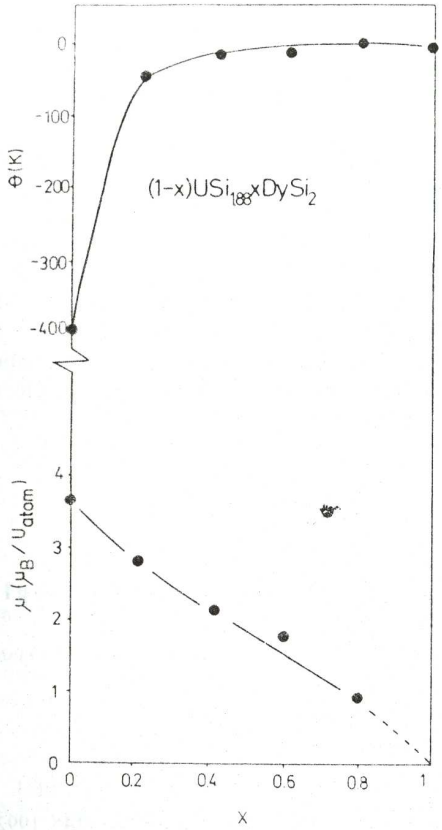

Fig.2. The composition dependence of θ values,of the Curie constants and of the μ_{eff}/U_{atom} values for (1-x)$USi_{1.88}xDySi_2$ systems.

Assuming that the contribution of Dy ions to the Curie constants are the same as those of free Dy^{3+}, the effective uranium moments were determined. The effective magnetic moments attributed only to uranium atoms are decreasing from 3.57 μ_B to 0.5 μ_B for x=0.8; an almost linear decreasing of these values with dysprosium composition is evidenced
(fig 2).

DISCUSSION

The transition from a nearly temperature independent susceptibility to a Curie-Weiss type behaviour at temperature $T>T^*=80$ K suggests the presence of spin fluctuations. This behaviour is supported also by the high negative paramagnetic Curie temperature. The effective magnetic moment is close to that of $U^{4+}(5f^2)$ free ion.

The magnetic behaviour of this system may be analyzed in the self consistent renormalization (S.C.R.) theory of spin fluctuations [4-6]. The wave number dependent

susceptibility χ_q has large enhancement due to electron-electron interaction only for small q, for which temperature dependence is significantly. The average mean square amplitude of the local spin fluctuations

$$< S^2_{loc} >= 3_{k_b} T \sum_q \chi_q$$

Error! Switch argument not specified.increases with increasing temperature until it reaches an upper limit determined by the charge neutrality condition at T^*=80K. At $T > T^*$ $USi_{1.88}$ behaves as if having a local moment. The nearly same magnetic behaviour was observed in $U(LaAl)_4$ compound [7].

The decreasing of the μ_{eff}/U_{atom} as well as ·θ·**Error! Switch argument not specified.** values indicates a gradual quenching of spin fluctuations when uranium content is decreasing.

As dysprosium content is greater, an antiferromagnetic order is present proving the increasing of change interactions.

A similar situation, a superposition of spin fluctuations behaviour and an antiferromagnetic order was reported in $(UR)Al_3$ systems where R=Gd or Dy [8].

REFERENCES

1. K.Remschnig, T.Le Bihan, H.Noel, and P.Rogl, *J. Solid State Chem.* 97, 3921, 1992.
2. P.Villars and L.D.Calvert, *Pearson's Handbook of Crystallographic* and *Data for Intermetallic Phases*, 1991.
3. K.N.R.Taylor, *Adv. Phys.* 20, 87, 551, 1971.
4. T.Moriya, *J. Magn. Magn. Mater.*14.1, 1979.
5. T.Moriya and A.Kawabata, *J. Phys.Soc.Jpn.*34. 635, 1973.
6. E.Burzo and R.Lemaire, *Solid State Commun.* 84. 1145, 1992.
7. I.Lupşa, P.Lucaci and Mihaela Danciu, Studia Univ.Babeş-Bolyai, *Physica,* XXXIX, 2, 1994.
8. P.Lucaci, E.Burzo and I.Lupşa, *J. Alloys and Compound*, 238.L4, 1996.

STUDIA UNIVERSITATIS BABEŞ-BOLYAI, PHYSICA, XLI, 2, 1996

THE MAGNETIC BEHAVIOUR OF $xUCo_2(1-x)USi_{1.88}$ SYSTEMS

P. LUCACI[1]

ABSTRACT. The magnetic properties of $xUCo_2(1-x)USi_{1.88}$ systems in the 77-500 K temperature range were studied. The reciprocal susceptibilities follow a modified Curie-Weiss law. As silicon is substituted by cobalt the paramagnetic Curie temperatures are decreasing in absolute magnitude as well as the effective magnetic moments of uranium atoms. The magnetic behaviour of the above system is discussed in the spin fluctuations model. A gradual silicon substitution by cobalt leads to a quenching of spin fluctuations.

INTRODUCTION

The $USi_{1.88}$ crystallizes in a tetragonal structure of $ThSi_2$ type [1]. The magnetic susceptibility above 100 K follows a Curie-Weiss law with $\mu_{eff}=3.53\ \mu_{eff}/U_{atom}$, close to that of uranium free value. A nearly temperature independent paramagnetism is reported below 10 K [1].

The UCo_2 compound crystallizes in a cubic symmetry of $MgCu_2$ type [2]. This compound shows a temperature independent susceptibility (10^{-3} emu/mol) [3].

We substituted silicon by cobalt in order to analyze the structural and magnetic properties of $xUCo_2(1-x)USi_{1.88}$ systems.

EXPERIMENTAL RESULTS

The samples were melted in an arc furnace in a purified argon atmosphere. Then they were thermally treated in vacuum at 1200 K during one week. X-ray analyses show that the compounds have tetragonal symmetry, of $ThSi_2$ type, for composition $x \leq 0.8$.

The magnetic measurements were performed in the 77-500 K temperature range. For $USi_{1.88}$ in the low temperature domain we used the measurements of Remschnig [1] superposed on our data obtained for T>77 K. The reciprocal susceptibilities as a function of temperature are plotted in figure 1. In inset is plotted the temperature dependence of the susceptibility for $USi_{1.88}$ compound. A maximum at ~ 10 K is shown. Above this temperature the χ values are decreasing and for $T>T^*=80K$ the susceptibility follows a Curie-Weiss law. The magnetic behaviour of the system $xUCo_2(1-x)USi_{1.88}$ obeys a modified Curie-Weiss law: $\chi= \chi_o+C/(T-\theta)$. We denoted by χ_o the temperature independent term, C represents the Curie constant and θ is the paramagnetic Curie temperature.

[1] Technical University, 3400 Cluj-Napoca.

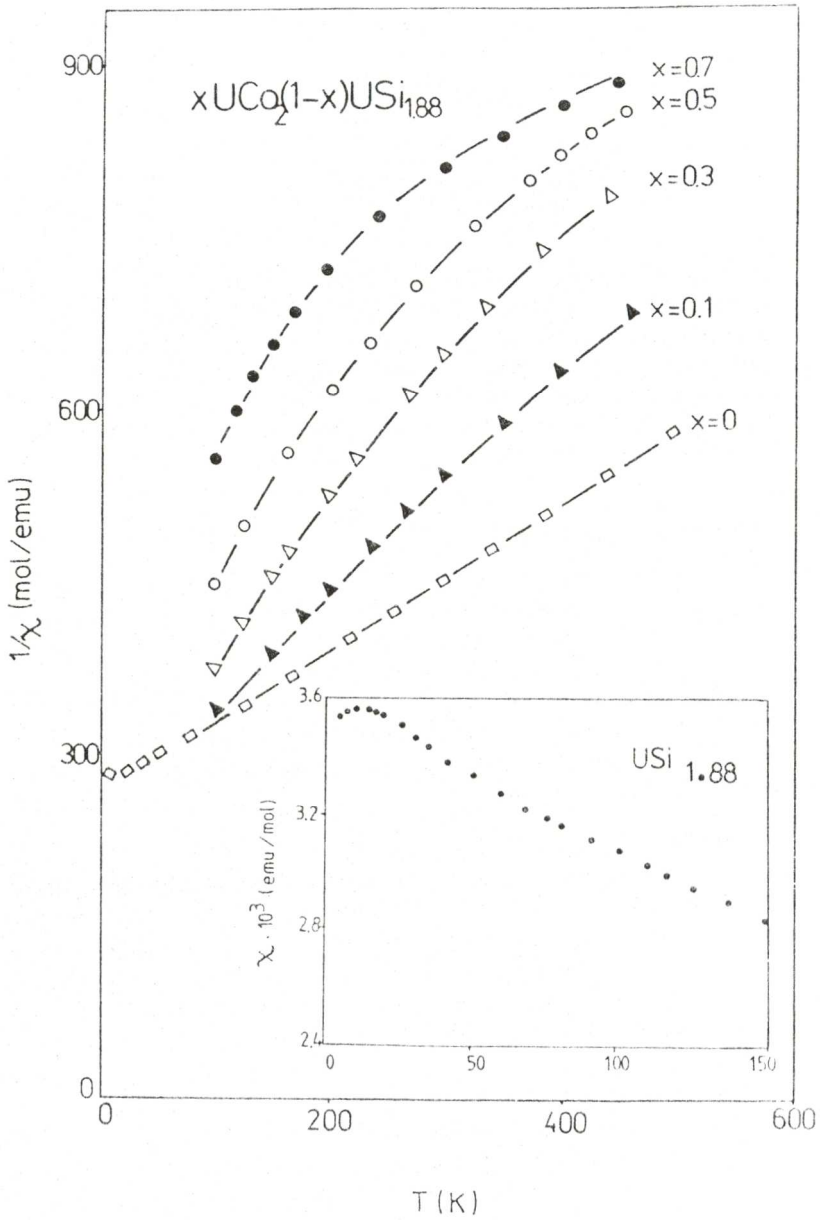

Fig.1. The temperature dependence of the reciprocal susceptibility of $xUCo_2(1-x)USi_{1.88}$ systems. The thermal variation of $USi_{1.88}$ susceptibility in the low temperature range is presented in inset.

By fitting the experimental results we obtained χ_o, C, θ. The composition dependence of χ_o, θ and μ_{eff} values are plotted in figure 2. The paramagnetic Curie temperatures are negative for $x \leq 0.8$ and are increasing from -386 K, characteristic to $USi_{1.88}$ to -20 K for x=0.8.

The effective magnetic moments are decreasing from $3.57\mu_B$ for $USi_{1.88}$ to zero value for UCo_2. The temperature independent term of the susceptibility is almost linearly increasing to 1.1 10^{-3} emu/mol characteristic for UCo_2.

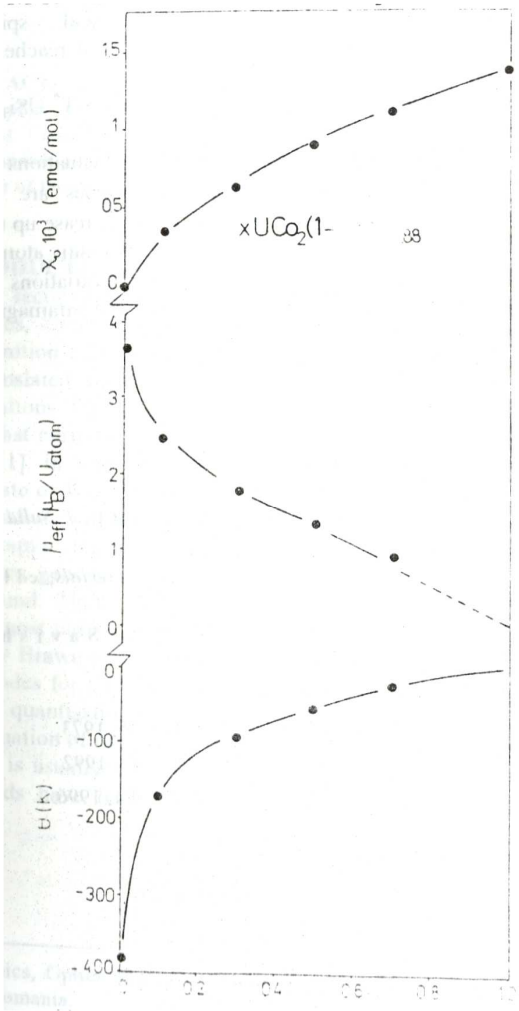

Fig.2. The composition dependence of χ_o,θ and μ_{eff}/U_{atom} values for $xUCo_2(1-x)USi_{1.88}$ systems.

DISCUSSION

The $USi_{1.88}$ compound has a maximum in the susceptibility values at ~ 10 K. Over 80 K a Curie-Weiss law is followed. The paramagnetic Curie temperature is negative (-386 K). The effective magnetic moment is $3.57\mu_B$ as expected for U^{4+} free ion. These facts support that $USi_{1.88}$ is a spin fluctuations system. The magnetic properties of this compound may be analyzed in the self consistent renormalization (S.C.R.) theory of spin fluctuations [4-6]. The wave number dependent susceptibility χ_q has large enhancement due to electron-electron interaction only for small q, for which temperature dependence is significantly. The average mean square amplitude of the local spin fluctuations $< S_{loc}^2 >= 3k_B T\sum_q \chi_q$ **Error! Switch argument not specified.**increases with increasing temperature until it reaches an upper limit determined by the charge neutrality condition at T^*=80K. At $T > T^*$ $USi_{1.88}$ behaves as if having a local moment.

Substituting silicon by cobalt a superposition of spin fluctuations behaviour and a Pauli paramagnetism is evidenced. As x is higher χ_o values are increasing. The paramagnetic Curie temperatures are negative for $x \leq 0.8$ and increase up to zero value for x=0.8. The effective magnetic moments are attributed to uranium atoms and they are decreasing when cobalt content is greater. These composition variations of χ_o,θ and μ_{eff} values indicate the transition from spin fluctuations to a Pauli type paramagnetism.

REFERENCES

1. K. Remschnig, T. Le Bihan, H. Noel, P. Rogl, *J. Solid State Chem.* 97, 3921, 1992.
2. V. Sechovsky, L. Havela in *Ferromagnetic Materials*, ed.E. P. Wohlfarth, vol.4, North Holland Publ. Comp., 1988.
3. V. F. Chechernikov, V. A. Pletyushin, T. M. Savishvilli, V. K. Slovyanskij, *J. Exp. Theor. Phys.* 58, 80, 1970.
4. T. Moriya, *J. Magn. Magn. Mater*. 14. 1, 1979.
5. T. Moriya, A. Kawabata, *J. Phys. Soc. Jpn.* 34. 635, 1973.
6. E. Burzo, R. Lemaire, *Solid State Commun*. 84. 1145, 1992.
7. P. Lucaci, E. Burzo, I. Lupşa, *J. Alloys and Compound*, 238. L4, 1996.

STUDIA UNIVERSITATIS BABEŞ-BOLYAI, PHYSICA, XLI, 2, 1996

IMPROVEMENT OF CORRELATION FILTERS USING A NEW COMPUTER GENERATED HOLOGRAM METHOD

M. GILOAN[1], S. ASTILEAN[1]

ABSTRACT. This paper presents an improved correlation filter based on a new graphic code for computer generated hologram that we have already proposed. Computer simulations and comparison with other graphic-codes for computer generated holograms are performed. Using our method the response of the correlation filter was improved by 44 %.

INTRODUCTION

Pattern recognition is a large field of which aim is to identify certain structures (images, sounds, different signals). One of the most powerful method used in pattern recognition is the correlation. Through correlation one image is compared with all the translated versions of another image. This technique requires a great amount of operations. Optical correlators are characterised by a massive parallelism that leads to a fast correlation. The first optical correlator was proposed by Van der Lugt in 1960's [1]. In Van der Lugt-type optical the correlation filter has to be the complex conjugate of Fourier transform of the reference pattern (see Fig. 1). Because the Fourier transform of the reference pattern has complex values the computer generated hologram technique is used to record the complex filter function.

Computer generated holograms (CGH) consist on transparent dots on an opaque background. They have a cellular structure each cell encoding a complex amplitude. The most famous technique used to design computer generated holograms was proposed by Brawn and Lohmann and is known as detour phase-technique [2]. Other graphic codes for CGH have been proposed [3-6], each graphic code allows a finite number of quantisation states in complex plane that leads to quantisation error [7-8]. The information of magnitude and phase of complex amplitude cannot be stored accurately. This is usually the main reason for the bad quality of correlation image. Different methods have been proposed to improve the correlation image quality [9-16].

[1] Faculty of Physics, Optics and Spectroscopy Department, Babeş-Bolyai University, 3400 Cluj-Napoca, Romania.

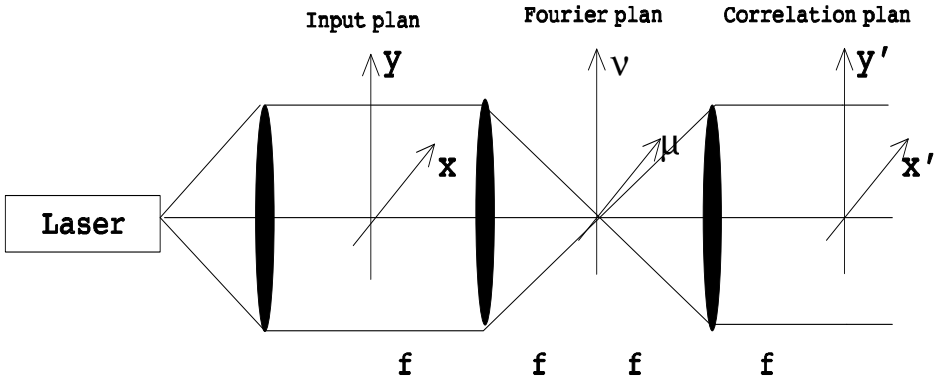

Fig. 1. Optical set-up of Van der Lugt correlator.

In this paper we present the improvement of a correlation filter using a novel technique to design CGH that we have already proposed [17]. The mathematical model of this graphic code and the algorithm to reduce the computation time are reviewed in section 2.1 and 2.2, respectively. Section 3 presents a comparison between our proposed method and the other technique for CGH.

GRAPHIC-CODE FOR CELL-ORIENTED HOLOGRAMS

2. 1. Mathematical model

We have considered a cell with five vertical slits of the same height (M=5). In this case a cell can encode a complex amplitude that has the following form:

$$\sum_{m=0}^{4} A_m \exp(j\frac{2\pi}{5}m) \tag{1}$$

where the value A_m represents the magnitude encoded in the m-th slit. Each slit allows N+1 equally spaced magnitude levels. The m^{th} slit encodes a complex number with phase ($2\pi m/5$).

Figure 2 shows the structure of a cell with N=5 and the geometrical interpretation in the complex plane.

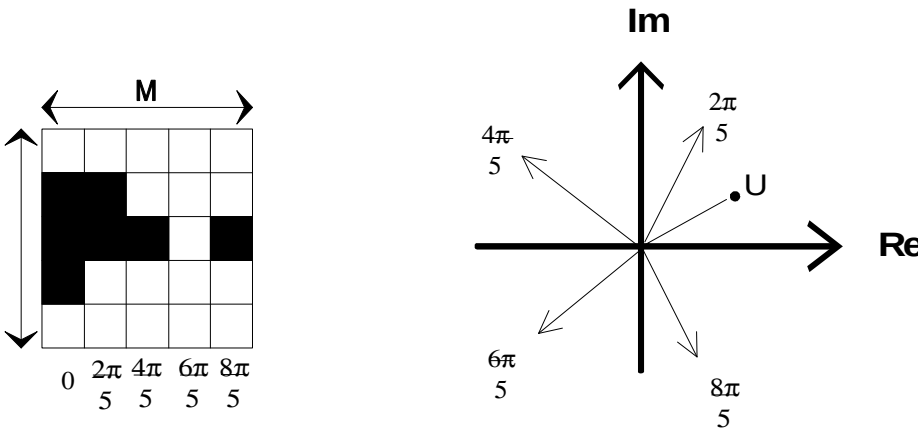

Fig. 2. Structure of the cell and the mathematical model of the proposed graphic-code.

Each distinct combination of A_m (m=0, 1, 2, 3, 4), where at least one of A_0 , A_1, A_2, A_3, A_4 is equal to zero, gives us a distinct quantisation state (e.g. the combination (3, 3, 1, 4, 2) gives the same quantisation state as the combination (2, 2, 0, 3, 1) because $\sum_{m=0}^{4} \exp(j\frac{2\pi}{5}m)$ = 0. The number of distinct combinations of A_m for N+1 magnitude levels is $(N+1)^5$ and excepting the level zero we have N^5 distinct combinations. According to this one can prove that for N+1 magnitude levels we have $(N+1)^5$-N^5 quantisation states. For N=5 we have 4651 quantisation states which are located in circle of radius R = 10 A cos (π / 5), where A is the difference between two adjacent levels of magnitude (see Figure 3).

The problem is to find the combination of A_m which represents the best approximation for the complex amplitude U_{kl},(where U_{kl} is a sample of Fourier transform) according to relation (1). In the next section we present the algorithm to obtain the best approximation for the sample U_{kl}.

2. 2. Algorithm

The algorithm consists in a motion through the quantisation states network towards the true complex amplitude U_{kl}, starting from different random quantisation states (see Fig. 3). This algorithm is proposed to reduce the iteration time required by the generation of all the quantisation states.

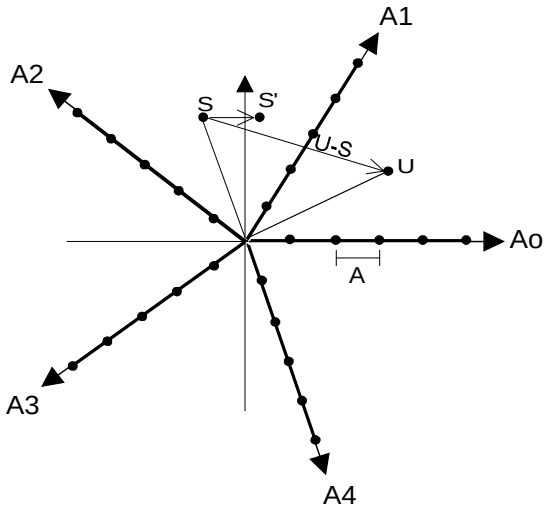

Fig. 3. Graphic presentation of the step 2 operation.

Step 1: Generate a random quantisation state. (A quantisation state is determinate by the values A_m where m = 0, 1, 2 , 3, 4).

Step 2: From the current quantisation state (S) we move towards the complex amplitude U_{kl}. First we calculate the phase of complex number obtained by subtracting S from U_{kl}, namely U_{kl} - S. Then we quantisate this phase on five levels (m=0, 1, 2, 3, 4) and we increase with quantity A the magnitude A_m, (A is a quantity equal with the difference between adjacent levels of magnitude.) In this way we moved to another quantisation state (S'). In order to explore the whole qantization states network this step is repeated for 2N times. The error $\varepsilon = |U_{kl} - S|$ is computed for each intermediate quantisation state and the best approximation is stored.

Step 3: Go to Step 1 or stop if a desired approximation was obtained or after an imposed number of trials.

SIMULATION

In order to compare our proposed method with other method we computed the correlation filters of alphabetical character '**a**' presented in figure 4 (top).

Figure 4 shows the response in the correlation plane obtained by the proposed method (for M=5 and N=5) in a) and Lohmann-type graphic code with eight phase levels and nine magnitude levels, (i.e. M=8 and N=8) in b). The values of intensity at the origin of the correlation plane (normalised to the value for the original non-quantised filter) are 0.99 for the proposed method and 0.55 for Lohmann-type graphic code. Also, the size of the hologram was reduced with respect to the Lohmann-type CGH where a cell has 8x8=64 pixels. This is an important result in frequency truncation

error reduction. Hence the response of the filter was improved in the first case because the quantisation errors was reduced.

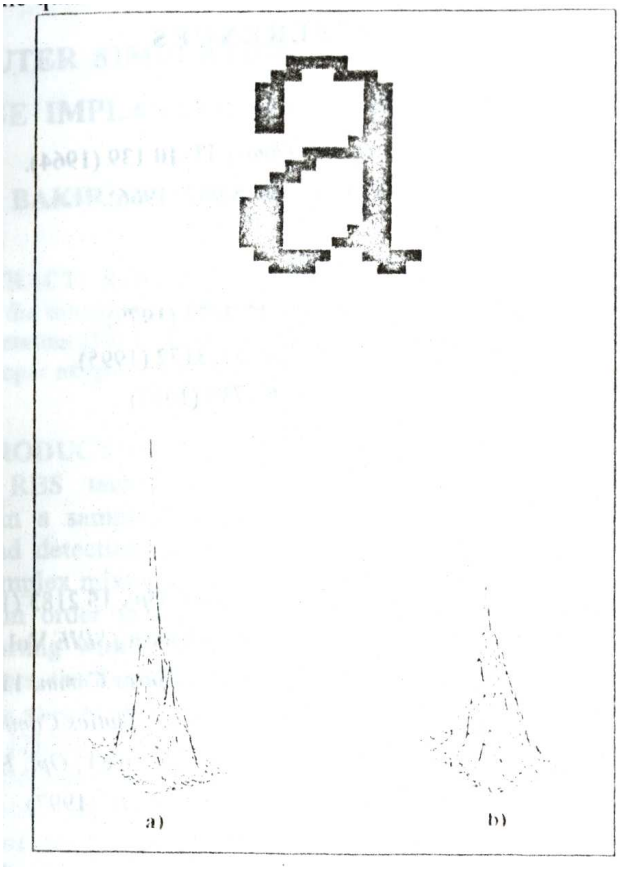

Fig. 4 Alphabetical character used in simulation (top) and computer simulated reconstruction:our method (a) and Lohmann-type method (b).

CONCLUSION

In this paper we have used an earlier proposed graphic-code for CGH in view to improve correlation filters. Our method increases the number of quantisation states although the cell has only 5x5=25 pixels. Using this method the response of the correlation filter was improved by 44 %. On the same mathematical model other algorithms, like simulated annealing, can be used in order to design improved correlation filters.

REFERENCES

1. A. B. Van der Lugt, IEEE *Trans. Inf. Theory* **IT-10** 139 (1964).
2. Brown, A.W. Lohmann, *Appl. Opt.* **5** 967 (1966).
3. Lee, *Appl. Opt.* **9** 369 (1970).
4. Burckhardt, *Appl. Opt.* **9** 1949 (1970).
5. Hsueh, A.A. Sawchuk, *Appl. Opt.* **17** 3874 (1978).
6. Lohmann, S. Linzinger, *Appl. Opt.* **34**, 3172 (1995).
7. Lohmann, D.P. Paris, *Appl. Opt.* **6** 1739 (1967).
8. Gabel, B. Liu, *Appl. Opt.* **9** 1180 (1970).
9. Dalas, *Appl. Opt.* **13** 2274 (1974).
10. Gabel, *Appl . Opt.* **14** 2252 (1975).
11. Allebach , *Appl. Opt.* **20** 290 (1981).
12. Allebach, N.C. Gallagher, B. Liu, *Appl. Opt.* **15** 2183 (1976).
13. Nagarajan, R.L. Easton Jr., R. Eschbach, *SPIE* Vol. **2406**, 318-330.
14. Nagarajan, R. Easton, R. Eschbach, *Optics Comm.* **114** 370 (1995).
15. Weissbach, F. Wyrowski, O. Bryngdahl, *Optics Comm.*. **72** 37 (1989).
16. Moreno, Ch. Gorecki, J. Campos, M.J. Yzuel, *Opt. Eng.* **34** 3520 (1995).
17. Giloan and S. Astilean, *Optics Comm., under press,* (1997).

STUDIA UNIVERSITATIS BABEŞ-BOLYAI, PHYSICA, XLI, 2, 1996

COMPUTER SIMULATION OF RBS SPECTRA FOR HIGH DOSE IMPLANTED OXYGEN IN SILICON SAMPLE

A. M. BAKIR[1], M. BERCU[1], F. CONSTANTIN[2], V. V. GRECU[1]

ABSTRACT. Rutherford backscattering spectrometry (RBS) is used to study the modified composition of silicon samples after oxygen high dose implantation (1017 - 1018 ions/cm^2). The RUMP program is used in fitting the proper oxygen concentration profile and depth range.

INTRODUCTION

The RBS techniques permit to establish the laryer's thickness and composition in a sample [1]. Peack heights, area and widths along with beam parameters and detection are used in order to determine the quantities mentioned above. For complex mixtures of elements with concentration profiles computer's code are required in order to solve them. The RUMP code permits the RBS spectra simulation starting with a sample description; the description includes the sample number of layers, the thickness, the composition and of course the beam and detection geometry; it is able to create one element contribution to the RBS spectra along the global spectra [2],[3].

The ion beam implantation is a versatile method in forming stoichiometric or nonstoichiometric compounds; this techniques is used in improving the microhardness and adhesion of thin layers deposited on massive targets. The success of implantation depends on the knowledge of implant species and basic implant parameters like projected range of implanted ions R_p and the concentration profile usually a Gaussian like function. The purpose of this paper is to determine these parameters after a carefully fitting of experimental data with theoretical predictions for silicon samples implanted with oxygen by using RUMP code [4],[5].

RBS EXPERIMENTS

The RBS experiments were performed using a 2,7MeV α - particle beam delivered by a U-120 cyclotron of the Institute of Nuclear Physics and Engineering - Bucharest. The scattered particles were detected by a surface barrier silicon detector with a total depletion layer of 500 μm and an active area of 150mm^2. The detection angle was 165^0. The beam spot had the dimensions 1mm x 0,2mm. The beam intensity was of the order of 10mA.

---

[1] Faculty of Physics, University of Bucharest.
[2] Institute of Nuclear Physics and Engineering, Bucharest.

The samples used in the present work consisted of the following:

a. A silicon sample implanted with a fluency of 10^{17}O ions cm^{-2} at an energy of 170 key (AR1104)

b. A silicon sample implanted with a fluency of 10^{18}O ions cm^{-2} at an energy of 150 key. The sample was annealed after the implantation (at 1000^{0}C)(AR1105).

RBS SPECTRUM SIMULATION - PHYSICAL CONSIDERATIONS

The application of high energy (MeV) ion beams in thin films analysis has become more and more important in the last few years. Therefore, a serious need has arised for fast-easy-to-use computer programs to evaluate the data.

The backscattering spectra can be analyzed using the computer simulation; this involve a specific target description along the experimental setup parameters. The algorithm alters generally the target composition until the calculated and experimental spectra are fitting together; the fitting procedure could be a least-squares method.

A RBS analysis of a solid sample supposes that the sample is bombarded by ions having certain incident energy (E_0), atomic number (Z_1) and atomic mass (M_1). The projectiles scattered with energy (E) at an angle (θ); The yield of the detected particles between E_i and E_{i+1} is [6,7].

$$Y(E_i) \alpha C_i \Delta x_i \int_{E_{in}(E_i)}^{E_{in}(E_{i+1})} \sigma(E)\, dE \qquad (1)$$

where: $E_{in}(E)$ is the energy of the incident ion before the scattering, C_i and Δx_i are the atomic concentration and the thickness of a slap where the incident energy is $E_{in}(E_{i+1})$ at the front of the slap and $E_{in}(E_i)$ at the back. In case of RBS where the cross section has an analytically form, this spectrum can be calculated easily [8,9].

There are many different elements that should be taken into account for the spectrum simulation. The cross sections are the most important data sets in the simulation process. Also, it is an important factor affecting the sensitivity of a given backscattering measurement, which clearly varies with the mass, charge, and energy at the coming ion. In the standard RBS methods it is assumed that the differential cross section is a Rutherford cross section. This assumption is valid in the range of about 800-2400 key for He and 50-700 key for H.

Another important element of the simulation is the energy loss calculation. This determines the depth scale. The energy of an ion with initial energy (E_0) after penetrating (χ) thickness in the material is:

$$E(x) = E_0 - \int_0^{X_r} \frac{dE}{dx}\, dx \qquad (2)$$

where $X_r = x\sin\alpha$, with α being the angle between the target surface normal and the direction of the incident beam. The sample is divided into slabs so small that (dE/dX) can be considered constant in the slab. The energy after penetrating the ith slab is:

$$E_i = E_{i-1} - \left.\frac{dE}{dx}\right|_{E=E_{i-1}} \frac{\Delta x_i}{\sin\alpha} \tag{3}$$

In the second method, the energy of an ion after penetrating thickness (χ) is given its Taylor expansion [9]:

$$E(x) = E_0 - x\frac{dE}{dx} + \frac{1}{2}x^2\frac{d^2E}{dx^2} + \text{---} \tag{4}$$

Taking the computer's precision into account, this second order approximation is sufficient.

In order to generate a realistic spectrum, the following factors must be take into account:

- The energy fluctuation due to energy straggling of the penetrating ions in the target.
- The energy straggling of the detected particles in the outgoing path and absorbent layer.
- The multiple scattering of incident ions and emitted particles in the target.
- The geometrical spread caused by the finite beam spot size and detector solid angle.
- The angular and lateral spread by particles and the instrumental system resolution.

The energy straggling has been calculated using Bohr's theory and the geometrical straggling. The Bohr's model calculates the straggling in terms of real density of electrons traversed by the beam. The standard deviation (Ω_B) in the beam energy loss in a layer with thickness (t) is [10]:

$$\Omega_B^2 = 4\,\pi\,e\,Z_i^2\sum_i Z_i\,(Nt)_i \tag{5}$$

where Z_i is the atomic number of the ion, e is the electron charge, Z_i and $(Nt)_i$ are the atomic numbers and areal densities of the target atoms. The geometrical straggling as a function of depth can be calculated by assuming that all these straggling as well as the detector resolution are gaussians [11]. Therefore, the square of the standard deviation of the resulting energy straggling (Ω_E) can be computed by adding the square of the individual standard deviations.

RESULTS AND DISCUSSION

The targets are two silicon wafers; they were implanted at two different implant doses. The implant ion was oxygen at energy of 170 and 150keV. One target was implanted at a fluency of 10^{17} ions/cm^2 and the second at 10^{18} ions/cm^2. The second target was after implantation annealed. Figure 1 presents the first target (AR1104) and figure 2 the second one (AR1105) along with the simulated spectra.

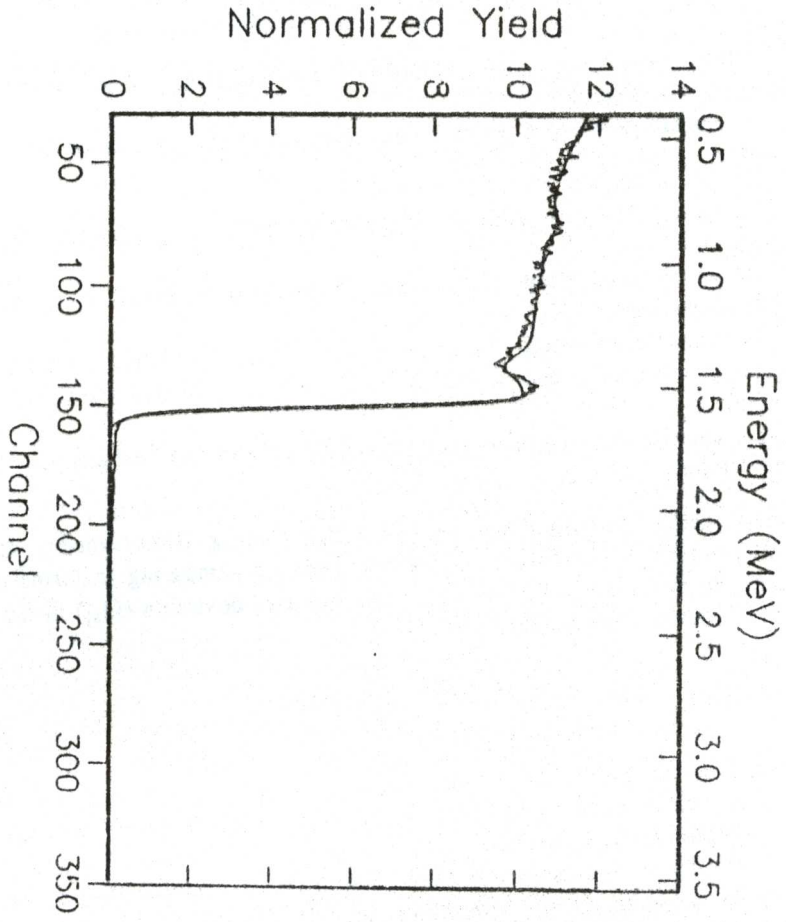

Fig.1. Simulated and measured RBS spectra of silicon sample implanted with a fluence of 10^{17} oxygen in cm^{-2} at an energy of 170 keV.

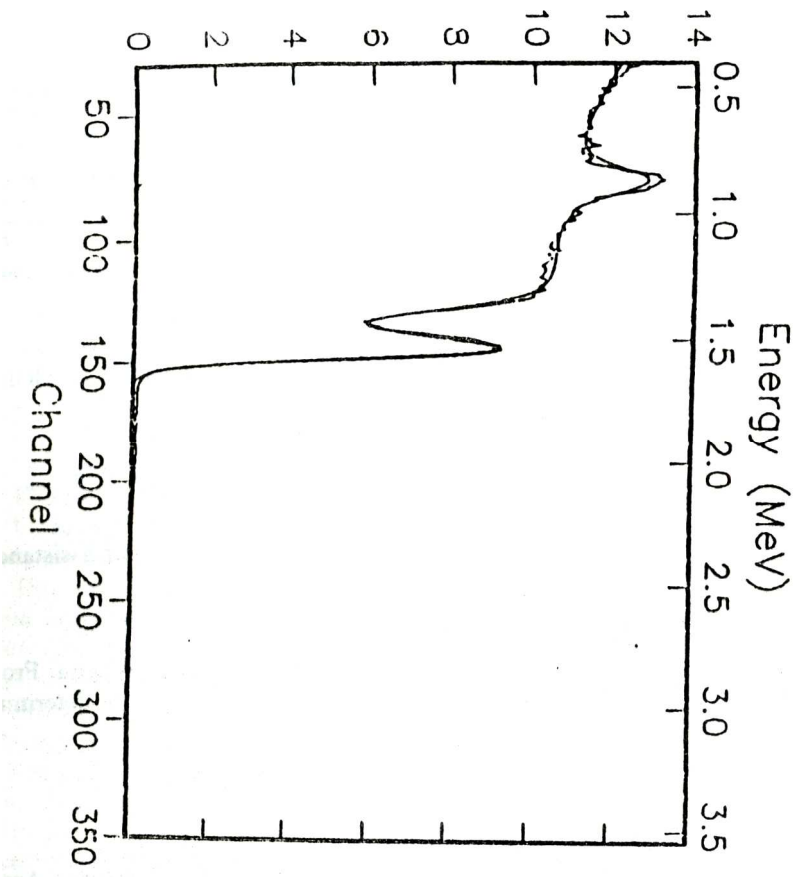

Fig.2 Simulated and measured RBS spectra of silicon sample implanted with a fluency of 10^{18} oxygen in cm^{-2} at an energy of 170 keV.

The RUMP code [9] is used in fitting the experimental data; we compose the target like a bulky silicon target with some diffusant oxygen; one of the RUMP main features is the ability in constructing a composite layer in which the composition of elements can vary along the depth. Practically the layer is subdivided in many layers (maximum 99) every sublayer having its own diffusant concentration. We chose for the implanted oxygen a Gaussian like distribution; for it we gave as starting parameters the amount of implanted oxygen (in relative units), the depth of maximum concentration and the mean width at half height. The second and third parameters are estimated with the help of TRIM code [12]; the TRIM code computes the mean range for projectile ions in amorphous targets for a given incident energy. For a better spectra modeling a supplementary thin layer is placed on the target top; is a dioxide silicon thin layer (few

nanometers), meaning the target handling before and after implant in atmosphere; and the annealing are responsible for the surface oxide.

The main results are summarized in **Table 1**

Table 1.

Target/Obs.	Top $\mathbf{SiO_2}$ layer nm	Oxygen $\mathbf{R_p}$ nm	Oxygen **fwhm** nm	Fluency/energy ions/cm^2/keV
1-nonannaled	3	445	210	10^{17} / 170
2-annealed	6.5	395	354	10^{18} / 150

Remarks:

The implanted oxygen has a Gaussian distribution.

The mean range, $\mathbf{R_p}$, of implanted oxygen fits the prediction of TRIM code for nonannealed targets.

After annealing the thickness of the top SiO_2 is increasing.

After annealing the Oxygen Gaussian distribution becomes wider.

Acknowledgements

The authors gratefully acknowledge dr. E.IVANOV for their assistance and advises to finished this work.

CONCLUSION

Computer simulation is a powerful tool ion beam analysis spectra. From the fit spectrum, the important information of implanted oxygen ions can be determined.

REFERENCES

1. Chu, J.W. Mayer, M.A. Nicolet, *Backscattering spectrometry*.(Academic press, New York, 1978).
2. Saunders, J.F.Ziegler, *Nucl. Instr. and Meth.* 218 (1983) 67.
3. Lawrence R. Doolitle, *Nucl. Instr. and Meth.* B15 (1986) 227.
4. Th.Weber, W.Bolse, K.P. Lieb, *Nucl.Instr. and Meth* B50 (1990) 95.
5. Jahel, et. al, *Nucl. Instr. and Meth.* 182/183 (1981) 223.
6. György Vizkelethy, *Nucl. Instr. and Meth.* B89 (1994) 122.
7. Kötay, *Nucl. Instr. and Meth.* B85 (1994) 588.
8. Blanpain, P. Révész, L.R. Doolitle, K.H. Purser, J.W. Mayer, *Nucl. Instr. and Meth.* B34 (1988) 459.
9. Doolitle, *Nucl. Instr. and Meth.* B9 (1985) 344.
10. Szilágyi and F. Pászti, *Nucl. Instr. and Meth.* B85 (1994) 616. Szilágyi, *Some Problem of Ion Beam Analysis*, Thesis, Eötvös Universty, Budapest (1993).
11. Biersack, L.G. Haggmark, *Nucl. Instr. and Meth.* 174 (1980) 257-269.

STUDIA UNIVERSITATIS BABEŞ-BOLYAI, PHYSICA, XLI, 2, 1996

NMR OSERVATION OF THE SPIN-SPIN RELAXATION IN CIS POLYBUTADIENE -TOLUENE-D_8 SOLUTIONS

M. TODICA[1], **A. V. POP**[1], **L. DAVID**[1], **S. ANGHEL**[1], **G. D. POPESCU**[1], **D. STÃNILÃ**[1]

ABSTRACT. The relaxation of the transversal magnetization of the protons attached to the polymeric chain was analyzed in order to established a correlation between the relaxation time and the characteristic parameters of the viscoelasticity.

INTRODUCTION

Many properties of the polymeric materials are determined by the dynamics of the polymeric chain, [1].

This dynamics can be estimate by observing the evolution of the dipolar interaction between the protons attached to backbone of the chain. The dipolar interaction is the main mechanism which govern the nuclear relaxation of the transversal magnetization, [2].

In the case of one isotropic spin system sumeted to a rapid motion during the NMR observation time, the dipolar interaction is averaged to zero. The relaxation of the transversal magnetization is like in the isotropic liquids. When the dynamics of the polymeric chain is not an isotropic process during the observation time, the dipolar interaction is not averaged to zero and the relaxation function of the transversal magnetization has a specific behavior, [3].

In molten polymers or polymeric solutions, the anisotropy of the chain motion is induced by the temporary junctions between different macromolecules, (the swelling points). The polymeric system can be regarded as a temporary lattice, [4].

Some properties of the polymeric materials, like the viscoelasticity, are directly connected with the existence of this temporary lattice. Because this temporary junctions induces a non zero average of the dipolar interaction, we attempt that a correlation between the NMR parameters of the relaxation of the transversal magnetization and some viscoelastic parameters can be established.

[1] "Babeş-Bolyai" University, Faculty of Physics, 3400 Cluj-Napoca, Romania.

EXPERIMENTAL

We studied the molten cis polybutadiene and the toluene d_8 solution of this polymer, with the polymeric concentrations Φ=88%, Φ=80%, Φ=70%, Φ=60% and Φ=50%. The microstructure of the molten polymer is 97% in cis conformation and 1% in vynil conformation. The glass transition temperature of the molten polymer is T_g=173 K, the molecular mass M_n=110 000g/mol, and the viscoelastic modulus G_n^0=6.9 MPa. The polymeric sample was kindly supplied by the Manufacture Michelin and the deuterated toluene was purchased from Spectrometrie Spin et Techniques, France. The samples were enclosed in NMR tubes (diameter 8mm) and sealed under a primary vacuum. The concentration of the solution was controlled with an accuracy better than 1%.

All the measurements were performed using a CXP Bruker spectrometer working at 45 MHz, in the temperature range of 234 K to, 344 K. The relaxation of the transversal magnetization was observed using the Carr-Purcell sequence, [5]. The sample temperature was controlled within 1 K.

RESULTS AND DISCUSSION

The relaxation of the transversal magnetization is governed by the dipolar interaction between the protons attached to the polymeric chain, but this dynamics is perturbed by the complex dynamics of the entire macromolecule. This dynamics occurs in a large spatial and temporary scale. The elementary motion refers to the monomeric unit and arise in a short time scale. Generally this motion affect the spin-lattice relaxation.

During the specific time of the spin-spin relaxation, the elementary motion can affect many momomers. The motion of the polymeric segment formed by many monomers is an anisotropyc process because the entanglement between two different chains. The entanglements induces an orientational order and thus an anisotropy of the segmental dynamics. For short observation time the polymeric system can be regarded as a rigid lattice. During this time the dipolar interaction between the backbone protons is not averaged to zero and the relaxation function will have a specific behavior. We can consider that the relaxation of the transversal magnetization is directly associated with the existence of the temporary junctions between the polymeric chains.

When the relaxation is governed by one given mechanism the relaxation curves can be described by the same mathematical function. As a result the relaxation curves can be superposed, [6, 7], Fig. 1.

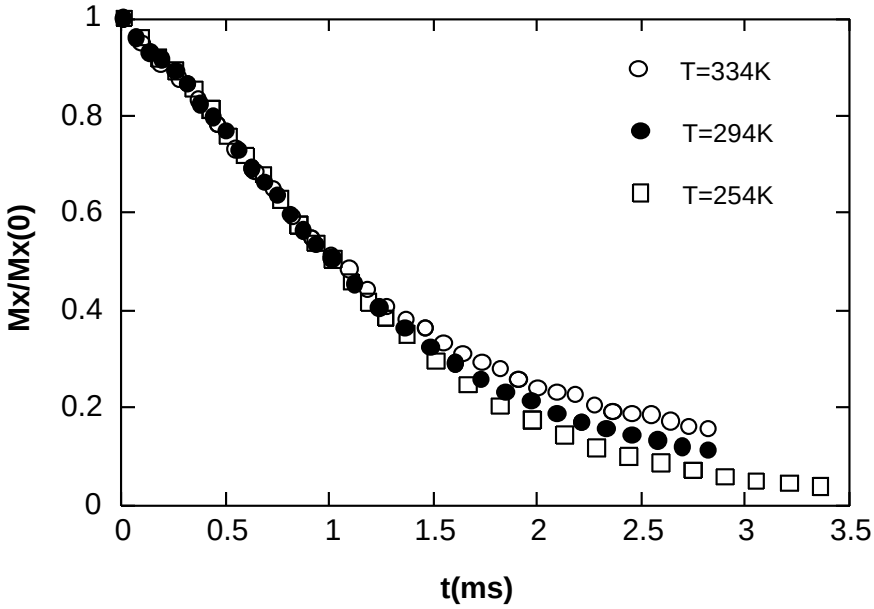

Fig.1. The superposition of the experimental curves observed for the molten polymer. The relaxation curves corresponds to the reference temperature, ( ) Tref = 254 K , (•) T = 294 K and (o)T=334K.

When the NMR observation time is long, the dipolar interaction is affected not only for the segmental dynamics, but also for the dynamics of the entire chain, like the reptation.

For sufficiently long time the polymeric chains became to desingage from the initial swelling points and the macromolecule change their initial conformation. The system can not be depicted like a rigid lattice. The dipolar interaction between the spins is strongly affected by the dynamics of the entire chain. As a result the relaxation function is affected in the terminal region by the long range dynamics. That means that the relaxation mechanism is described by different mathematical functions in the terminal region and at the beginning of the relaxation. The beginning of the relaxation curve is associate with the anisotropy induced by the temporary junctions and the end of the relaxation curve is associated with the dynamics of the entire chain. As a result the relaxation curves do not respect the superposition property in the terminal region, Fig.1.

Our interest will be focused on the superposition domain of the relaxation curves and we try to correlate one NMR parameter with the characteristic properties of the temporary lattice, like the viscoelasticity.

We supposed that the anisotropy of the dipolar interaction is directly connected with the relaxation time of the transversal magnetization. But the relaxation curves do not represent a single exponential function and then it is difficult to define a single relaxation time T_2. For this reason we tried to find another parameter, which will have the same physical signification for all the relaxation curves. We choose the time $t_{0.6}$ measured at 0.6 of the normalized amplitude of each relaxation curve, Fig.2. For this value of the amplitude the relaxation curves obey to the superposition property.

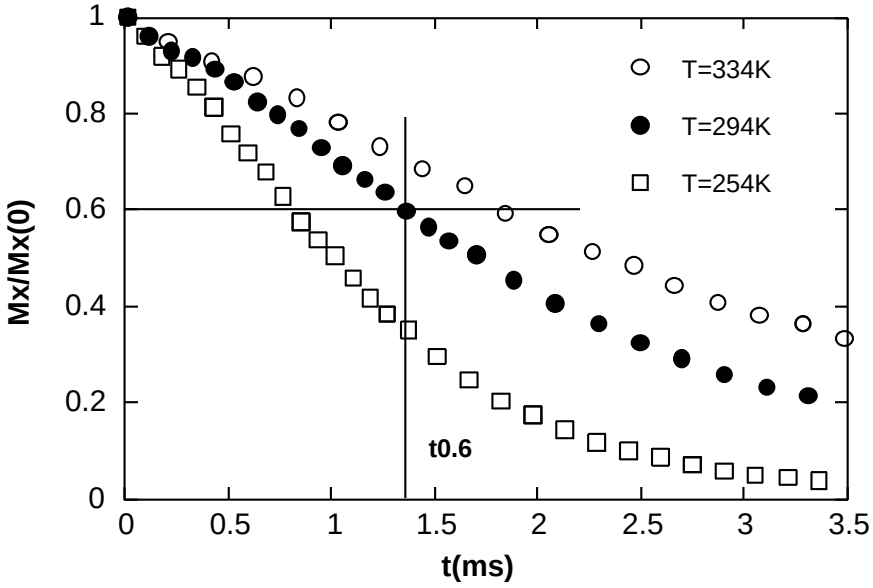

Fig.2. The relaxation of the transversal magnetzation of the molten polymer: ( )T = 254 K , (•) T = 294 K and (o)T=334K.

We measured the parameter $t_{0,6}$ in the temperature range from 254K to 334K for all the samples. We observed a linear dependence of this parameter with the temperature for all our samples, Fig.3. This dependence can be expressed as:

$$t_{0.6}(T,\Phi) = P(\Phi)\left[T - T_i(\Phi)\right] \tag{1}$$

$T_i(\Phi)$ represent the intersection of the linear plot with the axis of the temperatures

$P(\Phi)$ is the slope of the linear plot.

The parameters $T_i(\Phi)$ and $P(\Phi)$ can be evaluated experimentally.

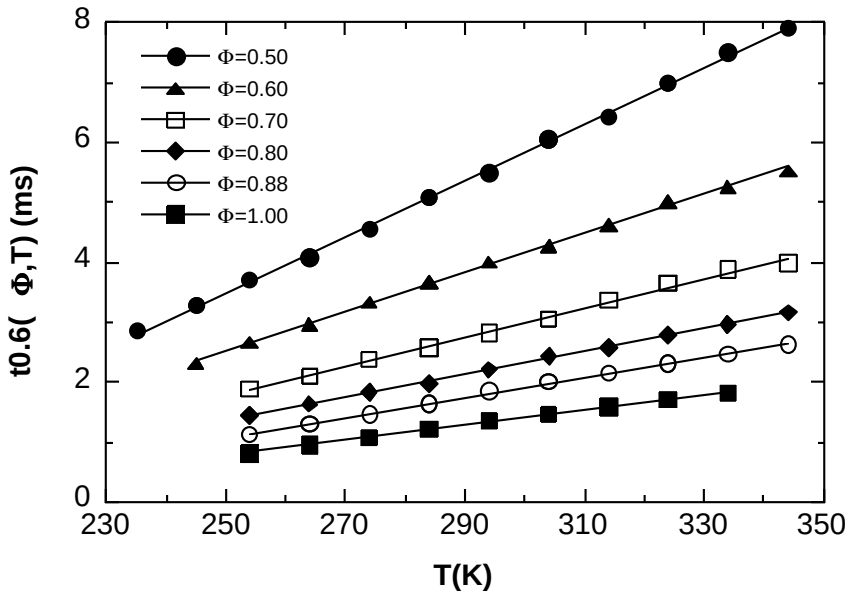

Fig.3. Temperature dependence of the parameter $t_{0.6}$ for different cis-polybutadiene-toluene D_8 solutions. Φ is the polymeric concentration.

Our interest is focused upon the parameter $P(\Phi)$ which depends on the concentration of the solutions, but do not depend on the temperature. We observed a linear dependence of this parameter when a new variable $\Phi^{-2.2}$ is used, Fig.4. This dependence can be expressed as:

$$P(\Phi)=A\left[1+\frac{b}{\Phi^{2.2}}\right] \tag{2}$$

where A and b are the fit parameters.

From mechanical studies it is known that the concentration dependence of the modulus of elasticity $G_N^0(\Phi)$ of the polymeric solutions is described by the relation:

$$G_N^0(\Phi) = G_N^0\Phi^c \tag{3}$$

where G_N^0 is the modulus of the molten polymer and **c** is one exponent with the value from 2 to 2.3, [8].

If we take $b=B/G_N^0$ in equation (2) we obtain:

$$P(\Phi) = A\left[1+\frac{B}{G_N^0\Phi^{2.2}}\right] \tag{4}$$

In equation (4) we can separate the expression of the modulus $G_N^0(\Phi)$ of the solutions, if we take the value 2.2 for the exponent *c*. The constants A and B has the values $A=3.84\ 10^{-3}\ m^2/K$ and B=16.8 MPa for ours samples.

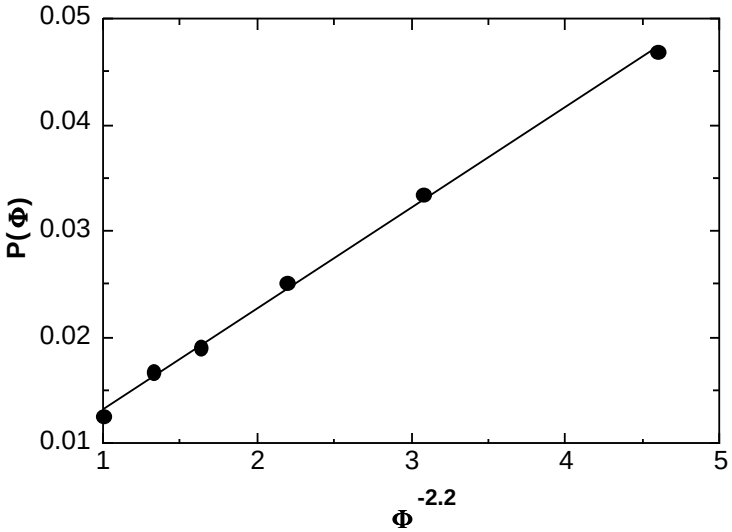

Fig. 4. Linear plot of the parameter P(Φ) versus the variable $\Phi^{-2.2}$ for some cis-polybutadiene-toluene D_8 solutions, with different polymeric concentrations.

From relations (1) and (5) we obtain:

$$t_{0.6}(T,\Phi) = A\left(T - T_i(\Phi)\right)\left[1+\frac{B}{G_N^0\Phi^{2.2}}\right] \tag{5}$$

The empirical equation (6) expressed the relation between the NMR parameter $t_{0.6}$ and the modulus of the solutions. This equation test that the specific NMR parameters, like the relaxation time of the transversal magnetization, can be connected with the parameters of the viscoelastic property of the polymeric solutions.

CONCLUSION

The analyze of the relaxation time of the transversal magnetization is an important way to observe the existence of the temporary lattice in the polymeric solutions. This temporary lattice is induced by the temporary junctions between different polymeric chains. It is possible to established a correlation between the NMR parameters of the relaxation and the viscoelastic behavior of the polymeric system. This dependence is described by the empirical equation (5).

REFERENCES

1. P.G.de Gennes, *Scaling Concepts* in Polymeric Physics, Cornell University Press, Ithaca, New-York, 1979.
2. A.Abragam, *Principles of Nuclear Magnetism*, Oxford University Press, London, 1961.
3. J.P. Cohen-Addad, *NMR and Fractal Properties of Polymers Liquids and Gels*, Pergamon Press, London, 1992.
4. A. Labouriau, J. P. Cohen-Addad, *J. Chem. Phys*., 94, 3249, 1991.
5. H.Y. Carr, E. R. Purcell, *Phyd. Rev*., 94, 630, 1954.
6. J.P. Cohen-Addad, A. Labouriau, *J. Chem. Phys*., 93, 4,15, 1990.
7. J.P. Cohen-Addad, *Physical Properties of Polymeric Gels, John Wiley and Sons*, Chichester, New-York, Toronto, 1996.
8. W.W. Graessley, *Adv. Polym. Sci*.,16, 1, 1974.
9. W.W. Graessley, S. F. Edwards, *Polymer*, 22, 1329, 1981.

STUDIA UNIVERSITATIS BABEŞ-BOLYAI, PHYSICA, XLI, 2 1996

PROTON SPIN - LATTICE RELAXATION IN SOME POLYISOPRENE SOLUTIONS

M. TODICĂ[1], S. ANGHEL[1], V. SIMON[1]

ABSTRACT. Spin-lattice relaxation time T_1 of the protons attached to the polymeric chain was measured in some solutions of the polyisoprene and C_7D_8, CCl_4 and $CDCl_3$ solvents. The temperature dependence of the time T_1 was analyzed over a wide range of the temperature above the glass transition temperature. The maximum of the spin-lattice relaxation rate is observed for all the samples. The temperature dependence of the spin-lattice relaxation time is connected with the local dynamics of the polymeric chain. The correlation time τ_C of the local motions corresponding to the maximum relaxation rate is $\tau_C = 2.2\ 10^{-8}$s.

The experimental curves $T_1(T)$ obtained for the polyisoprene-C_7D_8 polyisoprene-CCl_4 and polyisoprene-$CDCl_3$, solutions obey to the superposition property. The relaxation process is governed by the same mechanism in all this solutions.

INTRODUCTION

The relaxation of the longitudinal magnetization of the protons attached to the polymeric chain is a reach source of information about the local dynamics of the skeletal bonds of the chain, [1, 2]. The main mechanism which govern this relaxation is the dipolar interaction between the protons of the segmental units which include a few polymeric links.

The presence of the solvent molecules in the vicinity of the polymeric segments, or thermal activation, affect the local dynamics of the chain and thus the dipolar interaction between the neighboring protons. As a result the spin-lattice relaxation rate will depends on the temperature and solvent concentration.

In this study we are interested to observe this dependence for some solutions of the polyisoprene.

[1] Faculty of Physics, Babeş-Bolyai University, 3400 Cluj-Napoca, Romania.

EXPERIMENTAL

We studied some polyisoprene-toluene D_8 solutions with the polymeric concentration Φ=94%, Φ=78% and Φ=59%, polyisoprene-CCl_4 solutions with the polymeric concentration Φ=77% and Φ=59%, and polyisoprene-$CDCl_3$ with the polymeric concentration Φ=85% and Φ=62%, in the temperature range of 234K to 350K. The isomeric conformation of the polyisoprene sample was 92% cis-1,4, the glass transition temperature Tg=201±4K and the thermal expansion coefficient $\alpha=6.7\ 10^{-4}\ K^{-1}$. The glass transition temperature of the toluene is Tg=113±4K and the thermal expansion coefficient $\alpha=1.7\ 10^{-3}\ K^{-1}$. The samples were enclosed in NMR tubes and sealed under a primary vacuum. Spin-lattice relaxation time of the protons was measured using the inversion-recovery sequence (π-τ-$\pi/2$), [3]. All the measurements were performed at 45 MHz, using a CXP Bruker spectrometer.

RESULTS AND DISCUSSION

The dominant mechanism which govern the spin-lattice relaxation of the protons attached to the polymeric chain is the dipolar interaction with the nuclear spins located within one given chain segment, [4]. For a complex spin system, with protons located on different positions, the spin-lattice relaxation rate is expressed by a mathematically function which include the interaction with all the nuclear spins, [5]. When the protons are located in equivalent positions or the interaction between the far spins is neglected, the spin-lattice relaxation is described by a single relaxation time T_1. The relaxation time is temperature dependent and reach its minimum when the Larmor frequency ω_o is equal to the frequency of the local reorientation of the polymeric segments. In this case $\omega_o\tau_c\cong1$, [6]. This is a simple way to calculate the correlation time τ_c of the local reorientation of the polymeric segment.

The temperature dependence of the T_1 for the molten polymer and for the polyisoprene-toluene solutions was analyzed in previous works, [7]. For each sample the minimum value of the relaxation time T_1 is observed for a specific temperature $\theta(\Phi)$ depending on the polymer concentration, but the minimum value of the T_1 is the same as for the molten polymer in all the cases, $T_{1min}(\theta)$=50±5ms. The correlation time corresponding to those temperatures is $\tau_c\cong2.2\ 10^{-8}$ s for all the samples. We observed the relation $\theta(\Phi)$-$T_g(\Phi)$=107±10K, were $T_g(\Phi)$ is the glass transition temperature of the solutions calculated with the expression, [8]:

$$T_g(\Phi)=\frac{\alpha_p T_g^p(\Phi)+\alpha_s T_g^s(1-\Phi)}{\alpha_p\Phi+\alpha_s(1-\Phi)}$$

For this system the experimental curves $T_1(T)$ can be superposed if we plot the relaxation time T_1 versus the new variable $T^*=T-T_g(\Phi)=T-\theta(\Phi)+(107\pm10K)$. This superposition property shows that the temperature dependence of the relaxation time

T_1 can be described by the same mathematically expression, depending on the new variable T*, for the molten polymer and for the concentrated solutions. But the relaxation process is affected by the local dynamics of the polymeric links, which depends on the temperature and solvent concentration. When the superposition condition is fulfilled then the presence of the toluene molecules in the vicinity of the polymeric chain do not modify dramatically the local dynamics of the skeletal bonds and thus the relaxation process is like in the case of the molten polymer.

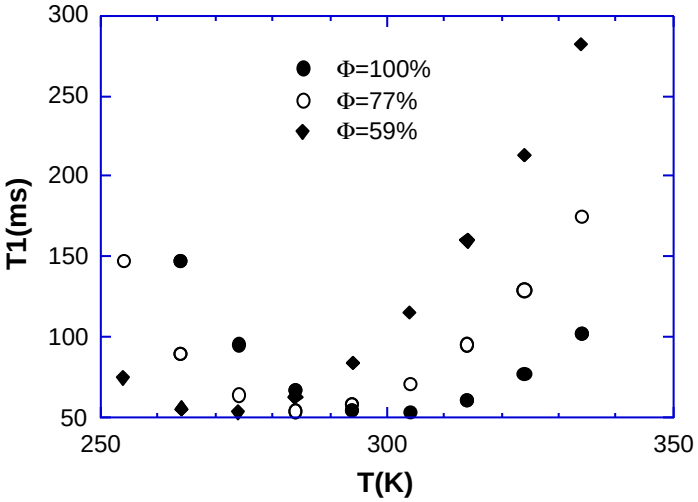

Fig. 1.. Temperature dependence of the relaxation time T_1 of the molten polyisoprene and polyisoprene-CCl_4 solutions.

It should be interesting to observe the behavior of this polymer when the toluene is replaced by another solvent, like the CCl_4 or $CDCl_3$. The temperature dependence of the relaxation time T_1 of the polyisoprene-CCl_4 solutions is shown in Fig.1. The minimum value of the relaxation time T_1 is the same for all the samples $T_{1min}(\theta)$=50±5ms, like for the molten polymer. This minimum correspond to one characteristic temperature $\theta(\Phi)$ for each concentration. The correlation time t_c corresponding to those temperatures is $\tau_c \cong 2.2\ 10^{-8}$ s. For a given concentration of the polymer, the temperature $\theta(\Phi)$ corresponding to the polyisoprene-CCl_4 solutions is higher that the temperature $\theta(\Phi)$ corresponding to the polyisoprene-C_7D_8 solutions. Then the mobility of the polymeric chain, corresponding to a given temperature T, is greater in the polyisoprene-C_7D_8 solutions like in the polyisoprene-CCl_4 solutions.

The curves $T_1(T)$ of the molten polymer and the solutions can be superposedwhen we utilize the variable $T^*=T-\theta(\Phi)+(107\pm10K)$, Fig. 2.

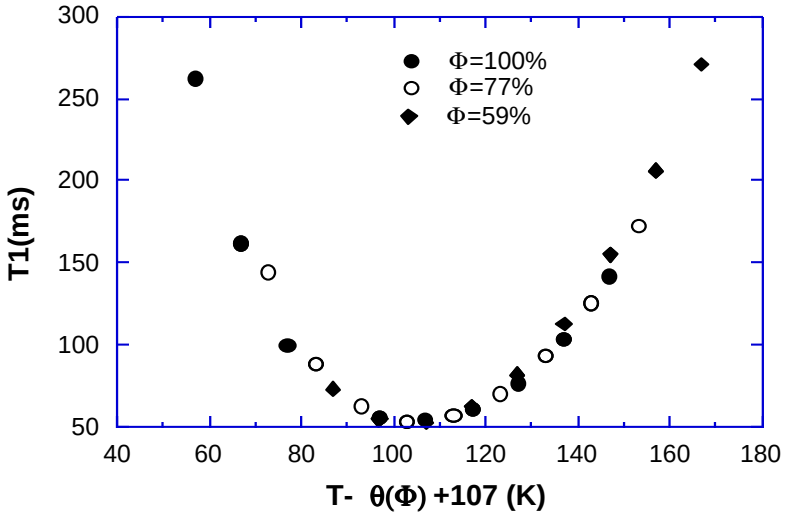

Fig. 2. Superposition of the curves $T_1(T^*)$ of the molten polyisoprene and polyisoprene-CCl_4 solutions.

If we combine both the superposition properties, polyisoprene-C_7D_8 and polyisoprene-CCl_4, we can affirm that the temperature dependence of the relaxation time T_1 is described by the same mathematically expression depending on the new variable T*. In this case we have the same dynamically properties of the polymeric chain when the C_7D_8 or CCl_4 solvents are utilized. The CCl_4 molecules play the same role in the dynamics of the polyisoprene like the toluene molecules.The temperature dependence of the relaxation time T_1 of the polyisoprene-$CDCl_3$ solutions is shown in Fig. 3. We found the same minimum value of the relaxation time T_1 like for the molten polymer $T_{1min}(\Phi)$=50±5ms, for all the samples. This minimum correspond to one characteristic temperature $\theta(\Phi)$ for each concentration. The temperatures $\theta(\Phi)$ corresponding to the minimum of T_1, for all the solvents, are represented in Fig. 4. The temperatures $\theta(\Phi)$ decreases when the solvent concentration increase. This representation suggest the fact that the temperatures $\theta(\Phi)$ has the same concentration dependence like the glass transition temperatures of the solutions. On the other hand this behavior can indicate a simple superposition property of the curves $T_1(T)$ by translation along the temperature axe. In fact we can superpose the curves $T_1(T)$ of the solutions and $T_1(T)$ of the molten polymer when we utilize the variable $T^*=T-\theta(\Phi)+(107\pm10K)$, Fig. 5.

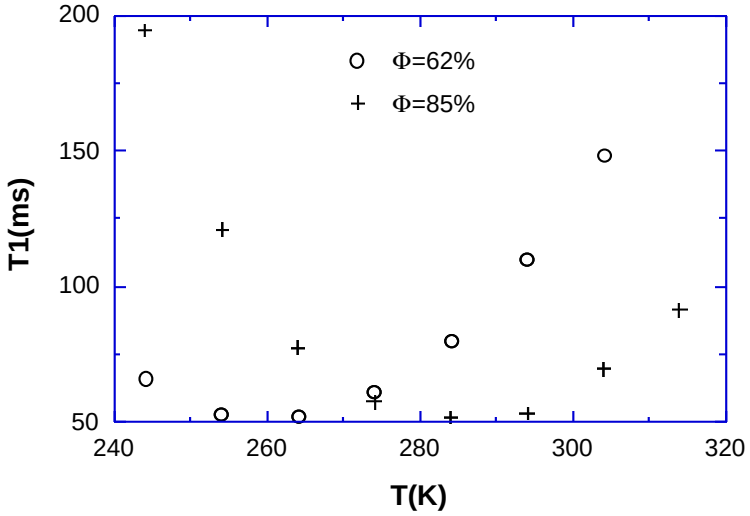

Fig. 3. Temperature dependence of the relaxation time T_1 of the molten polyisoprene and polyisoprene-$CDCl_3$ solutions.

The $CDCl_3$ molecules are different from the CCl_4 molecules by the presence of one deuterium atom which replace one Cl atom. This situation determine a slightly difference on the spatial symmetry of this molecules. However the superposition property of $T_1(T^*)$ indicate the fact that this difference do of this solvents are used. In this case the dynamic process of the skeletal links is the same in both the solvents. If we compare the resultat of the superposition of $T_1(T)$ for all the samples we can conclude that the spin-lattice relaxation process is governed by the same mechanism when the C_7D_8, CCl_4 or$CDCl_3$ solvents are utilized. One similar behavior of this polymer in different solvents was observed for other authors, [9,10]. Then the local dynamics of polymeric chain is governed by the same mechanism in all this solvents.

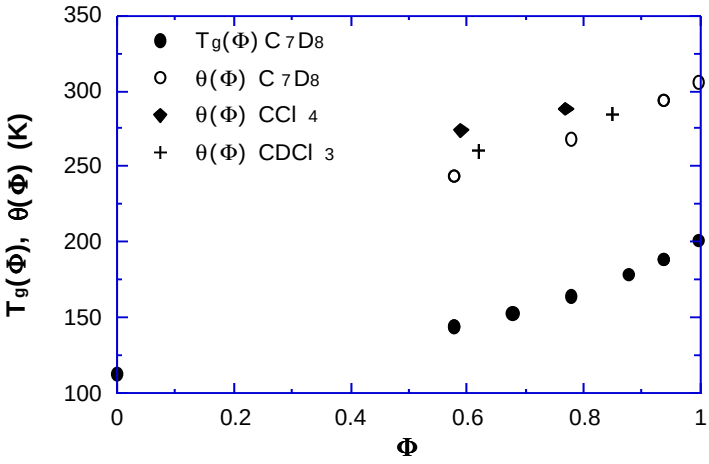

Fig. 4. Concentration dependence of the glass transition temperature of the polyisoprene-C_7D_8 solutions and concentration dependence of the temperatures θ(Φ) of the polyisoprene in different solvents.

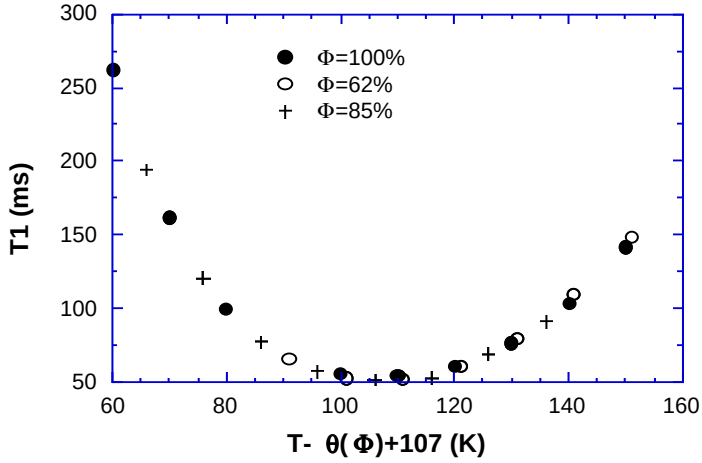

Fig. 5. Superposition of the curves $T_1(T^*)$ of the molten polyisoprene and polyisoprene-$CDCl_3$ solutions.

CONCLUSION

The superposition property of the relaxation curves $T_1(\Phi,T)$ suggest the fact that the relaxation process can be expressed by a single mathematically function. This property is also respected if the toluene is replaced by the CCl_4 or $CDCl_3$ molecules in the polyisoprene solutions. The local dynamics of the polymeric segments is governed by the same mechanism for the polyisoprene C_7D_8, polyisoprene CCl_4 and polyisoprene $CDCl_3$ concentrated solution. The correlation time of the local reorientation of the polymeric bonds can by calculated when the curves $T_1(\Phi,T)$ reach its minimum and has the value for this systems $t_c \cong 2.2\ 10^{-8}$ s.

REFERENCES

1. Cohen-Addad, "*NMR and Fractal Properties of Polymers Liquids and Gels*", Pergamon Press, London, 1992.
2. Cohen-Addad, "*Physical Properties of Polymeric Gels*", John Wiley and Sons, Chichester, New-York, Toronto, 1996.
3. Carr, E. R. Purcell, *Phys. Rev*., 94, 630, 1954.
4. Abragam, "*Principles of Nuclear Magnetism*", Oxford University Press, London, 1961.
5. Guillermo, R. Dupeyre, J. P. Cohen-Addad, *Macromolecules*, 23, 1291, 1990.
6. Ya. Slonim, A. N. Lyubimov, "*The NMR of Polymers*", Plenum Press, New York, 1970.
7. Todica, G. Damian, D. Ciurchea and A. V. Pop, *Studia, Physic*a Univ. "Babes-Bolyai", XL, 1, 1995.
8. Ferry, "*Viscoelstic Properties of Polymers*", John Wiley and Sons, New York, 1980.
9. Glowinkowski, D. J. Gisser, M. D. Ediger, *Macromolecules*, 23, 3520, 1990.
10. Gisser, S. Gloinkovski, M. D. Ediger, *Macromolecules*, 4, 270, 1991.

STUDIA UNIVERSITATIS BABEŞ-BOLYAI, PHYSICA, XLI, 2, 1996

SPECTROSCOPIC AND MAGNETIC INVESTIGATION OF SOME CU(II)-NITRAZEPAM COMPLEXES

L. DAVID[1], O. COZAR[2], E. FORIZS[2], R. TETEAN[1]
C. CRACIUN[1], D. OPRISOR[1]

ABSTRACT. The CuL_2X_2 (L=7-nitro-1,3 dihydro-5-phenyl-2H-1,4 benzodiazepin-2-one, also known as nitrazepam or mogadon, X=Cl,Br) complexes were prepared and investigated by IR, ESR and magnetic susceptibility measurements. The IR spectra suggest that Cu(II) ion is coordinated by two nitrogen and two halogen atoms. The powder ESR spectrum at room temperature of CuL_2Br_2 is quasiisotropic, while for CuL_2Cl_2 is characteristic for axial monomeric species with small rhombic distortion. The isotropic ESR spectra of these compounds in DMF and Py solutions suggest the presence of pseudo-tetrahedral monomeric species. Two different monomeric species were evidenced in Cu(II)-Nitrazepam solutions adsorbed on NaY zeolite.

INTRODUCTION.

Derivatives of 1,4-benzodiazepine are used in medicine as tranquilizing and sedative-hypnotic agents [1-5]. 1,4-benzodiazepine can adopt monodentate, bidentate or bridging ligand bonding mode. The stereochemistry and chemical reactivity studies of their coordination compounds with transition metal ions help us to determine the relationship between chemical structure and biological activity of these drugs. It is well known that the metal complexes of ligands which have biological activity are more active than the free ligands [2,3]. There have been studied the peoperties of 1,4-benzodiazepines with the palladinum (II) and platinum (II) metals for theirs considerable antibacterial power [2]. Nitrazepam (7-nitro-1,3dihydro-5-phenyl-2H-1,4 benzodiaze- pin-2-one) (Fig.1) is one of these benzodiazepine which is a commercially available drug with myorelaxant and anxyolitic activity.

[1] "Babeş-Bolyai" Univ., Depart. of Phys., Cluj-Napoca, Romania.
[2] "Babeş-Bolyai" Univ., Depart. of Chem., Cluj-Napoca, Romania.

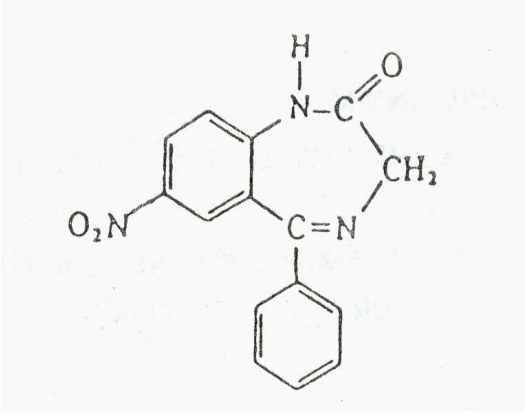

Fig. 1. The Nitrazepam structural formulae

We report here the synthesis and spectroscopic characterization of two complexes of copper(II) halides with Nitrazepam. The choice of the Cu(II) metal is a result of his large implications in pharmacology [6].

EXPERIMENTAL.

The ligand, nitrazepam, supplied by Terapia of Cluj-Napoca has been used without further purification. The complexes was obtained by adding a solution of nitrazepam (0.5 g, 1.9 mmol) in acetone to the solution of appropriate metal salts ($CuCl_2 \times 2H_2O$; $CuBr_2$ 0.8 mmol) in an equal volume of the same solvent. The solutions was vigorously stirred for about 30 min. at room temperature and the insoluble precipitates were filtered off. The complexes were purified by means of repeated washing with acetone.

Infrared spectra have been recorded in the 4000-400 cm^{-1} range with a Bio-Rad-Digilab-FTS 65A/896 spectrometer by the KBr pellets technique. Far-IR spectra in the range 500-100 cm^{-1} were recorded on a Bio-Rad FTS-40V using polyethylene pellets. The magnetic susceptibility measurements were performed in the temperature range 77-300 K with a Faraday balance. ESR spectra were obtained in the X band (9,4GHz) using a standard JEOL-JES-3B equipment at room temperature.

RESULTS AND DISCUSSION

All the typical bands of the ligand appear in the IR spectra of the metal complexes. The most important IR bands and theirs assignments are listed in Table 1. One of the changes observed in the IR spectra of the both complexes is the negative shift (18-19 cm^{-1}) of the n(N-H) vibration band which appears in the 3195 cm^{-1} region. Positive shifts (22 cm^{-1} and 3 cm^{-1}) appear for the n(C=O) and n(C=N) vibration modes respectively.

Compound	**ν(NH)**	**ν(C=O)**	**ν(C=N)**	**ν(Cu-N)**	**ν(Cu-X)**
Nitrazepam (L)	3214	1695	1611	-	-
CuL_2Cl_2	3195	1718	1615	302	285
CuL_2Br_2	3196	1717	1614	302	287

Table 1. IR spectroscopic data (cm^{-1}) of the ligand and Cu(II)-complexes

The spectra of complexes present the band characteristic of the symmetric and antisymmetric stretching modes of the nitro-group at the same value (1529 and 1350 cm^{-1}) as in the free ligand [7].

In the Far-IR spectra of the complexes a new band assignable to the ν(Cu-N) vibration appears at 331 cm^{-1} and 346 cm^{-1} which confirms the involvement of nitrogen atoms in the coordination [8]. The bands assigned to the ν(Cu-X) vibration (X=Cl, Br) appears at 302 cm^{-1} and 246 cm^{-1}.

The amide and imino bands are found to be unaffected by complexation and thus rules out the coordination through keto-oxygen or through the 4-nitrogen. Also, no bands are present in the range where ν(Cu-O) usually lies for this metal. The fact that the spectrum of the Cu(II)-nitrazepam compound shows a noticeable difference in the position of ν(C=O) stretching frequency given by the same band of the free ligand may be explained through the possible hydrogen bonds owing to the water of crystallization. The presence of this water of crystallization is confirmed by the medium-strong absorption bands observed in the ranges 3480-3450 cm^{-1} for ν(O-H) frequency and 1640-1625 cm^{-1} frequency. Since vibrational modes such as wagging, twisting and rocking activated by the coordination to the metal have not been found in the expected ranges, it appears that coordinated water (at the metallic ion) is not present.

These results suggest that only the N(1) atom of the nitrazepam and the halogen atom (Cl or Br) are involved in the coordination process. The nature of the halogen atom

The results for the atomic magnetic moments 1.78 μ_B (CuL_2Cl_2) and 1.72 μ_B (CuL_2Br_2) obtained from the magnetic susceptibility measurements are in good agreement with theoretical values corresponding to the $3d^9$ systems [9]. The effective magnetic moments suggest a distorted tetrahedral local environment around Cu^{2+} ions [10]. Fig.2 presents the magnetic data for the CuL_2Cl_2 compound. The linear dependence of χ^{-1} vs T show a Curie-Weiss behavior with θ=55 K. The positive value of θ suggests the possibility of the ferromagnetic interactions between metallic ions, through the hydrogen bounds.

The powder ESR spectrum of CuL_2Cl_2 complex obtained at room temperature (Fig.3) exhibit the absorption signals typical of randomly oriented single state (S=1/2) species having an axial symmetry with a small rhombic distortion (g_1=2.208, g_2=2.059, g_3=2.025). The powder ESR spectrum of CuL_2Br_2 is quasiisotropic (g=2.090).

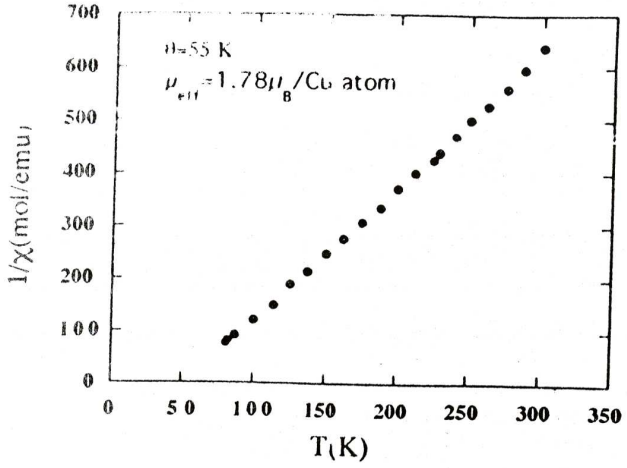

Fig. 2. Temperature dependence of χ^{-1} for CuL_2Cl_2 complex

The monomeric species prevail also in the pyridine (Py) and dimethylformamide (DMF) solutions of Cu(II)-Nitrazepam compounds. The shape of the spectra (Fig.4) and the obtained values of ESR parameters for these solutions (Table 2) suggest the presence of Cu(II) pseudotetrahedral species [11]. No hyperfine splitting due to the interaction of the paramagnetic electron with nitrogen or halogen nuclei was observed.

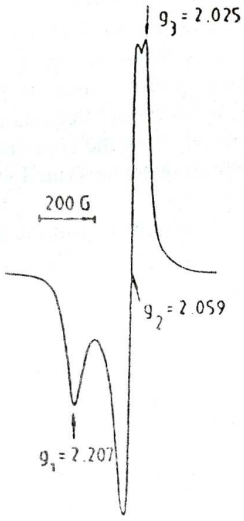

Fig. 3. Powder ESR spectrum of CuL_2Cl_2 complex at room temperature

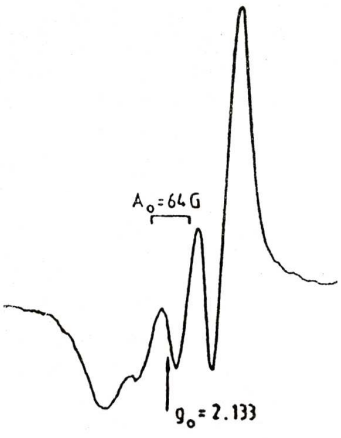

Fig.4. ESR spectrum of Py CuL_2Cl_2 solution at room temperature

Table 2. ESR parameters of DMF and Py CuL_2X_2 solutions

Compound	Solvent	g_0	A_0(G)
CuL_2Cl_2	DMF	2.171	55
CuL_2Cl_2	Py	2.133	64
CuL_2Br_2	DMF	2.174	59
CuL_2Br_2	Py	2.141	69

The anisotropic spectra with four hyperfine lines in the g_{II} region and a strong absorption signal in the $g_{\perp}$ region were obtained from Cu(II)-Nitrazepam solutions adsorbed on NaY zeolite. The spectra of a DMF CuL_2X_2 solutions show the coexistence of two monomeric species with different values for g_{II} and A_{II} parameters (Fig.5) with different values for g_{II} and A_{II} parameters. One of these species with CuN_2O_2 chromophore is due to the coordination of solvent molecules at the Cu(II) ion in halogen atom's stead. The other set of parameters confirms the existence of a CuO_4 chromophore with planar-distorted tetrahedral (T_d) symmetry [12].

Table 3. ESR parameters of mononuclear species obtained in Cu(II)-Nitrazepam solutions adsorbed on NaY zeolite, at room temperature.

Compound	Solvent	g_{II}	$g_{\perp}$	A_{II}(G)	Chromophore and symmetry
CuL_2Cl_2	DMF	2.393 2.353	2.081	122 170	$CuO_4 \rightarrow T_d$ $CuN_2O_2 \rightarrow D_{2d}$
CuL_2Cl_2	Py	2.282 2.249	2.059	163 178	$CuN_2N_4^* \rightarrow O_h$ $CuN_4 \rightarrow D_{4h}$
CuL_2Br_2	DMF	2.383 2.351	2.082	125 170	$CuO_4 \rightarrow T_d$ $CuN_2O_2 \rightarrow D_{2d}$
CuL_2Br_2	Py	2.297 2.251	2.062	169 174	$CuN_2N_4^* \rightarrow O_h$ $CuN_4 \rightarrow D_{4h}$

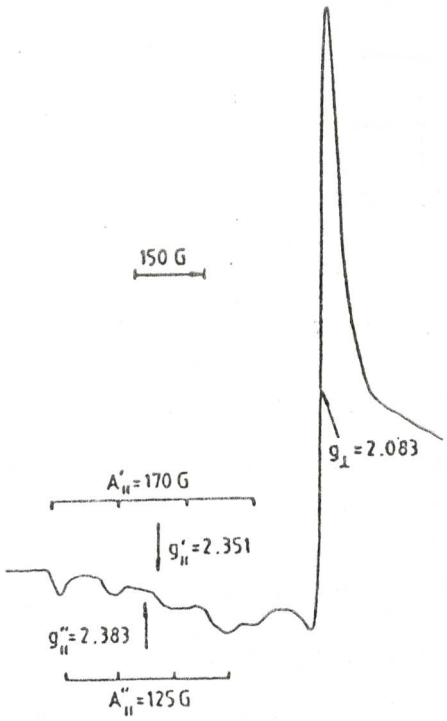

Fig.5. ESR spectrum of DMF CuL_2Br_2 solution adsorbed on NaY zeolite

ESR data concerning the Cu(II) ion in the tetrahedral symmetry are characterized by the decreasing of hyperfine structure constants and the increasing of g_{II} values relatively to those usually observed in square-planar or octahedral-distorted environments. This can be explained by the 4p-admixture in the d_{xy} ground state of planar-tetrahedral distorted species [13]. Electronic spectra of CuL_2X_2 compounds in DMF solutions show an absorption band at 13400 cm^{-1} which may be attributed to the $d_{xy} \rightarrow d_{x^2-y^2}$ transition [2]. Considering $\Delta_{x^2-y^2}$=13400 cm^{-1} and β^2=1 a value of 0,79 respectively 0.77 was estimated for the α^2 coefficient for the both compounds CuL_2Cl_2 and CuL_2Br_2. Using the LCAO-MO procedure [13] a ontribution of 2% of $4p_z$ orbital to the ground state has been obtained for the studied complexes.

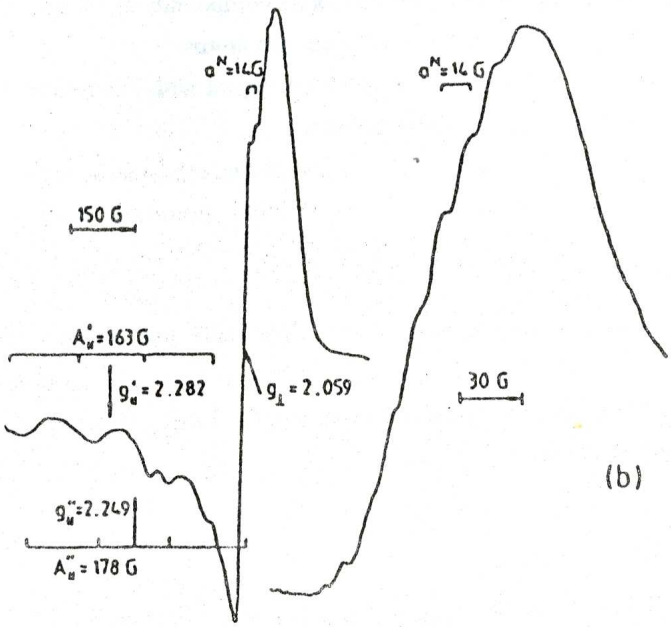

Fig.6. ESR spectrum of pyridine CuL_2Cl_2 solution adsorbed on NaY zeolite (a). Extended perpendicular absorbtion (b)

ESR spectra of pyridine Cu(II)-Nitrazepam solutions adsorbed on NaY zeolite also suggest the presence of two magnetically nonequivalent monomeric species (Fig.6). One of these species having $CuN_2N_2^*$ chromophore is due to the substitution of halogen atoms by pyridine molecules. The analyses of ESR parameters characteristic for these monomeric species suggest a hexacoordinated octahedral distorted geometry around Cu^{2+} ions due to the possible coordination of another two pyridine molecules along the Oz axis. The O_h local symmetry results from the great value of g_{II} parameter and relative small value of A_{II}, comparative with the case of square-planar symmetry. The second monomeric species of CuN_4 chromophore occurs by total substitution of halogen atoms and nitrazepam molecules by pyridine molecules. The existence of CuN_4 chromophore is also confirmed by the appearance of nine nitrogen superhyperfine lines in the $g_{\perp}$ region (a^N=14 G).

CONCLUSIONS

IR spectra of nitrazepam and its Cu(II) compounds show that Cu(II) ion is four coordinated by two nitrogen atoms and two halogen atoms.

The magnetic moments are in good agreement with theoretical estimations to the $3d^9$ systems with a tetrahedral distorted geometry.

The powder ESR spectra of Cu(II) complexes are quasiisotropic for CuL_2Br_2 and anisotropic for CuL_2Cl_2 suggesting an axial local symmetry with a small rhombic distortion.

The anisotropic ESR spectra obtained for DMF and pyridine CuL_2X_2 solutions adsorbed on NaY zeolite show the presence of two magnetic nonequivalent monomeric species. The kinds of these monomeric species and the local symmetry around Cu(II) ions depend on the solvent nature.

REFERENCES

1. C. Preti, G. Tosi, *J. Coord. Chem.* 6,81 (1976).
2. C. Preti, G. Tosi, *J. Coord. Chem.* 8,223 (1979).
3. C. Preti, G. Tosi, *Transition Met. Chem.* 3,246 (1978).
4. G. Minghetti, M. L. Ganadu, C. Foddai, M. A. Cinellu, F. Demartin, M. Manassero, *Inorg. Chim. Acta*, 86,93 (1984).
5. M.A. Cinellu, M. L. Ganadu, G. Minghetti, F. Cariati, F. Demartin, M. Manassero, *Inorg. Chim. Acta* 143,197 (1984).
6. Srenson J. R. J. in*: Metal Ions in Biological Systems* (Siegel H., ed), Vol 14, Marcel Dekker, New York, 1982, p.77-124.
7. K. Nakamoto, *Infrared and Raman Spectra of Inorganic and Coordination Compound*, J. Wiley ed., New York, 1969.
8. N.B. Colthup, L.H. Delly, S.E. Wiberley, *Introduction to Infrared and Raman Spectroscopy*, Academic Press, New York, 1964.

9. I.Drago, S. Russel, *Physical Methods in Chemistry*, W.B. Saunders Company, 1977.
10. B.J.Hathaway, *Comprehensive Coordination Chemistry*, Geoffrey Wilkinson ed., Vol. 5, Pergamon Press, Oxford, 1987.
11. H.Yokoi, A.W. Addison, *Inorg. Chem*. 16,1341 (1977).
12. M.Mahajan, K.N. Saxena, *J. Inorganic & Nuclear Chemistry* 43,2148 (1981).
13. O.Cozar, I. Ardelean, *J. Non-Crystalline Solid*s 92,278 (1987).

STUDIA UNIVERSITATIS BABEŞ-BOLYAI, PHYSICA, XLI, 2, 1996

CAPACITIVELY COUPLED PLASMA AS SPECTRAL SOURCE FOR DIRECT ANALYSIS OF CONDUCTIVE SAMPLES

S. D. ANGHEL[1], **M. TODICA**[1]

ABSTRACT. A spectral source based on a RF capacitively coupled plasma at atmospheric pressure is presented. This discharge is in contact with only one electrode that is the sample too. The plasma support gas is Ar, with a flow-rate of 0.6 - 1.6 l/min. The frequency of electromagnetic field is 27.12 MHz and the absorbed power by the plasma is 85 -275 W. The dependence of spectral line intensities on various parameters (plasma power, Ar flow-rate, observation height, angle of the conical sample) has been studied. The excitation temperature of Ar atoms has been determined too, and the detection limits for some elements in brass and low-alloy steel are presented.

INTRODUCTION

In atomic spectrometry, direct analysis of conductive and nonconductive solid samples without chemical treatment is very important. Dissolution of solids to be introduced into the excitation source consumes time and can determine the contamination of samples and the deterioration of sensitivity of analysis method.

Many kinds of plasma excitation sources for solid samples are known. Its included dc(Arc) and ac(Spark) plasmas, inductively coupled plasmas (ICP), capacitively coupled plasmas (CCP), glow discharges (GD), flowing afterglows, Theta-pinch discharges, exploiding films and wires, and laser produced plasmas [1].

Capacitively coupled plasma at atmospheric pressure principally has been used for the analysis of liquid samples [2 - 6] and as detector for gas chromatography [7,8]. It has been tested as spectral source for direct analysis of solid samples. Liang and Blades [9] combine the high efficiency of atomization in electrothermal atomizers with the high efficiency of excitation in rf plasmas. They achieved an excitation source with atomization in graphite furnace for plasma emission spectroscopy (FAPES). The working frequency was of 27 MHz, the power into the plasma was in the range of 100 - 600 W and the gas-flow rate (Ar) was 1 l/min. The detection sensitivities were lower than one picogram for some elements. In the microwaves domain (2450 MHz, 500 - 700 W) Ali et al. [10] employing a modified conventional ICP torch placed into a resonant cavity have analyzed powdered solid samples. The detection sensitivities were in the ng domain.

[1] Babeş-Bolyai University, Faculty of Physics, Cluj-Napoca, Romania

In this work a new method for direct analysis of conductive samples is presented. The same kind of plasma torches as in the work [6] is used, the solid sample being placed on the sustaining electrode of the plasma. In the system described below, both atomization and excitation steps are interpreted.

EXPERIMENTAL

The experimental set-up is shown in Fig.1 and the components are listed in Table I. Fig.2 shows the torch and the sample place. The generated plasma is one of tip-ring type, being in contact with only one electrode, which is as well the sample. It has a conical shape being placed on the top of a cylindrical brass piece (8 mm o.d. and 60 mm in length). They are inserted into a quartz tube (15 mm i.d., 18 mm o.d. and 100 mm in length) sustained by the introduction system of the plasma gas (Ar). The Ar introduction system is made of Teflon (PTFE) and has twelve equidistant cylindrical holes surrounding the plasma sustaining electrode. This assures the laminar introduction of the plasma gas that is an important condition for plasma stability. At a distance of 40 mm from the sample tip, the quartz tube is surrounded by an annular counterelectrode that assures the symmetry of the electromagnetic field lines, therefore the symmetry of the discharge.

Table I Instrumentation for capacitively coupled plasma as excitation source for solid conductive materials

Instruments/Components	Manufacturer
Spectrometer • 1m, 2400 groves/mm, • linear dispersion, • 0.5 nm/mm	Research Centre for Analytical Instrumentation Cluj-Napoca, Romania
RF Generator • free-running, • Colpitts oscillator, • 27.12MHz,50-300 W	Research Centre for Analytical Instrumentation Cluj-Napoca, Romania
Computer • Telerom P - 386	IEIA Cluj-Napoca, Romania
Torch	Laboratory made

Capacitively coupled plasma at atmospheric pressure of tip-ring type has four characteristic zones that confers it an inhomogeneous appearance (Fig.2). In the immediate proximity of the plasma sustaining point one can observe a thin blue-violet layer, named superficial luminescence, with a thickness lower than 1 mm and which has all characteristics of a normal cathode fall. The plasma consists of a thread form core that has the highest temperature (3500 - 4000 K) and which in argon is brilliant-white, and a blue-light coat less brilliant and cooler than the core, and which surround it. The last two zones are separated by the superficial luminescence through a dark space

similar to the dark spaces of luminescent discharges in direct current. From analytical point of view the core and the luminescence are important.

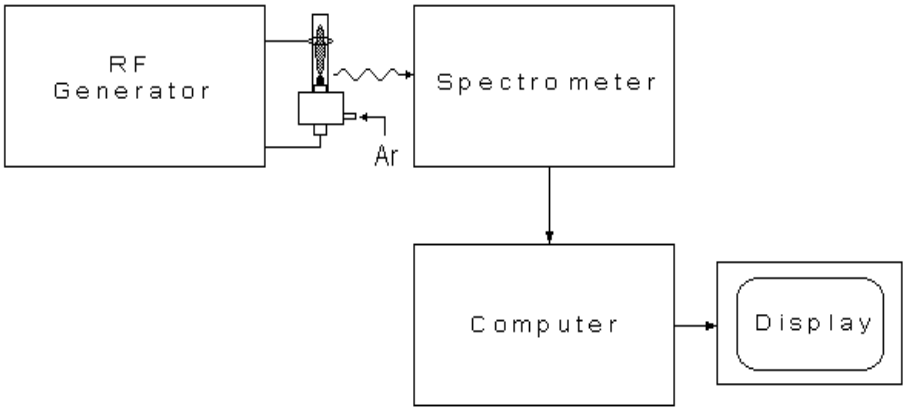

Fig.1. - Experimental set-up for CCP Used as spectral source for solid conductive samples.

The sample form and dimensions are shown in Fig.2.

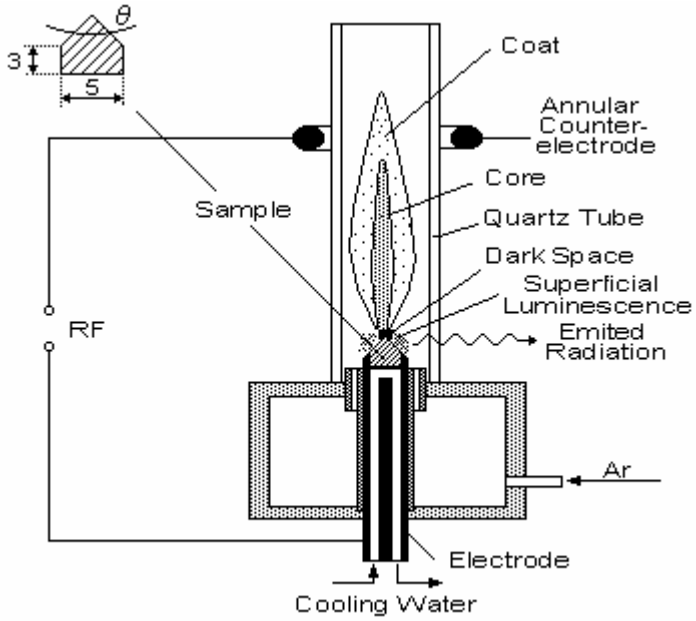

Fig. 2. - Schematic diagram of CCP torch and dimensions of the sample (mm).

In the alternance of the electromagnetic field in that the electrode has a negative potential, the positive ions are accelerated in the very intense electric field of the normal cathode fall. The energized ions collide the sample and their kinetic energy determines the surface atoms to be ejected (solid sampling by sputtering phenomenon). The atoms penetrate into the superficial luminescence and the core of the plasma where they are ionized and excited, and emit their characteristic line spectra. Because an overheating of the sample electrode tip could make the both processes hard to control, the lower electrode of the torch is water coolled.

RESULTS AND DISCUSSION

Brass and low-alloy steel have been used as samples. In a first stage the influences of the power into the plasma, plasma gas flow-rate, observation height measured on the tip of the sample and the angle of the cone on the relative intensities of the emission lines and on relative standard deviation were studied. These dependencies are presented in Fig. 3 - 7.

The rise of the spectral line intensity when the plasma power is increased (Fig.3) can be correlated both with the increase of the density of the positive ions that are accelerated in the normal cathode fall and the increase of the excitation temperature of the plasma.

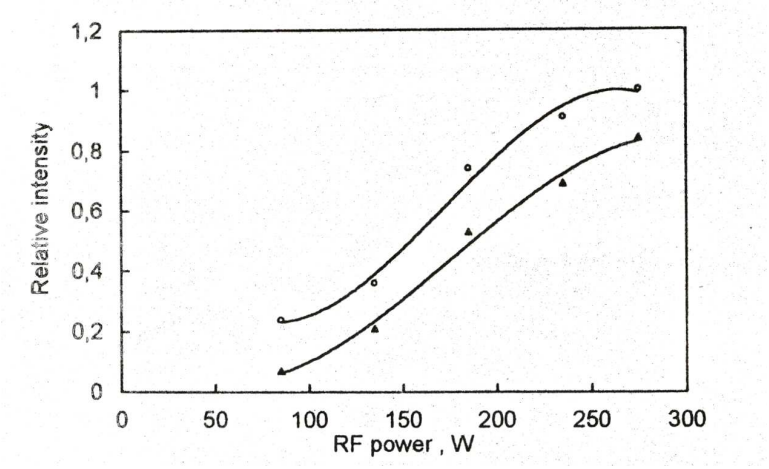

Fig. 3 - Effect of plasma power on emission intensity for Zn - O at 213.861 nm and Pb - Δ at 405.783 nm from brass. Gas flow-rate, 0.62 l/min and $\theta = 90^{o}$.

The gas flow-rate influences both the plasma absorbed energy and the time residence of the atoms in the plasma. At the flow-rates lower than 0.4 l/min the plasma volume decreases and its core disapears because of air difussing in the upper part of the torch. Consequently, the emission intensity strongly decreases. The increase of the gas flow-rate above 0.4 l/min is accompanied by changes of the dimensions and the plasma

appearance. At this flow-rate the core and the superficial luminescence of the plasma become visible and the intensities of the emission lines increase. At gas flow-rates higher than 0.7 l/min the emission intensity again decrease, this time because of a reduced time residence of atoms in the plasma (Fig.4). For gas flow-rates in the range of 0.4-0.7 l/min the emission intensity is maximum and the relative standard deviation is minimum.

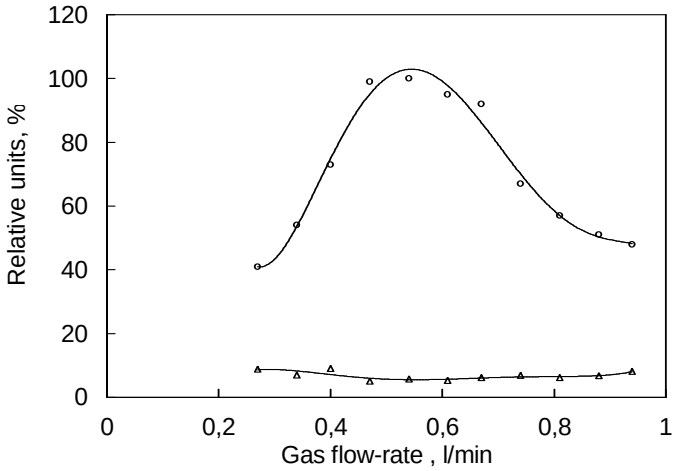

Fig. 4. - Effect of gas flow-rate on emission intensity - O and RSD - Δ for Zn at 213.861 nm. Plasma power, 135 W and θ =90^{O}.

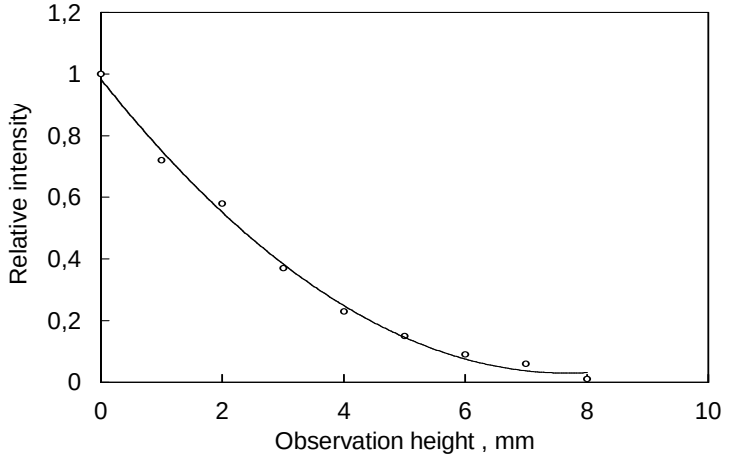

Fig. 5 - Emission intensity for Zn from brass at 213.861 nm at different observation heights. Plasma power, 135 W, gas flow-rate, 0.62 l/min and θ =90^{O}.

The decrease of the emission line intensities when the observation height is increased (Fig.5) is due to the decrease of the temperature in the core of the plasma on the one hand and of the diminution of the number of the sampling atoms that are acceded in this zone on the other hand. From Fig.6 one can observe that if the sample is sharper the excitation process is more efficient because of the increased electric field in the neighbourhood of the sample tip. For angles smaller than 60^0, the sample is overheated and the accidental thermal emission determines plasma instabilities.

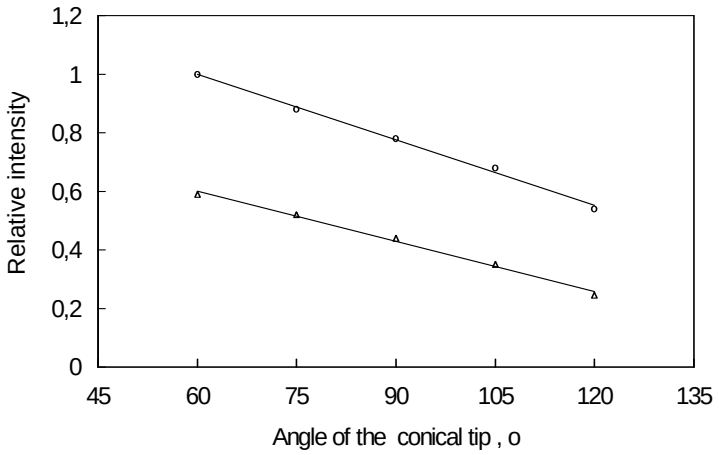

Fig. 6. - Emission intensity for Pb - O from brass at 405.783 nm and Mn - Δ from low-alloy steel at 403.076 nm as function of angle of conical sample.
Gas flow-rate, 0.62 l/min and plasma power, 135 W.

It has been studied too the dependence of the relative standard deviation (RSD) on the plasma power (Fig.7).

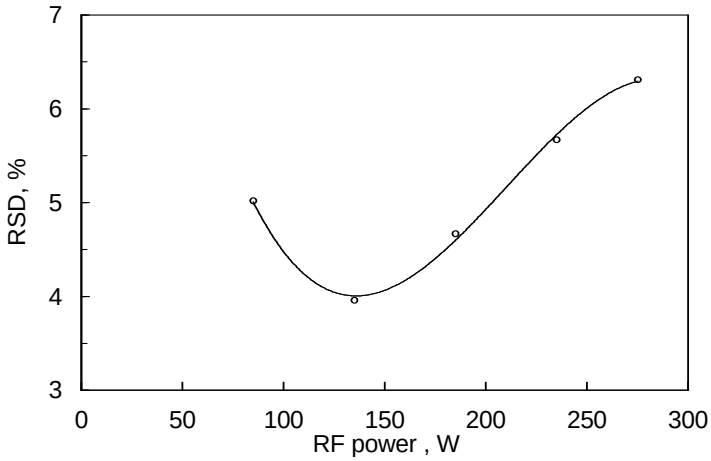

Fig. 7. - RSD for emission line of Zn at 213.861 nm at different RF powers. Gas flow-rate, 0.62 l/min and $\theta = 90^{o}$.

It has been obtained a minimum at the plasma power about 150 W. At the powers lower or greater than 150 W RSD increases because of the lower sampling efficiency and also due to the rise of the electrothermal emission.

Also it was observed that the distance between the sustaining tip of the plasma and the annular counterelectrode has not influences on the emission line intensities when this parameter was in the range of 10 - 60 mm, because of the power and the appearance of the plasma remain unchanged.

Excitation temperature of Ar atoms in the superficial luminescence of the plasma was calculated from the slope of a Boltzmann-plot prepared by using the plasma as thermometric species. Table II summarizes the spectroscopic data for selected Ar lines. Here λ is the wavelength of the transition, g - the statistical weight of the lower level, f - the oscillator strength and E_{exc} - the excitation energy of the upper level of the observed transition. The correction of the measured line intensity (I) of the spectral line was based on the calibration of the detection system. It was calibrated in the 400-800 nm range with a spectral radiance standard lamp type EPI 1604. Fig.8 presents a typical plot for the Ar lines obtained at the operating power of 135 W.

Table II Spectroscopic data for Ar lines

λ [nm]	Eexc [eV]	gf
340.62	15.47	0.0382
419.83	14.59	0.0246
430.01	14.51	0.0169
451.07	14.58	0.0101
555.87	15.14	0.0740
557.26	15.32	0.0457
603.21	15.13	0.2178

The precision of the measurement of individual line intensities was within a few percent RSD. The temperature, determined from the slope of the plot using the equation:

$$\log \frac{I\lambda^3}{gf} = \text{const} \cdot - \frac{5040}{T} E_{exc} \quad (1)$$

has an estimated uncertainty of 15%. It is about 3880 K.

The detection limits (DL) was calculated using 3σ criteria:

$$DL = \frac{3 \times 0.01 \times RSD \times X_B}{X_A} \times C_o \quad (2)$$

where X_A is net analyte signal, X_B - background signal and C_O - analyte concentration.

The results for a few elements contained in brass and low-alloy steels are listed in Table III. The liquid monoelement solutions pneumatically nebulized into the plasma were employed solely for the identification of analyte emission lines. Figure 9 presents a calibration curve for vanadium from low alloy-steel which is linear over three orders of magnitude, starting from a concentration five times DL.

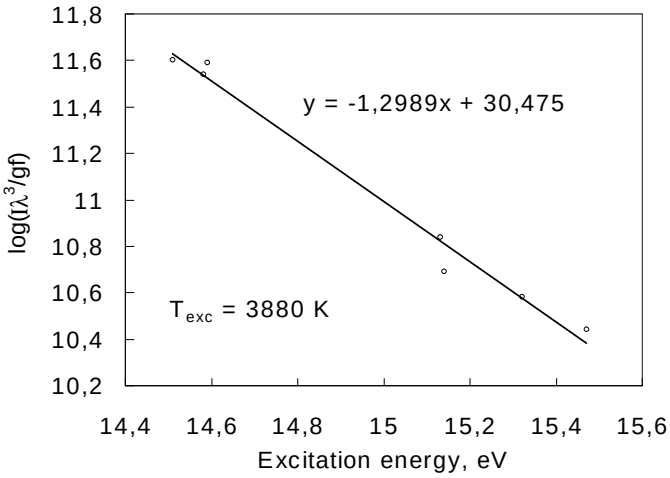

Fig. 8. - Boltzmann-plot for Ar at 135 W rf power

Table III. Detection limits of some elements from brass and low-alloy steel

Element	l [nm]	DL [%]
Brass		
Pb	405.78	0.03
Low-Alloy Steel		
Co	345.35	0.003
Cr	425.43	0.01
Mn	403.07	0.05
Mo	386.41	0.02
Ni	352.45	0.03
V	437.92	0.003

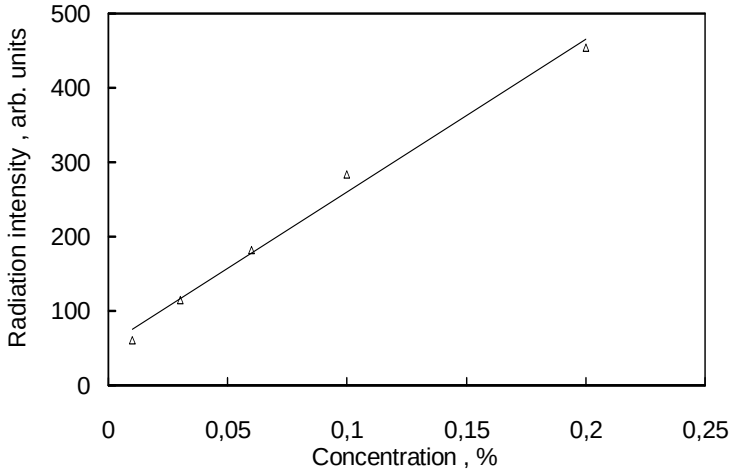

Fig.9. - Calibration curve for V in low-alloy steel at 437.324 nm. Gas flow-rate, 0.62 l/min and plasma power, 135 W.

The simplicity of the system described above, the low cost and the easiness of operation and its promising performances can determine a further development of this analyzing method.

REFERENCES

1. W. Blades, P. Banks, C. Gill, D. Huang, C. Le Blanc, IEEE *Trans. Plasma* Sci. 19, 1090 (1991).
2. C. Liang, M. W. Blades, *Anal. Chem*. 60, 27 (1988).
3. D. Hwang, W. Masamba, B. W. Smith, J. D. Winefordner, *Can. J. Spectrosc*. 33, 156 (1988).
4. E. Sturgeon, S. N. Willie, V. Luong, S. S. Berman, *Atom. Spectrom.* 4, 669 (1989).
5. Cordos, S. D. Anghel, A. Fodor, XXVII *Coll. Spectrosc*. Intern. vol. C. 22, Bergen, Norway 1991.
6. Tataru, S. D. Anghel, *Roum. J. Phys*. 37, 785 (1992).
7. Huang, M. W. Blades, *J. Anal. Atom. Spectrom*. 6, 215 (1991).
8. Huang, D. C. Liang, M. W. Blades, *J. Anal. Atom. Spectrom*. 4, 789 (1989).
9. C. Liang, M. W. Blades, *Spectrochim. Acta* 44B, 1059 (1989).
10. N. Ali, K. C. Ng, J. D. Winefordner, *J. Anal. Atom. Spectrom*. 6, 211

STUDIA UNIVERSITATIS BABEŞ-BOLYAI, PHYSICA, XLI, 2, 1996

LOCAL SOFTENING OF HARD SHELLED SEMIPRODUCTS BY USING PLASMA GENERATOR

IOAN BICA[1]

ABSTRACT. The work presents the experimental results concerning the local softening of Diesel motor cylinders with plasma using a specialized plasmagenerator.

Key Words:(localsoftening),(plasma generator), (softening temperature), (cutting tool).

1. INTRODUCTION.

Cylinders for Diesel motors, are obtained through centrifugal chill casting of grey cast iron. The marginal surfaces of the cylinders have a high hardness (≥ 250 HB) shell.The oughing by cutting of the shell leads to a high consumption of cutting tools as well as to a reduced Specific discharge of chips.

In order to decrease the consumption of the cutting tool and to increase the specific discharge of chips, the marginal surfaces of the cylinder are locally heated in the ransferred electric arc plasma [1,2,4].

The transferred electric arc plasma increases the temperature of the hard shell in the cutting zones and consequently, the cutting forces diminish.Intuitively, it is not possible to have a cutting area with local plasma heating. It is necessary to correlate the plasma heating area (the power of the transferred electric arc plasma, the distance between the plasma generator and cutting tool, radius of anodic patch) and the cutting area (cutting rate, advance of cutting tool, depth of cutting) of the semiproduct, in order to obtain a good cutting regime, comparable to the usual one. There are known the roughing technologies by cutting of hard and superhard steel semiproducts [2,3]. Roughing by cutting of semiproducts with hard shell are less well nown.

In the paper there are presented the analytical temperature distribution in the cuttingzone, as well as the temperature distribution on the cutting edge,at the local plasma heating for roughing of the marginal surfaces of the Diesel engine cylinders. There are evidenced the conditions necessary to attain locally the plastifying temperature of the hard shell, the temperature gradient at the cutting edge which ensure, as much as possible, the uniform ear of the tool, as well as the temperature area of the

[1] University of Timişoara, str. V. Pârvan 4, 1900 Timişoara, Romania.

roughed surface which do not produce unwanted phase transformations and thermal deformations of the cylinder.

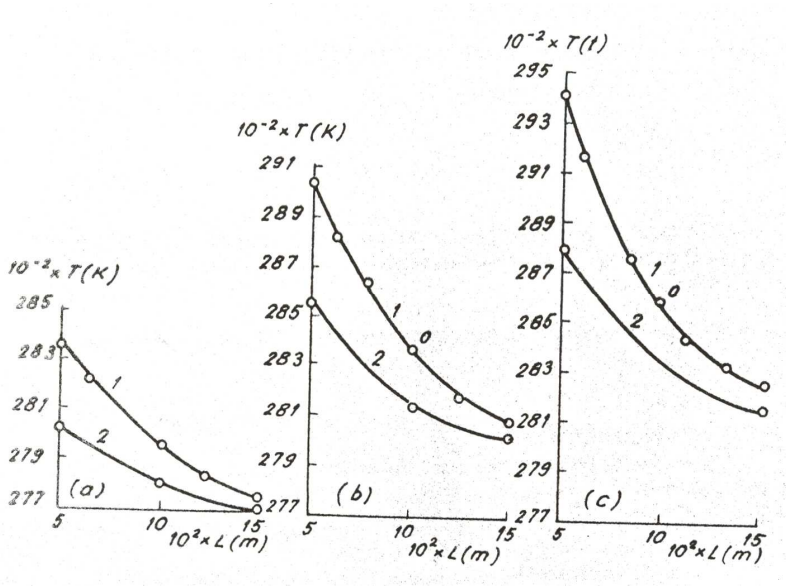

Fig.1. Roughing by cutting of the shell on the outside surface of the cylinder for Diesel motor (schematic diagram)

where: 1 - plasma generator; 2 - current source; 3 - cylinder; 4 - cutting tool; AB - cutting width; S - cutting tool feed rate; Ox,Oy,Oz - the axes of the orthogonal coordinate system Oxyz; L - the distance between the plasma generator and the cutting tool measured on the circumference of the cylinder; n - the number of rotations of the machine tool.

The theoretical results are compared with those obtained experimentally under semiindustrial conditions.

2. CALCULATION OF TEMPERATURE DISTRIBUTION

2.1. *Description of the procedure*

The limited heating with the plasma arc of the cylinder for Diesel motors which is roughed by cutting is presented in Figure 1.

The plasma generator 1, connected to the current source 2, heats the cylinder 3 along the cutting width:

$$AB = b = \frac{t}{\sin\chi} \tag{1}$$

where:

- b is the cutting width, m;
- t is the cutting depth, m;
- χ is the plan approach angle of the cutting tool.

The heated zone is cut by the cutting tool and then driven away. The roughed surface remains at a lower temperature as compared to that of the cutting area.The plasma generator 1, from Figure 1, is placed at a distance L from the cutting tool 4. The roughing speed of the cylinder is v.

2.2. Temperature distribution of cylinder

An orthogonal coordinate system Oxyz is attached to the cutting area of the cylinder for Diesel motors, as in Figure 1.

The sense of rotation of the workpiece is chosen to ensure that the heated zone reaches on the shortest way the edge of the cutting tool.Consequently, the positive sense of the Ox axis is opposed to the velocity vector in the origin of the Oxyz coordinate system (fig.1).

Taking into consideration that the plasma arc is a concentrated energy source having a cylindrical form the relation for the temperature in the cutting area results as follows [2,3]:

$$T(x,y,z)_{x=-L} = \frac{0.16 \cdot P \cdot \eta}{\lambda \cdot L} \sqrt{\frac{a_0}{a_0 + K_1} \cdot exp(-10^4 \cdot K_1 \cdot y^2) \cdot exp\left(-\frac{10^4 \cdot a_0 \cdot K_1 \cdot z^2}{a_0 + K_1}\right)} \quad (2)$$

where:

- $T(x,y,z)|_z = -L$ is the temperature in the coordinate point (-L, y, z) situated on the cutting tool edge, K;
- P is the power in the plasma arc, W;
- η is the plasma heating efficiency of the cylinder;
- L is the distance between the plasma generator and the cutting tool, measured on the circumference of the cylinder, m;
- a_0 is the confinement coefficient of the plasma arc, m^{-2}.

The confinement coefficient of the argon plasma arc is determined by means of the relation [2,3]:

$$a_0 = \frac{3 \cdot 10^{-4}}{r^2} \quad (3)$$

where r is the anodic spot radius, m.

K_1 from the relation (2) is expressed by means of the relation [2,3]:

$$K_1 = \frac{25 \cdot 10^{-6} \cdot v}{\omega \cdot L} \quad (4)$$

where:

- v is the cutting speed, $m \cdot s^{-1}$.
- is the thermal diffusivity of the shell on the marginal surfacesof the cylinder, $m^2 s^{-1}$

Taking into consideration the case in Figure 1(x = -L and z = 0), the relation (2) becomes:

$$T(x,y,z)_{x=-L} = \frac{0.16 \cdot P \cdot \eta}{\lambda \cdot L} \sqrt{\frac{a_0}{a_0 + K_1} \cdot exp(-10^4 \cdot K_1 \cdot y^2)} \tag{5}$$

The values of radius r of the anode spot was experimantally determined. The used procedure is described in the paper [4]. For different values of P in the plasma arc of $10 \cdot 10^3$ W; $16.5\ 10^3$ W and $20 \cdot 10^3$ W, the average value of the anode spot radius is r = $4 \cdot 10^{-3}$ m. The research work for the temperature distribution in the cutting area is performed by using the relation (5).

The mean experimental values of the thermophysical constants for the hard shell of
the cylinders are as follows [1]:
- the softening temperature: T_p=873 K ± 10%;
- the melting temperature: T_t=1573 K ± 10%;
- the thermal conductivity: λ = 0,04 W m^{-1} K^{-1};
- the thermal diffusivity: $\omega = 25\ 10^{-6}$ m^2 s^{-1}.

2.3 Temperature distribution of cutting tool

During the roughing operation by limited heating by plasma arc the cutting tool gets warm. The temperature at a certain point on the cutting tool edge results from relation (5) multiplied by a β coefficient [2,3] i.e.:

$$T_s(x,y,z) = \beta\ T(x,y,z) \tag{6}$$

where:
-T_s (x,y,z) is the temperature at a certain point on the cutting tool edge, K;
-T(x,y,z) is the temperature at a point of the cutting edge, K.

The β coefficient takes into account the heat storages in the material. For the hard shell [1], β =1.5.

The cutting tool wear when roughing by cutting with plasma arc limited heating is due to the non uniform distribution of the temperature along its cutting edge length [3].

To study the temperature distribution on the cutting tool edge the thermal uniformity coefficient μ is introduced. It is defined by means of the relation [1,3]:

$$\mu = \frac{T_s(L, y, \frac{b}{2})}{T_s(L, y, O)} \tag{7}$$

where:

-T_s (L, y, b/2) is the temperature at a point situated at the end of the cutting tool edge, K;
-T_s (L, y, O) is the temperature at a point situated in the middle of the cutting tool edge.

The relation (8) for coefficient of thermal uniformity was obtained by replacing the relation (5) in the expression (7) and taking into account the expressions (3) and (4):

$$\mu = exp\left[-\frac{3v \cdot b^2}{4(12\omega \cdot L + v \cdot r^2)}\right] \tag{8}$$

As the origin of the coordinate system Oxyz is chosen at a point corresponding to the half of the cutting width b, see Figure 1, there results:

$$z = \pm\frac{b}{2} \tag{9}$$

Introducing the relation (9) in relation (8) there results the dependence of the thermal uniformity coefficient μ, on the z variable, i.e.:

$$\mu = exp\left(-\frac{3z^2}{12\omega \cdot L + v \cdot r^2}\right) \tag{10}$$

3. EXPERIMENT

The experiments concerning the usual cold roughing by cutting of the shell from the marginal surfaces of the cylinder were compared to roughing by plasma arc limited heating.

The experimental installation which has been used is described in the paper [5]. A specialized plasma generator was developed in order to perform inside the cylinder the roughing by cutting through limited heating with plasma arc. Its description and technical characteristics are presented in paper [6]. The experimental tests are presented in **Table 1.**

Nr. crt.	I (A)	U (V)	$10^3 \cdot D$ ($Nm^3 \cdot s^{-1}$)	v ($m \cdot s^{-1}$)	$10^3 \cdot S$ ($m \cdot rev^{-1}$)	$10^3 \cdot t$ (m)	L (m)	$10^3 \cdot d$ (m)	$10^3 \cdot d_a$ (m)
1.	250	60	1/3	2.00	0.38	4	0.10	10-12	3.5
2.	260	60	1/3	2.00	0.5	4	0.10	10-12	3.5
3.	275	60	1/3	2.00	0.6	4	0.10	10-12	3.5
4.	300	60	1/3	2.00	0.7	4	0.10	10-12	3.5

I - the electric current intensity of the plasma arc;
U - the voltage of the plasma arc;
D - the argon flow rate;
v - the cutting speed;
S - the cutting tool feed rate;
t - the cutting depth;

L - the distance generator-cutting tool, measured on the circumference of the Diesel motor cylinder;
d - the distance between the plasma generator nozzle and hard shell of the Diesel motor cylinder;
d_a - the diameter of the plasma generator nozzle.
The cutting tool used during the experiments has small plates, characterized by the following geometry:

-plan relief angle: $\alpha=12^0$
-plan clearance angle: $\gamma=-6^0$
-plan approach angle: $\chi=45^0$
-secondary approach angle: $\chi_1=45^0$
-inclination angle: $\chi'=-3^0$
-radius: $r'=0.3\ 10^{-3}$m

To avoid the heat storages inside the cylinder air should be blasted at a flow rate of 0.2 $Nm^3\ s^{-1}$.The roughing by cutting of the shell from the marginal surfaces of the cylinder is performed when the cutting width has the value $b=6\ 10^{-3}$m.

4. RESULTS AND DISCUSSION

Figure 2 shows the temperature distribution, T, in the cutting area for the depthy, in the Diesel motor cylinder wall.

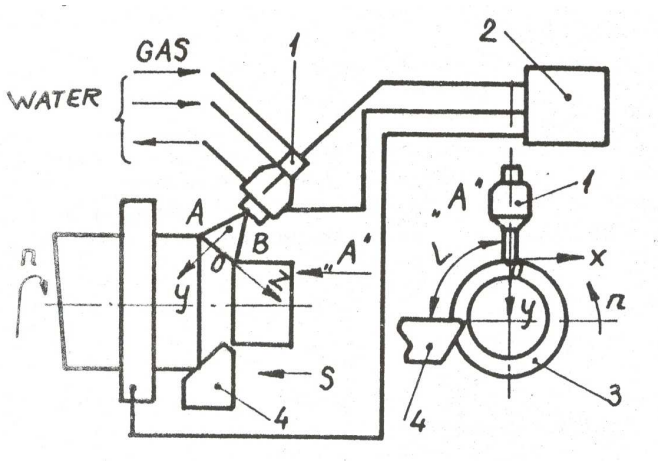

Fig. 2. The temperature distribution, T, in the cutting area for the depth, y, in Diesel motor cylinder wall.

The experimental results in Fig. 2 are for:
-the power in the plasma arc: (a) $P=10\ 10^3$W; (b) $P=16.5\ 10^3$W; (c) $P=20\ 10^3$W;
-the cutting speed: (1) $v=1$m s^{-1}; (2) $v=2$m s^{-1}; (3) $v=3$m s^{-1};

-the distance between the plasma generator and the cutting tool:L = 0.10 m;
-material: cast iron;
- o - experimental values.

For the power P = 10 10^3W in the plasma arc, the temperature on the cylinder surface (y=o m) is T=1023 K, when the cutting speed is v=1.0m s^{-1} and generator - cutting tool distance L=0.10 m. When the cutting speed increases the temperature on the surface of the cylinder decreases. When the cutting speed is v=3m s^{-1} and the power is the same in the plasma arc (P=10 10^3W), (Figure 2 a), the temperature on the surface of the cylinder is T=843 K.

The maximum temperature on the surface of the cylinder is 1773 K when the cutting speed is v=1 m s^{-1} and the plasma generator-cutting tool distance is L=0.10 m as in Figure 2 c.

In the depth of the cylinder wall the temperature decreases exponentially to values up to 373K as in Figure 2.

The temperature in the cutting area decreases as the distance L between the plasma generator and the cutting tool increases, (see Figure 3).

The results in Fig. 3 were obtained by using: the cutting speed: v = 1 m s^{-1}; depths in the cylinder wall: (1)y = 0 m; (2)y = 1 10^{-3}m; powers in the plasma arc:(a) P = 10 10^3 W; (b) P = 16.5 10^3W; (c) P = 20 10^3 W; material: the hard shell on the marginal surfaces of the Diesel motor cylinder o - experimental calues.

If at the distance L=0.05 m the temperature on the surface of the cylinder is T=1353 K for P=10 10^3W T=2043 K for P=16.5 10^3W and T=2373 K for P=20 10^3W then at a distance L=0.15 m the temperature on the surface of the cylinder will become: T=733 K for P=10 10^3W, T=1063 K for P=16.5 10^3W and T=1233 K for P=20 10^3W.

On the bases of the data from Figure 3 the temperature gradient module in the cylinder wall was calculed. The calculed values are given in Table 2.

$10^{-3} \cdot$ P (W)	$10^{2} \cdot$ L (m)	$10^{-4} \cdot \Delta T/\Delta y$ ($K \cdot m^{-1)}$
10	5	36
	10	14
	5	4
16.5	5	50
	10	26
	5	8
20	5	60
	10	28
	5	12

where:
P - the power in plasma arc; L - the distance between the plasma generator and the cutting tool, measured on the circumference of the Diesel motor cylinder; $\Delta T/\Delta y$ - the temperature gradient module.

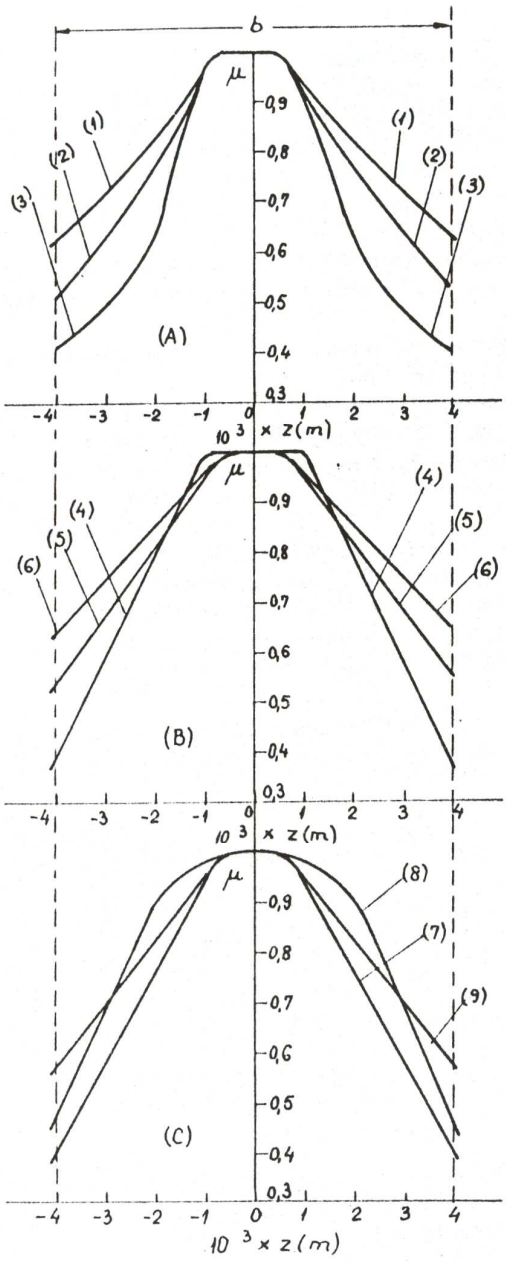
b
μ
0,9
0,8
0,7
0,6
0,5
0,4
0,3
(1)
(2)
(3)
(A)
-4 -3 -2 -1 0 1 2 3 4
10 3 x z(m)
(4)
(5)
(6)
(B)
(7)
(8)
(9)
(C)

Fig. 3. The temperature distribution, T, in the cutting area, depending on the distance, L, between the plasma generator and the cutting tool

From Table 2 there can be observed that the temperature gradient module decreases when the distance L between the plasma generator and the cutting tool increases.

Having in view the thermophysical constants of the cylinder shell (the melting temperature T_t =1573K ± 10%; the softening the temperature T_s=873K± 10%) there was used a cutting regime with limited heating by plasma arc corresponding to the curve 2 in Figure 2b.

The optimum area of roughing by cutting with plasma arc limited heating of the outside and respectively inside surfaces of the cylinder corresponds to the number 3 in Table 1. When the electric current intensity is I=275 A_{dc} the cutting temperature, measured with an electric resistance pyrometer is T=1273K ± 10%.

For electric current intensities I > 275 A_{dc}, the temperature at the cutting area exceeds the melting temperature of the shell and the cutting tool is thermally strongly affected.The temperature at the roughed surfaces measured with an electric resistance pyrometer does not exceed 373 K. The dependence of the thermal uniformity coefficient μ, along the length of the cutting tool (axis Oz, see Figure 1), is presented in Figure 4.

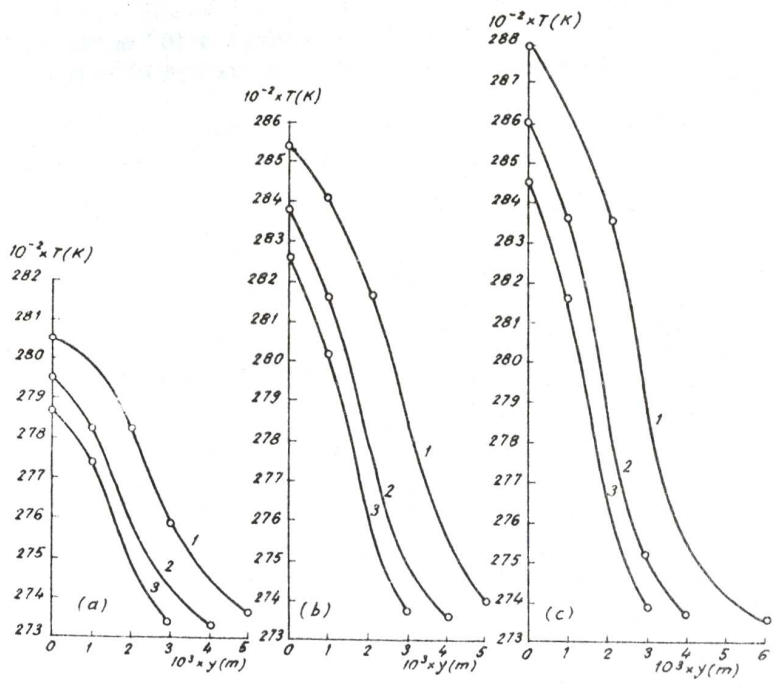

Fig. 4. The dependence of the non-dimensional magnitude μ on the z coordinate

case (A):
-the cutting speed: (1) v = 1m s^{-1}; (2) v = 2m s^{-1}; (3) v = 3m s^{-1};
-the distance between the plasma generator and the cutting tool: L = 0.10 m
-the anode spot radius: r = 4 10^{-3} m.

case (B):
-the cutting speed: v = 2m s^{-1}
-the distance between the plasma generator and cutting tool: (4) L = 0.05 m; (5) L = 0.10 m; (6) L = 0.15 m;
-the anode spot radius r=4 10^{-3} m.

case (C):
-the cutting speed: v = 2m s^{-1}
-the distance between the plasma generator and cutting tool: L = 0.10 m
-the anode spot radius: (7) r = 3 10^{-3} m; (8) r=4 10^{-3}m; (9) r=5 10^{-3} m.
Observation:b is the cutting width, m.

The temperature along the length of the cutting tool edge tends to become uniform for low values of the cutting speed, (see Figure 4A-curve 1). When the cutting speed is constant,(see Figure 4B), the temperature along the length of the cutting tool edge tends to turn uniform for high values of the distance L, between the plasma generator and the cutting tool (curve 6).

On the other hand, for the anode spot radius r=4 10^{-3} m, the temperature along the length of the cutting tool, on the cutting distance b=4 10^{-3}m is uniform (see Figure 4C-curve 8).

By increasing the value of the anode spot radius up to r=5 10^{-3} m, there results the thermal non-uniformiy of the cutting tool when the cutting width is b=4 10^{-3}m.

On the extremities of the cutting tool edge (b=8 10^{-3} m), the temperature has higher values (μ =0.57) for the anode spot radius r=5 10^{-3}m (curve 9), as compared to the temperature in the same points of the cutting tool, but for the anode spot radius r=4 10^{-3}m (curve 8).

According to the data presented in Figure 4B-curve 5, the thermal uniformity coefficient of the cutting tool is μ =0.75. This leads to the conclusion that the wear of the cutting tool is reduced. The maximum cutting values used corresponding to roughing the cylinder without any heating are presented in Table 3.

Table 3:

v_0 ($m \cdot s^{-1}$)	$10^3 \cdot S_0$ ($m \cdot rev^{-1}$)	$10^3 \cdot t_0$ (m)
1.33	0.22	3

where:
v_0 - the cutting speed;
S_0- the cutting tool feed rate;
t_0 - the cutting depth.

The working life of the cutting tool having an average wear VB_{av}=0.8 10^{-3}m,

is τ_0=15 s.

Indeed, by using the plasma limited heating cutting regime from Table 1 (number 3) it comes out that for the same average wear $VB_{av}=0.8\ 10^{-3}$ m, the working life of the cutting tool is τ = 165s.

The working life of the cutting tool has increased τ/τ_0=11 times when the plasma arc limited roughing was performed, as compared to the usual roughing of the shell from the marginal surfaces of the cylinder.

Using the roughing regime in Table 3 and respectively that in Table 1 (number 3) it follous that the specific discharge of chips is higher by roughing with plasma arc limited heating as compared to the usual roughing.

There have been noticed certain cylindricity deviations of not more than $\pm 0.55\ 10^{-3}$ m on the radius as a result of the plasma arc limited heating of the marginal surfaces of the Diesel motor cylinders. As the processing by cutting for the final dimensions is commonly performed, these deviations are not significant.

5 CONCLUSIONS

1. For the cutting area, the temperature in the cutting area is of 1273K ± 10%. At depths of $y=4\ 10^{-3}$ m in the cylinder wall the temperature is up to 373 K.
2. The specific volume of chips increases 5.3 times when roughing by means of plasma arc limited heating as compared to the specific volume of chips when using the common roughing.
3. For the cutting area, the theoretical value of the ratio between the temperature at the cutting tool edge and the temperature at the half of the cutting tool is μ = 0.75.
4. Correspondingly the working life of the cutting tool when roughing by means of the plasma arc limited heating increases 11 times as compared to the commonly used roughing.
5. The analytical model for roughing by cutting with limited heating with plasma arc of hard steel semiproducts gives satisfactory results also in the case of semiproducts with hard shell.

REFERENCES

1. I. Bica, *"Researches concerning the physics and technology of thematerials by using the direct current thermal plasma"*, Doctoral thesis, University of Timišoara, (in Romanian), 174 (1991);
2. S. S. Kravcenko, *"The influence of the plasmo-mechanical regime parameters on the temperature distribution in the cutting area"* (in Russian), Fizica i himia obrabotki materialov, no.4, 30-34 (1982);
3. S. S. Kravcenko, *"The temperature distribution on the cutting tool edge when using plasmo-mechanical materials processing"* (in Russian), Mashinostroenie, no.3 (1982) p.141-145;
4. I. Bica, C. Marin, *"An experimental method for determination of anodic spot diameter"*, The annals of Timišoara University Physics series, no.31,39-45 (1994);
5. I. Bica *"Installation for plasma softening of the hard shelled semiproducts"*, The Annals of Oradea University, Physics series (in press).
6. I. Bica, *"Plasma local softening of hard shelled semiproducts"*, Romanian Reports in Physics (in press).

STUDIA UNIVERSITATIS BABEŞ-BOLYAI, PHYSICA, XLI, 2 1996

REMARKS IN N=1 SUPERSYMMETRIC GAUGE THEORIES

RADU TATAR[1]

ABSTRACT. In the present paper we are developing some new facts concerning the dynamically generated effective potentials and the vaacuum structure for N=1 supersymmetric theories. We are using theories with different gauge groups and we are trying to obtain connections between these theories. As a first example, in this paper we are considering the case of unitary groups SU and SP and we are showing that for specific ranges of N_c and N_f, the theories based on these groups are equivalent in the sense introduced in this paper (they have the same effecctive potential and the same vacuum structure). For other ranges, the SP theory is equivalent with SU on some singular points of the last one.

1. INTRODUCTION

There are already 2 years since the exploring of four dimensional supersymmetric field theories which are exact has started with the work of Seiberg [2] when the number of flavors and the number of colors are within specific ranges.

Ever since, a large amount of work have been done in this area for all types of classical gauge groups [3] [6] [7] and even for some exceptional groups as G_2 in [8] [9]. For all these theories the effective potentials were obtained for all ranges of the number of colors and number of flavors. Besides, many results have been obtained for the different phases of the theories (for a very detailed discussion see [11]).

Another achievement made in these theories was the discovery of an electric-magnetic type duality for these theories [10] which is the analog of the dualities appearing in N=2 [12] and N=4 [13] [14] supersymmetric theories. Besides the original approach of [10] which considered fermions only in the fundamental representation, later results considered also fermions in the adjoint representations and other cases. [16] [17]

What appears to be rather interesting is that for theories with different gauge groups, the form of the effective potential can be the same, fact which is of course simply connected with the Dynkin index for the fundamental and adjoint representations for different groups. Moreover, it turns out that the number of vacuum states can be the same for two different theories. Starting from these two observations, we introduce the concept of equivalence between such two theories. The concept of duality is apparently

[1]University of Miami Coral Gables, Florida, 33124, U.S.A.

weaker than the concept of duality because for equilavence we are not requiring the 'tHooft anomaly condition.

The equivalence concept can give another classification of theories, besides the group structure classification and the duality. When one takes the combination of duality and equivalence, the spectrum of dualities, which are defined only for the theories with the same type group (SU, SP, SO, etc) can be extended to a type of duality between theories with different types of groups (this we denote by equduality).

We analyse the possible connection between 2 theories with different gauge groups, one with SU (N_c) and the other one with SP($2N_c$ - 2), both having the matter content in the fundamental representation. We will show that in some cases two such theories can be taken equivalent, in thee sense that they have the same effective potential and the same number of vacuum states. We also try to make an attempt to discuss their dualities, which could enlarge the set of dual theories to theories with different gauge groups.

A summary of our results is the following. For N_f (N_c - 1, we find that SU(N_c) and SP($2N_c$ - 2) give the same effective poteential and have the same number of vacuum states.

In section 2 we discuss briefly the results of [2], [3] for the SU groups and the results of [7] for SP groups.

In section 3 we are considering the case $N_f \leq N_c$ - 1, for which the two theories are equivalent in the sense of their equal effective potential and number of vacuum states.

In section 4 we are going further and discuss the caases $N_f = N_c$ and $N_f = N_c$ + 1, for which the SP theory will be equivalent to SU theory at a singular point, where the "baryons" are zero.

In section 5 we discuss the problems which appear in section 4 and something about the dualities for $N_f \geq N_c + 1$.

2. SUPERSYMMETRIC SU(N_c) AND SP(N_c) GAUGE THEORIES

2. 1. SU(N_c)

These are the "oldest" theories treated in the literature, starting with seminal papers [1], where present ideas were introduced in order to discuss for the first time dynamical SUSY breaking. Actually the construction of exact effective potentials and the supersymmetry breaking appear both in the initial discussion.

In [2], the four dimensional supersymmetric gauge theories which have a continous manifold of inequivalent vacua was treated in detail, for a particular range of the number of flavors when the number of colors is fixed the starting point was the supersymmetric QCD, based on an SU(N_c) gauge theory with N_f flavors of quarks, Q^i in the fundamental representation and Q_i in the antifundamental representation. The anomaly free global symmetry is

$$SU_{Nf} \times Su_{Nf} \times U(1)_R \qquad (1)$$

where the $U(1)_R$ charge of Q is $\frac{N_f - N_0}{N_f}$.

For these theories has been shown in [2][3][11] that the effective Lagrangian dynamically generated for these theories is

$$W_{eff} = \left(N_c - N_f\right) \in N_c - N_f \left(\frac{\Lambda^{3N_c - N_f}}{det\, Q\, Q} \right)^{1/N_0 - N_f} \tag{2}$$

where Λ is the dynamically generated scale of the theory, the determinant is over all the matter fields in the low-energy theory(which lie below the dynamically generated scale) and the ε factor appears as a sign of the fact that we have multiple vacua.

One of the main features of this case it is that the classical and quantum levels differ dramatically. In the classical theory, the scalar potentialis zero for an entire space given by the flat direction correspondingto squarks. This space is the classical moduli space of vacua.

For the quantum case, formula 2 tells us that the only value for whichthe potential is 0 is at infinity, which cannot be a minimum. So at quantum level the degeneracy is completely removed and the theory does not have any vacuum.

To characterize the moduli space gauge invariantly, in [2] were introduced the following gauge invariant combinations

$$M^{\ i}_{r\ l} = Q^i\, Q_{r\ l} \tag{3}$$

$$B_{i_{N_0+1},\ldots,i_{N_f}} = \frac{1}{N_c!} \in_{i_1 \ldots, i_{N_f}} Q^{i_1} Q^{i_2} \ldots Q^{i_{N_c}} \tag{4}$$

and the same for $\tilde{B}$. The lore is to call M mesons and B baryons.

Their charges are completely determined by the charges of Q's.

The flat directions are the spaces of these new fields, subject to a constrained which simply connects the 3 fields and follows from the Bose statistics for the fundamental quarks.

At classical level, in the case N_f=N_c, there is only one constraint

$$\text{det M-B}\tilde{B} = 0 \tag{5}$$

At quantum level this changes because of a one instanton effect.

The modified form for the constrain is

$$\text{det M-B}\tilde{B} = \lambda^{2Nc} \tag{6}$$

The quantum space is different from the classical one. Of course, the effective potential given by (2) is now 0.

One important observation consist in the existence of specific points where the global symmetry is enhanced. This points are called singular points. One of the important singular points is the one with

$$B=\tilde{B}=0, \tag{7}$$

and the M matrix is

$$M_{ij}=\Lambda^2\sigma_{ij} \tag{8}$$

It is obvious that in this case the condition (6) is satisfied. In this case the flavor symmetry $SU(N_f)$ is broken to $SU(N_f)$. This is an important result which will be used later. The "t Hooft anomaly conditions are satisfied for the broken symmetry. (conform [2]).

For the case $N_f=N_c+1$, the quantum moduli space of the massless theory is the same as for the classical theory. The difference between this case and the preceding one consist in realization of the confinement, for $N_f=N_c$ the confinement is realized with chiral symmetry breaking and for $N_f=N_c+1$ the confinement is realized without chiral symmetry breaking. [2][11]

For the case $N_f \geq N_c+2$, the quantum moduli space is the same as the classical one. The method of constructing the effective potential is different and for these case appears the duality.

2. 2. *$SP(2N_c)$*

In this case the gauge group is the symplectic group, *$SP(2N_c)$* this being the subgroup of *$SU(2N_c)$* which leaves invariant an antisymmetric tensor J^{cd}, which can be taken to be $J = 1\otimes i\sigma_2$.

The dimension of this group is $N_c(2N_c + 1)$. The matter content consist in $2N_f$ fields Q_i, $i = 1. . . 2N_f$, in the fundamental representation of *$SP(2N_c)$* which is $2N_c$ dimensional.

The noduli space of degenerate SUSY vacua, given by the zero's of the scalar potential is given by

$$Q_{ij}=\begin{cases} a_i & if\ i=j\le N_f\ or\ i=j+N_c \\ 0, & otherwise \end{cases}.$$

for $N_f \leq N_c-1$ and

$$Q_{ij}=\begin{cases} a_i, & if\ i=j\le N_c\ or\ i=j+N_{ci} \\ 0, & otherwise \end{cases}$$

The space of vacua is now specified only by "meson" superfields, which are given by $M_{ij}=Q_{ic}Q_{jd}J^{cd}$.

In the case N_f $(N_c-1$, explicit calculations of [7] showed that the effective potential dynamically generated in this case is given by

$$W_{eff}=(N_c+1-N_f)\in_{N_c-N_f}\left(\frac{2^{N_c-1}\ \Lambda_{N_c,N_f}^{3(N_c+1)-N_f}}{PfM}\right)^{1/(N_c+1-N_f)} \tag{9}$$

The results (2) and (9) will one of our starting points in the next section.

For $N_f \geq N_c$ we have the same behavior as in the $SU(N_c)$ case for different values of both N's. We will return to this common feature latter.

3. $N_F \leq N_C-1$. THE EQUIVALENCE BETWEEN $SU(N_C)$ AND $SP(N_C-1)$

First we define what we imply by equivalence.

We say that two theories are equivalent if they have the same effective potential and the same number of vacuum states. In some cases the equivalence requirement can be stronger in the sense that two equivalent theories can have additional common features, but these are the necessary conditions for the duality. We return to this discussion in the conclusions.

3. 1. *Pure Yang-Mills theories (no matter)*

Consider two pure Yang-Mills supersymmetric gauge theories, one with gauge group $SU(N_c)$ and the other one with gauge group $SP(2N_c-2)$. The only kind of confinement which appear at this level is the gaugino condensation, gaugino being the fermionic partner of the gluons in the vector superfield.

In [5], the result for this condensation for our groups was

$$\frac{<\lambda\lambda>_{SU(N_C)}}{32\pi^2} = \in N_c \Lambda^3_{SU}, \text{ and } \frac{<\lambda\lambda>_{SP(2N_c-2)}}{64\pi^2} = 2^{-2/N_c} \in_{N_c} \Lambda^3_{SP}. \quad (10)$$

where the indices for (denote the group to which the scale correspond. Again the $\in_{Nc}$ factor represents the root of unity and the indice denotes the number of vacuum states.

Now we make one important assumption for our gauge groups. Assume that the two scales are related by the following

$$2^{1-\frac{2}{N_c}} \Lambda^3_{SP} = \Lambda^3_{SU} = \Lambda^3_{N_c,0} \quad (11)$$

In this case we can write the two relations in (10) in a single form

$$\frac{<\lambda\lambda>}{32\pi^2}_{SP,SU} = \Lambda^3_{N_C,0} \in_{N_c} \quad (12)$$

which tells us that the gaugino condensate is the same for both theories therefore the vacuum structure is the same, both theories having N_c vacuum states.

The effective potential of the pure Yang Mills theory is constructed with the help of the "glue-ball" field S. Because S has as source $\log \Lambda^{3N_c-N_f}$ for both theories, and now the two scales are taken to be equal, the "glue-balls" of both theories are identical giving the effective potential:

$$W(S) = S\left[\log\left(\frac{\Lambda_{N_c,0}^{3N_c}}{S^{N_c}}\right) + N_c\right] \tag{13}$$

The two requirements for equivalence are now satisfied and we state that at pure gauge level $SU(N_c)$ and $SP(N_c\text{-}2)$ are equivalent.

The choice of 11 allows us to state this equivalence. A similar choice will be made after introducing flavors.

3. 2. *Supersymmetric QCD*

Let us now introduce matter fields in the fundamental representations of both gauge groups as we discussed in section 2. For SU we can introduce any number of flavors but for SP we can introduce only an even number of flavors as it is required [15]. Suppose that at each level of introducing matter, the number of flavors introduced in SP theory is always the double of number of flavors for SU, i. e. in SU we are introducing flavors one by one and in SP we are introducing flavors in pairs. So, at each level we will have N_f matter fields in the SU theory and $2N_f$ matter fields in the SP theory, denoted by $Q^{i(SU)}$, $i=1...Nf$ and $Q^{i(SP)}$, $i=1...2N_f$.

The gauge invariant combination of matter fields were introduced in section 2. As a function of these we have the effective potentials generated non-perturbatively as in (2), (9).

As it is obvious from these two formulas, the indices for (appearing in both theories is the same, so the number of vacuum states is the same.

We make now another assumption. We suppose that the VEV for the squarks are the same in both theories. With this, we were able to show that for any N_f N_c,

$$PfM_{SP(2Nc-2)} = detM_{SU(Nc)}.$$

where the indices of M's denote the corresponding gauge groups. Of course, for SU we have N_f flavors and for $SP2N_f$ flavors.

The relation between scales is considered to be a generalization of 11 as follows

$$2^{N_c-2}\Lambda_{SP(2N_c-2),2N_f}^{3N_c-N_f} = \Lambda_{SU_{N_C},N_f}^{3N_c-N_f} \tag{15}$$

Using now (14) and (15), we can state that the potentials for the two theories are equal.

Coupling this with the above equivalence between vacuum structures, we can say that the 2 theories are equivalent.

4. $N_f = N_c$, $N_c + 1$

For this case, our previous discussion fails. This is because of the "baryons" appearing in the SU theory and not appearing in the SP theory. In SP theories, because the "baryons" are defined with (factors, they can be decomposed in products of mesons.

We cannot say that such products are baryons because the mesons have zero baryon numbers(so their product has also 0 baryon number) whereas the baryons have non-zero baryon numbers. So, indeed, the only gauge invariant fields for SP are the mesons.

This means that the theories cannot be equivalent. The SP theories are equivalent with SU restricted to a singular point, i. e. to a subspace of the moduli space. This point of the moduli space is exactly the one discussed in section 2 i. e. the point where the 2 baryon fields are 0 but the meson field still satisfies the quantum moduli space condition det $M=\Lambda^{2Nc}$ The effective potential is 0 for both theories from definition.

For both theories, by adding mass terms to the dynamically generated superpotential, one obtains the fermion condensation, given by the expectation values for the meson field M. N_f (N_c, where all the classical vacua are lifted, by adding $W_{tree} = \frac{1}{2} m^{ij} M_{ij}$ for SP group and W_{tree} = mM for SU, the result for the expectation value for M is

$$\left\langle M_{ij} \right\rangle = \epsilon_{N_c} \left(2^{N_c - 2} \, Pfm \, \Lambda_{SP}^{3N_c - N_f} \right)^{1/N_c} \left(\frac{1}{m} \right) ij \tag{16}$$

for $SP(2N_c\text{-}2)$ group and

$$\left\langle \begin{matrix} i \\ M \; r \\ j \end{matrix} \right\rangle = \epsilon_{N_c} \left(\det m \, \Lambda_{SU}^{3N_c - N_f} \right)^{1/N_c} \left(\frac{1}{m} \right)_r^i \tag{17}$$

for SU(Nc) group.

So the number of vacua is the same for both groups and this is true for the entire moduli space of both theories. The expectation values for M are also equal because of the relation between scales [15] and the identity expressed in [14] which is now changed with the same relation for m's, the sources of M'

The refore, our equivalence requirements are satisfied and we say that $SP(2N_c\text{-}2)$ is equivalent with $SU(N_c)$ for $N_f = N_c$.

We go further, to $N_f = N_c.+1$. In this case, as obtained in [7], the effective potential for the light fields in the low energy theory is

$$W = - \frac{Pfm}{2^{N_c - 1} \Lambda_{SP}^{2N_c - 1}} \tag{18}$$

for $SP(2N_c\text{-}2)$.

If compared with the result for $SU(N_c)$ obtained in [2], again the equality between the superpotentials is obtained for the singular point $B = \tilde{B}$ of the moduli space for SU. Both theories have at origin of field space massless composite mesons so

the chiral symmetry of the theory is unbroken there. This represents confinement without chiral symmetry breaking for both theories, as opposed with the one with chiral symmetry breaking obtained for $N_f = N_c$. So, again the two theories are equivalent in the sense that they satisfy the 2 necessary requirements.

5. POSSIBLE DUALITIES AND FURTHER COMMENTS

It is already well known that for the case $N_f > N_c + 2$, SQCD can be described in the original "electric" formalism and in the dual "magnetic" formalism. (see [10][11] for an extended discussion of SU and [7] for the duality in SP). The $SU(N_c)$ electric theory has a dual description as a $SU(N_f--N_c)$ theory and the $SP(2N_c - 2)$ electric theory has a dual description as a SP(2Nf - 2Nc - 2) theory.

As in previous section, the $SP(2N_c - 2)$ theory is equivalent with $SU(N_c)$ and the $SP(2N_f-2N_c-2)$ is equivalent with $SU(N_f -N_c)$. So if we have an equivalence between electric theories, the same equivalencewill be between their duals. An equivalence plus a duality does not give aduality, because does not satisfy all the requirements(ex. 'tHooft anomaly condition). Nevertheless, some of the duality features appear after composinga duality and a equivalence.

If we start with $SU(N_c)$ at a singular point, by using the relation between the electric and magnetic baryons

$$B^{i_1\cdots i_{N_c}} = C \in^{i_1\cdots i_{N_c} j_1\cdots j_{N_c}} b_{j_1\cdots j_{N_c}} \tag{19}$$

(B are the electric baryons, b are the magnetic baryons and $\tilde{N}_c = N_f - N_c$), we see that the dual theory will be again at a singular point where all the dual baryons are 0.

If the original mesons have all the entries non-null, the corresponding M's singlets which appear in the dual theory are non zero and therefore all the dual quarks are massive. The low energy magnetic group leads to gluino condensation after integrating out all the massive fields and the superpotential has the same form as in the case $N_f < N_c$, but of course now the sign will be opposite.

For Sp theories, to $M_{ij} = Q_{ic}Q_{jd}J^{cd}$ mesons correspond $M_{ij} = -M_{ji}$ singlets. Again, for Pf $M \neq 0$ in the electric theory, the M singlets are non zero and again the dual quarks are massive. By integrating out the massive quarks and using the relation between scales and relation [14] the resulting superpotential will be the same as for SU.

So a duality plus an equivalence give an equivalence. We can say that $SU(N_c)$ and $SP(N_f - N_c - 2)$ are equidual (obtained one from another by a duality and an equivalence).

REFERENCES

1. I. Affleck, M. Dine N. Seiberg, *Nuclear Physics* B241 (1984) 493; *Nuclear Physics* 256 557 (1985).
2. N. Seiberg, *Phys. Rev*. D49 6857, hep-th 9402044 (1994).
3. K. Intriligator, R. G. Leigh, N. Seiberg, *Phys. Rev*. D50 1092 hep-th 9403198 (1994).
4. S. Cordes, *Nucl. Physics* B273 629 (1986).
5. D. Finnell P. Pouliot hep-th 9503115.
6. K. Intriligator N. Seiberg, *Nucl. Phys*, B444 125 hep-th 9503179 (1995).
7. K. Intriligator P. Pouliot, hep-th/9505006, *Phys. Lett*. 353B 471 (1995).
8. I. Pesando, hep-th/9506139.
9. S. B. Giddings J. M. Pierre, hep-th/9505196.
10. N. Seiberg, hep-th/9411149, *Nucl. Phys*. B435 129 (1995).
11. K. Intriligator N. Seiber, hep-th/9509066.
12. N. Seiberg E. Witten, hep-th/9408074, *Nucl. Phys*. B431 484 (1994).
13. C. Montonen D. Olive, *Phys. Lett*. 72B 117 (1977).
14. C. Vafa E. Witten, hep-th/9408074, *Nucl. Phys*. B432(1994) 3.
15. E. Witten, *Phys. Lett*. B117 324 (1982).
16. D. Kutasov, hep-th/9503086, *Phys. Lett*. 351B 95 (1995).
17. D. Kutasov, A. Schwimmer, hep-th/9505004, *Phys. Lett*. 353B 57 (1995).

STUDIA UNIVERSITATIS BABEŞ-BOLYAI, PHYSICA, XLI, 2, 1996

A NONLINEAR MODEL OF ECOSYSTEM

S. CODREANU[1], **M. F. DANCA**[2]

ABSTRACT. The work presents the dynamics of an ecosystem with three species in competition. The methods of nonlinear dynamical systems theory are used and different possible behaviour of the ecosystem are revealed.

Introduction

It is well known that the increasing progress in the understanding of the dynamical processes in ecology is due to the study of more realistic mathematical models in this field [1]. Such models are in fact nonlinear differential equations (ordinary, delay, partial, stochastic) or difference equations (when the variable time *t* can be considered discrete). The basic characteristic of these equations is the impossibility to be solved analytically. But, nevertheless, a considerable amount of informations can be obtained by using the methods of the new theory of nonlinear dynamical systems [2-5].

In this work we present an application of this theory to the study of the nonlinear dynamics of the competition between three species. The main result is that there are different possible behaviours of the considered dynamical system.

Study of the nonlinear model

Let us consider the following system of three differential equations:

$$\frac{dx_i(t)}{dt} = x_i(t)\left[1-\sum_{j=1}^{3} A_{ij}x_j(t)\right], \qquad i=1,2,3$$

with

$$\left(A_{ij}\right)=\begin{pmatrix} 1 & a & b \\ b & 1 & a \\ a & b & 1 \end{pmatrix}; \qquad \sum_{i=1}^{3} x_i(t)=1; \qquad 0 \le x_i(t) \le 1 \tag{1}$$

and the parameters (a, b)>0.

[1] "Babeş-Bolyai" University, Faculty of Physics, 3400 Cluj-Napoca, România.
[2] Spiru Haret High School, 3400 Cluj-Napoca, România.

The variable x_i denotes the population density of the species *i* and the (*i, j*) - th element of the matrix (A_{ij}) determines the effect of species *j* on the growth rate of species *I*.

The system (1) which contracts the volumes in the phase space has two steady states, or equilibria:

$$x_i^* = 0 \qquad (i = 1, 2, 3) \tag{2}$$

and

$$x_i^* = \frac{1}{1 + a + b} \qquad (i = 1, 2, 3) \tag{3}$$

We will consider only the last, nontrivial equilibrium, which depends on the parameters *a* and *b*. Its stability is analysed by the known method applied to the linearized system. Thus the stability matrix is:

$$(S_{ij}) = -\frac{1}{1 + a + b}(A_{ij}) \tag{4}$$

which leads to the eigenvalues equation:

$$(1 - \lambda)^3 - 3ab(1 - \lambda) + a^3 + b^3 = 0 \tag{5}$$

The solutions of this equation are:

$$\lambda_1 = 1 + a + b$$
$$\lambda_{2,3} = 1 - \frac{a + b}{2} \pm \frac{i}{2}\sqrt{3}\,|a - b| \tag{6}$$

Since *a* and *b* are positive, the eigenvalues (6) have positive real parts if $a+b < 2$ and the equilibrium is unstable. If $a+b \geq 2$, there is instability only in one direction and the stability in a phase plane. Obviously if $a+b = 2$, then $\mathrm{Re}\lambda_{2,3} = 0$ and the phase trajectory is a limit cycle which indicates an oscillatory behaviour.

We have investigated this dynamical system also numerically using the standard Runge-Kutta algorithm, and we observed different behaviours as the parameters were varied. Some of these behaviours are presented in the Figures 1-4. In figure 1 a steady state of the system is illustrated. The limit cycle can be observed in the Figure 2. For the parameters *a* and *b* indicated in the Figure 3 the orbit asymptotically approaches the corners of the triangular region defined by $\sum_{i=1}^{3} x_i = 1$ in a cyclic fashion and finally rests in one of them. The same behaviour is illustrated in the Figure 4 where the arrows indicate the evolution directions of the phase trajectory of the system.

Conclusions

We have investigated a special kind of ecosystem by using the general methods of the theory of nonlinear dynamical systems. Both analytical and numerical study have revealed different behaviours of the system as the parameters were varied. The model considered by us could be applied also in biomedical sciences.

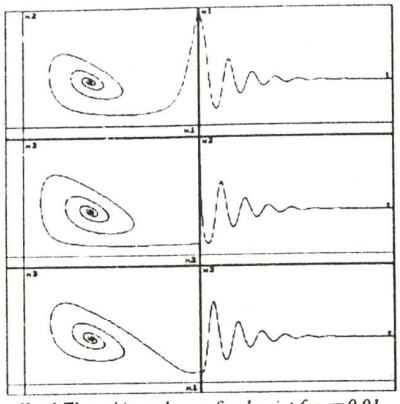

Fig.1 The orbit tends to a fixed point for a=0.01, b=1.6

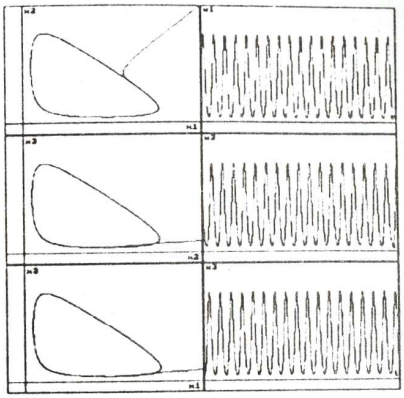

Fig.2 A limit cycle for a=0.9 and b=1.1

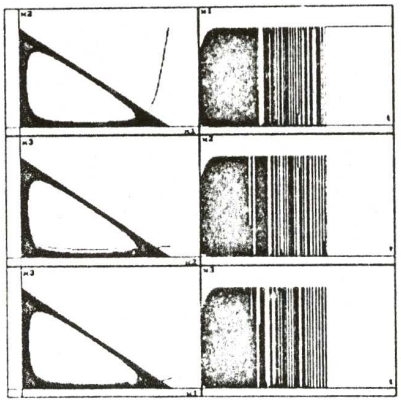

Fig 3 The orbit asymptotically approaches one corner of the triangular region (a=0.01 and b=2)

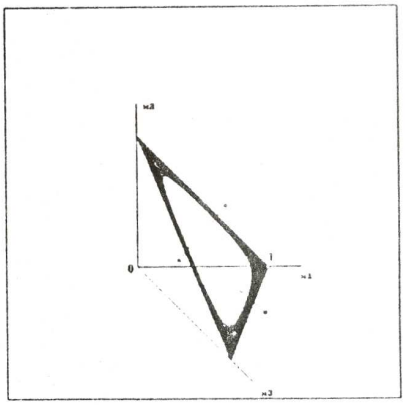

Fig 4 A thee dimensional illustration of the behavior from the fig 3

REFERENCES

1. J. D. Murray, *Mathematical Biology*, Springer-Verlag Berlin, 1990.
2. E. Ott, *Chaos in Dynamical Systems*, Cambridge Univ. Press, 1992.
3. S. Codreanu, M. Danca, *Journal of Biological Physics* (Netherlands), 23, 1-9, 1997.
4. M. Danca, S. Codreanu, B. Botond, *Journal of Biological Physics* (Netherlands), 23, 11-20, 1997.
5. S. Codreanu, M. Danca, Polish Journ. of Environ.Studies vol.6, no.1, 21-24, 1997.

STUDIA UNIVERSITATIS BABEŞ-BOLYAI, PHYSICA, XLI, 2, 1996

A DETAILED COMPUTATIONAL STUDY OF RABINOVICH - FABRIKANT (R. R.) MODEL

M. F. DANCA[1], **S. CODREANU**[2]

ABSTRACT. The nonlinear R. F. model, which cannot be analytically integrated is numerically investigated with the standard Runge-Kutta method. Different behaviours of the system are obtained as the parameters are varied.

The model investigated by us, which was proposed by Rabinovich-Fabrikant [1] in order to explain the stochasticity arising as the result of development of modulation instability in a nonequilibrium dissipative medium, is:

$$\dot{x}_1 = x_2(x_3 - 1 + x_1^2) + bx_1$$

$$\dot{x}_2 = x_1(3x_3 + 1 - x_1^2) + bx_2$$

$$\dot{x}_3 = -2x_3(a + x_1x_2)$$

with *a* and *b* positive parameters.

This system of three autonomous differential equations contracts the volumes in the phase space if a > b so it could have an attractor. Also the system is symmetrical by the changes $x \to -x$ and $y \to -y$. For the physical reasons we will restrict our study only to the case $x_3 > 0$.

Thus the equilibrium states of the system are $X^*_0 = (0, 0, 0)^T$ and:

$$X^*_{1,2} = \left(-\frac{\pm a}{\sqrt{a / b(2 + r)}}, \pm \sqrt{a / b(2 + r)}, \ \frac{2 + r - ab + b^2}{2 + r} \right)^T,$$

$$X^*_{3,4} = \left(-\frac{\pm a}{\sqrt{a / b(2 - r)}}, \pm \sqrt{a / b(2 - r)}, \ \frac{2 - r - ab + b^2}{2 - r} \right)^T$$

where $r = \sqrt{1 - 2ab + 3b^2}$

[1] Babeş-Bolyai Univ., Faculty of Physics, 3400 Cluj-Napoca, România.
[2] Spiru Haret High-School, 3400 Cluj-Napoca, România.

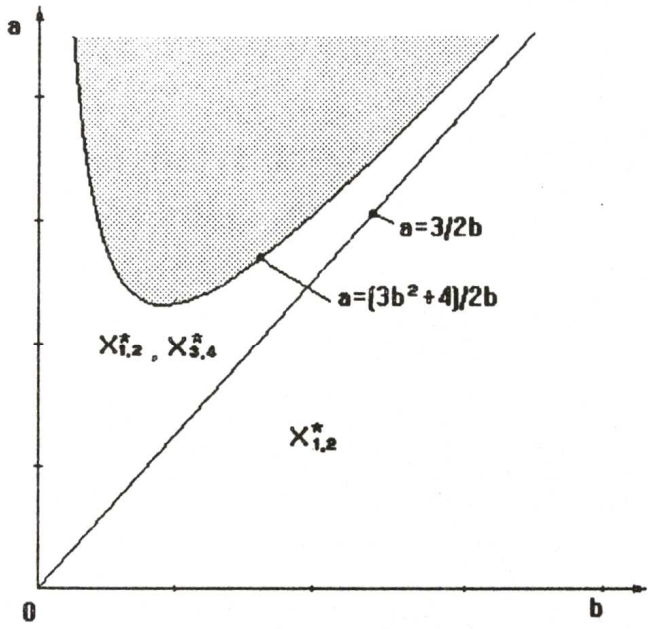

Fig. 1 Diagram of the parametric domains of the steady states

It is obviously that the nontrivial steady state of the system depends strongly on the choice of the parameters *a* and *b*.

In figure 1 we present a diagram of the domains of values of parameters for which the steady states are possible. There are not equilibrium states in the shaded region.

The stability of the equilibria with the usual technique applied to the linearized equations is very difficult. It implies to solve the following eigenvalues equation:

$$\det(A-\lambda I) = 0$$

where A is the Jacobi matrix evaluated at the points X*

$$A = \begin{pmatrix} b + 2x_1x_2 & x_3 - 1 + x_1^2 & x_2 \\ 3x_3 + 1 - 3x_1^2 & b & 3x_1 \\ -2x_2x_3 & -2x_1x_3 & -2a - 2x_1x_2 \end{pmatrix}_{X^*}$$

So we decided to find the steady states and the other possible behaviours of the system by numerical integration. For that we have used a standard Runge-Kutta method [2]. Our main results are presented in the Figures 2-7.

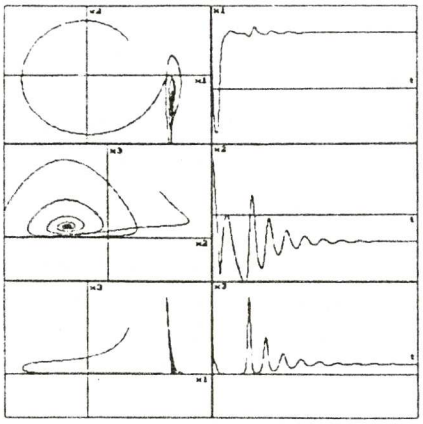

Fig. 2. A steady state.
a = 0.4
b = 0.09

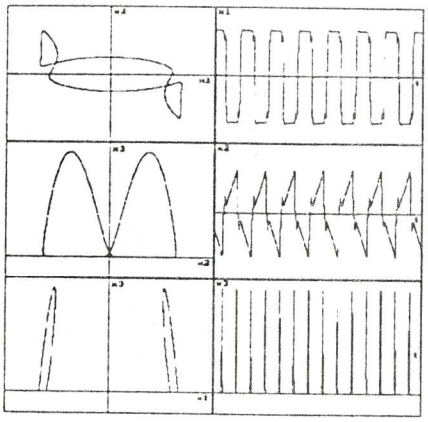

Fig. 3. A limit cycle
a = 1.1
b = 0.1

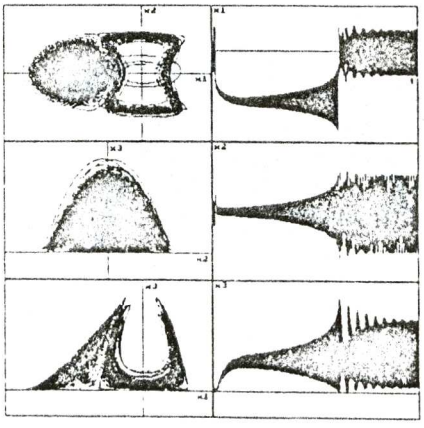

Fig. 4. A possible limit cycle
a = 1
b – 0.4

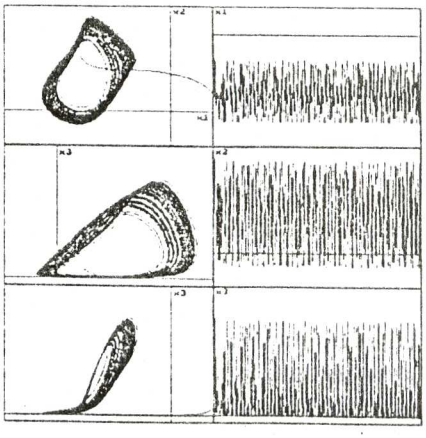

Fig. 5. A chaotic behavior
a = 1.2
b = 0.1

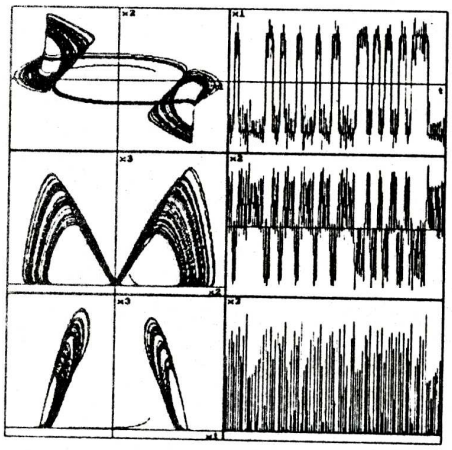

Fig.6
A chaotic behavior
a=1.2
b=0.1

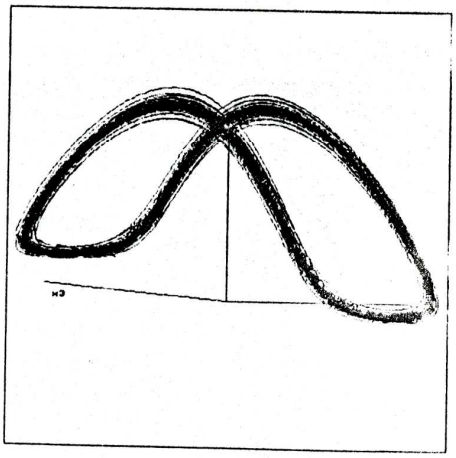

Fig.7
A three dimensional version of the Fig.3.
The transients have been neglected.
a=0.06
b=0.05

REFERENCES

1. M. I. Rabinovich, A. L. Fabrikant, *J.E.T.P.*(Sov)77, 617, 1979.
2. M . - F . D a n c a , *D o c t o r T h e s i s* , Technical University of Cluj.